Mesure des électrons et recherche de bosons de Higgs en canaux multi-leptons avec l'expérience CMS au LHC

Clémentine Broutin

ÉCOLE POLYTECHNIQUE

THÈSE

présentée

pour obtenir le grade de

DOCTEUR EN SCIENCES

par

Clémentine Broutin

Electron Measurements and Search for Higgs Bosons in Multi-Lepton Channels with the CMS Experiment at LHC

Soutenue le 12/07/2011 devant le jury composé de :

Mme.	M.-C.	Cousinou	Présidente
M.	G.	Moultaka	Examinateur
M.	J.-C.	Brient	Examinateur
M.	G.	Hamel de Monchenault	Rapporteur
Mme.	I.	Wingerter-Seez	Rapporteur
M.	C.	Charlot	Directeur de thèse
M.	Y.	Sirois	Directeur de thèse

Contents

Aknowledgements

The only people with whom you should try to get even are those who have helped you.

John E. Southard

'Thèse' : un petit mot qui cache tant de travail, tant de volonté... et tant de soutien ! 'Merci' : un petit mot tout simple lui aussi, pour m'adresser à toutes les personnes qui m'ont aidée durant ces trois ans, et sans qui ce manuscrit ne serait pas ce qu'il est aujourd'hui.

Je m'adresse d'abord à mes directeurs. Merci Claude pour tes conseils, ta patience et ton attention, merci d'avoir trouvé du temps pour moi, même quand tu n'en avais pas, et de m'avoir aidée à avoir confiance en cette thèse. Merci Yves pour tes idées et tes conseils. Merci à vous deux de m'avoir encadrée pendant ces trois ans, et tout particulièrement ces derniers mois, malgré les autres préoccupations du groupe.

Merci aussi à mes rapporteurs, qui m'ont aidée à prendre du recul sur mon manuscrit et à l'améliorer. Et merci à l'ensemble de mon jury pour sa disponibilité et sa bonne volonté.

Un grand merci à toute la communauté CMS qui m'a fait une petite place ; merci en particulier au groupe ECAL PFG et à son ambiance positive. Merci à tous ceux qui ont répondu à mes nombreuses questions, notamment pendant ces derniers mois : outre l'équipe du LLR, je pense notamment à Olivier, Anne-Fleur, Riccardo, Andrea et tous les autres...

Je tiens aussi à remercier toute l'équipe CMS du LLR, qui a mis de la vie dans ces trois années de travail. Pascal a tout particulièrement compris mon caractère et m'a beaucoup aidée, non seulement à travailler, mais aussi à dédramatiser, ce qui n'était pas toujours une mince affaire ! Stéphanie aussi a été très proche de moi : merci pour ton écoute, pour le massage des pieds, pour les conseils et les confidences ! Je n'oublie pas non plus les blagues de Christophe, e la bestemmia del Roberto, qui ont rythmé les journées de notre bureau. Et les sourires de Lamia, la gentillesse d'Arabella, la sympathie de Roko, le calme rassurant de

Lorenzo, les discussions avec David et Nadir, que mon stress semble amuser... et bien sûr l'ambiance Alexienne, qui n'a pas son égal ;-) Merci aussi à Philippe, discret mais présent et un vrai soutien lui aussi.

J'ai aussi une pensée pour les stagiaires, en particulier Baptiste, Loïc, Alice et Thibaut : bonne chance pour la suite !

Je pense aussi au reste du labo : Magali, JP et Christophe, leur bonne humeur et leurs conseils, et puis les quarante-deux croissants de Daniel et Mathieu ! Merci à Thu et Nora pour leur bonne humeur, à Maïthé pour sa gentillesse, à Elodie pour ses coups de main surtout dans les derniers moments, et à Brigitte qui a patiemment encadré toutes mes pérégrinations. Merci bien sûr à Hamid qui sait tellement tout gérer, à la super équipe des informaticiens, et à tout le labo, les Toulousains et les autres, les buveurs et les autres :-)

Je voudrais aussi remercier Claudia, Jeff, Mounir, David et Jeanne : vous avez fait de mes déjeuners de vrais moments d'amitié. Et pas seulement mes déjeuners ! Ca va être difficile de se voir aussi souvent l'an prochain, mais quelque chose me dit qu'on trouvera bien des occasions :-D

Et puis, merci à mes amis, en thèse ou non, que j'ai moins vus les derniers mois de la thèse, mais dont je sens le soutien à chaque instant. Merci à tous ceux qui sont venus à ma soutenance tout en sachant que ça serait du Chinois ! Un merci tout particulier à Julie, super coloc' et même plus !

Merci à toute ma famille, qui de près ou de loin a suivi toutes les étapes de cette thèse. J'ai une pensée toute particulière pour Mamymone et son attention de tous les instants. C'était une année importante pour les trois filles, et j'espère qu'on pourra fêter ça toutes les trois cet été, si possible pas seulement en parlant de dents ;-)

Merci aussi à ma (future) belle-famille, qui a accepté mon emploi du temps très occupé et m'a aussi gentiment soutenue.

Enfin, merci à toi Guillaume, à qui j'ai rendu la vie terrible ces derniers mois, et qui m'as aidée à tenir le coup. Merci de m'avoir coachée, de m'avoir supportée et de m'avoir soutenue... Je ne peux vraiment pas imaginer ce que ces trois ans auraient été sans toi ! C'est toi qui m'as le plus aidée, et c'est sûrement à toi que j'ai fait le plus de reproches... Merci pour plein de petits trucs, mais surtout merci pour toi, et merci d'être là !

Qu'est-il devenu ? Où est-il ? Où se cache-t-il ? Que ferai-je pour le trouver?
Où courir? Où ne pas courir? N'est-il point là ? N'est-il point ici ?
Molière, *L'Avare*

Introduction

A child of five would understand this. Send someone to fetch a child of five.

Groucho Marx

The dream of a particle physicist is to explain the matter of our whole universe by a handful of elementary particles, and its structure by few simple interactions. This goal was almost achieved by the Standard Model, developed in the 1960's and early 1970's. This theory unifies the concepts of Quantum Mechanics and Special Relativity, and describes elementary particles of matter (i.e. fermions) and their electromagnetic, weak and strong interactions (through gauge bosons).

This theory of fundamental particles and their interactions has been remarkably confirmed in collider experiments in the past decades, in particular by the discovery of particles such as the Z boson and the top quark, that had been predicted. To complete the sketch of the Standard Model, the Higgs mechanism introduces gauge boson masses via the field of the Higgs boson. Besides, fermions get massive through their interactions with the Higgs field. The discovery of this Higgs boson would be the crowning achievement of the Standard Model.

The cards are now in the hands of experimental physicists. The existence of an elementary particle such as the Higgs boson is tested at colliders. High energy collisions are expected to create the searched particle, and detectors located around collision points allow the hunt for a typical signature. After the exclusions from the Large Electron Positron Collider and the Tevatron (proton-anti-proton collider) experiments, the Large Hadron Collider is the major actor for the Higgs hunting in the next years.

Despite its phenomenal success, it is clear that the completion of the standard model

is not marking the end of the road for theoretical physics. Theorists have been working on extensions of the Standard Model that can explain such phenomena as neutrino oscillations, or describe the gravitational interaction. Signatures of such theories are naturally also searched at LHC experiments.

Such a project is not to be improvised. The development and construction of the LHC machine took over two decades. It was built to provide proton-proton collisions with a nominal center-of-mass energy of 14 TeV (7 TeV during the first years) and a very high luminosity ($\mathcal{L}_{nominal} = 10^{34}$ cm^{-2}s^{-1}). In parallel, detectors were conceived and built, responding to the LHC characteristics and the physics goals: in particular the CMS and ATLAS experiments were designed primarily for the search of Higgs bosons and physics beyond the Standard Model. The response of these detectors was simulated, allowing the development of physics object reconstruction algorithms and research analyses.

This precise preliminary work provided reliable tools for the study of the first LHC collision events in the end of 2009. This date marked the boundary between an era dominated by analysis optimization on simulation, and a new period of data understanding and simulation corrections. This transition is the context of my PhD, which started with optimization studies of algorithms and analyses, and was soon oriented towards the study of the first LHC data.

This thesis starts with an introduction of the Standard Model and the Higgs mechanism. Some extensions of the Standard Model are also presented, in the LHC phenomenological context. The Higgs boson(s) of several theories present clean multi-lepton signatures that are more particularly discussed in this thesis. The second chapter describes the LHC machine and the CMS detector. After these theoretical and experimental concepts, the work produced during my PhD is described in details in the next chapters.

The trigger is a fundamental tool for all physics analyses in CMS. It makes the first decision on each event: whether or not to record the corresponding information. Its rate must be controlled according to the recording and storage capacity. Besides for each analysis the trigger efficiency must be as high as possible, and precisely measured. The LLR was mainly involved in the building of the CMS Electromagnetic Calorimeter, and responsible for the Level-1 electron and photon trigger. This trigger, and the measurements that I made to control its efficiency, are described in chapter 3.

An important parameter in multi-lepton analyses is the lepton charge. It is used in

particular to identify the lepton pair from the decay of a chosen particle. Electron charge identification presents unprecedented difficulties in CMS. This is due to the high amount of material present in the tracker, that enhances bremsstrahlung and photon conversions, thus complicating electron topologies. I developed new and more precise electron charge identification algorithms, that are described in chapter 4.

Finally, a good control of the trigger efficiency and a good knowledge of lepton objects allow the development of research analyses. The analysis of research of the Standard Model Higgs boson in the decay channel $H \rightarrow ZZ^{(*)} \rightarrow 4\ell$ is described in chapter 5. The data recorded in 2010 did not provide enough statistics to derive any exclusion or discovery of the Standard Model Higgs boson, however other models could be tested. I developed an analysis for the search of doubly charged Higgs bosons from the Seesaw mechanism, that is detailed in that chapter too. This analysis sets new limits on the masses of doubly charged Higgs bosons.

Chapter 1

Theoretical context: the Standard Model and Higgs Boson(s)

'Excellent' I cried.

'Elementary.' said he.

Sir Arthur Conan Doyle, *The Adventure of the Crooked Man*

Contents

1.1 The Standard Model and Electroweak Symmetry Breaking

The philosophy of the understanding of matter through ages can be summarized in two words: elementary and symmetry. The search for elementary constituents of matter was already a concern in the antiquity, when Democritus introduced the word 'atom' ($\acute{\alpha}\tau o\mu o\varsigma$: uncuttable).

Elementary constituents can simplify significantly the description of matter, because the combination of a small number of elementary bricks can explain a high diversity of constructions. This is how the two kinds on nucleons (protons and neutrons) are the common basis of the 118 atoms represented in Mendeleïev's table. Similarly, the more recent study of the protons and neutrons showed a high diversity of particles with the same properties: the hadrons. This diversity was understood by the compositeness of these particles, based on the combinations of three kinds of quarks (called up, down and strange).

Besides, the structure of matter is often understood thanks to symmetry considerations. The use of symmetry allowed Mendeleïev to predict the existence of atoms that had not been observed yet, to complete his table. Moreover, symmetry considerations in the study of hadrons lead Gell-Mann and Zweig to introduce quarks as fundamental building blocks for hadrons, in 1964. The theory of quarks was largely developed in the following years. Many other examples could be given, but we will now move to the description of elementary particles.

1.1.1 Particles, Interactions and Symmetries

The goal of the Standard Model is to describe the elementary particles of matter, their properties and their interactions.

Once a collection of elementary particles is determined, one is tempted to assign them some parameters that constitute their identity (electric charge, mass...). This assumes that those quantities are conserved: for example, if the electric charge of a particle can change, it does not constitute its identity.

The meaning of these parameters appears when interactions are discussed: these parameters are indices of the sensitivity of the particles to the corresponding interactions. For example, the electric charge of a particle indicates its sensitivity to the electromagnetic interaction.

Noether's theorem tells us that to each conserved parameter corresponds a symmetry. As a consequence, each interaction is associated to a (local) symmetry. As will be discussed in this section, the introduction of a local symmetry requires the addition of one or several spin-1 gauge fields: they describe the vectors of the corresponding interaction. These vectors, called gauge bosons, were also observed experimentally.

The particles of matter are called fermions; they are described by spinors (ψ, spin: $\pm\frac{1}{2}$). Their collection is made of three generations of leptons: the electron (e) and its neutrino (ν_e), the muon (μ) and its neutrino (ν_μ), the tau lepton (τ) and its neutrino (ν_τ); and three generations of quarks: up (u) and down (d), charm (c) and strange (s), top (t) and bottom (b) .

The behavior of these particles is described in a Lagrangian, which details their propagation in the vacuum.

The Lagrangian for the free propagation of a spin-$\frac{1}{2}$ particle (ψ) of mass m writes:

$$\mathscr{L}_{free} = \bar{\psi}\left(i\gamma^\alpha \partial_\alpha - m\right)\psi \ , \tag{1.1}$$

where γ^α are the Dirac matrices.

This expression is invariant under global $U(1)$ gauge transformations ($\psi(x) \to e^{i\Lambda}\psi(x)$). However the interactions observed in nature indicate the presence of other, local symmetries, which imply modifications to this Lagrangian.

Four fundamental interactions were observed experimentally, involving these particles: the electromagnetic, weak, strong and gravitational interactions. The Standard Model describes the three first ones, assigning them conserved particle parameters associated to local symmetries. However it fails to add the gravitational interaction. This loophole will be discussed at the end of this chapter.

The choice of the symmetry[1] to associate to an interaction is based on the required number of degrees of freedom, since the number of generators of the symmetry group is the number of gauge bosons that it can include. The electromagnetic interaction is carried by one vector boson, the photon: hence only one degree of freedom is necessary in the associated symmetry. This justifies the choice of a $U(1)$ symmetry.

[1]The researched symmetries are unitary transformations ($U(1)$, $SU(n)$ if $n > 1$). While $U(1)$ possesses exactly one degree of freedom (one generator), we recall that $SU(n)$ contains $n^2 - 1$ degrees of freedom ($n^2 - 1$ generators).

On the other hand, the weak interaction is carried by three bosons: W^+, W^- and Z, which requires a symmetry with three degrees of freedom, like $SU(2)$. This interaction is however not orthogonal to the electromagnetic interaction, and is only well described in a coupled model: the electroweak interaction, in the symmetry $SU(2) \times U(1)$. The other complications involved in this symmetry, such as the problem of the boson masses, require an electroweak symmetry breaking which is described in the next section.

Finally, the strong interaction is carried by eight bosons: the gluons. It is described by the $SU(3)$ symmetry. The choice of this symmetry group is motivated by several calculations and measurements, that will not be detailed here.

These three interactions are described in the Standard Model, in a global $SU(3) \times SU(2) \times U(1)$ symmetry.

1.1.2 Electroweak Interactions

1.1.2.1 Quantum Electrodynamics (QED)

The electromagnetic interaction applies on electrically charged particles, and is naturally associated to the conservation of the electric charge. As a consequence, its $U(1)$ symmetry (one gauge boson: the photon), is referred to as $U(1)_Q$.

This symmetry, that acts on a fermion field as: $\psi(x) \rightarrow e^{i\Lambda(x)}\psi(x)$, must leave the Lagrangian invariant. This requires the introduction of a field $A_\alpha(x)$, that couples to the particle by a coupling e and transforms under the gauge transformation as $A_\alpha \rightarrow A_\alpha + \frac{1}{e}\partial_\alpha \Lambda$. The derivative term ∂_α changes to a covariant derivative $D_\alpha = \partial_\alpha - ieA_\alpha$, and the term $\bar{\psi}(i\gamma^\alpha D_\alpha - m)\psi$ is invariant under the transformation.

The Lagrangian gains also a term corresponding to the free propagation of the gauge field A_α: $-\frac{1}{4}F_{\alpha\beta}F^{\alpha\beta}$, where $F^{\alpha\beta}$ is the gauge field strength tensor:

$$F_{\alpha\beta} = \frac{i}{e}[D_\alpha, D_\beta] = \partial_\alpha A_\beta - \partial_\beta A_\alpha \ , \tag{1.2}$$

This strength tensor is invariant under local gauge transformations, and the global Lagrangian is also invariant:

$$\mathscr{L}_{QED} = \bar{\psi}\left(i\gamma^\alpha D_\alpha - m\right)\psi - \frac{1}{4}F_{\alpha\beta}F^{\alpha\beta} \ . \tag{1.3}$$

The field A_α is the representation of the gauge boson: the photon. The covariant derivative introduces a coupling between the particle described by ψ, and the photon (with a factor e

proportional to the particle electric charge). The kinematic term $-\frac{1}{4}F_{\alpha\beta}F^{\alpha\beta}$ represents the propagation of the photon.

1.1.2.2 The Complications of the Weak Interaction

Choice of the symmetry

The first observed weak interactions were β decays: they indicated the presence of a massive charged gauge boson, coupling electrons to neutrinos for example. These interactions were observed to apply only on particles of left helicity; they are associated to the conservation of the helicity.

This charged gauge boson must be represented in a unitary group containing off-diagonal generators: the smallest known is $SU(2)$. A local gauge transformation in the non-abelian group $SU(2)$ is written as a function of its generators τ_a, the three Pauli matrices[2]. The matrices τ_1 and τ_2 correspond to these off-diagonal contributions of the charged weak bosons $W^{\pm}$. The third generator suggests the presence of a third neutral gauge boson.

Each fermion field can be written as the sum of its left-handed and its right-handed components: $\psi = \psi_L + \psi_R$. Right-handed components are not sensitive to the weak interaction, and are represented as singlets, while left-handed particles are represented as doublets. Each generation of fermions contains two doublets and two singlets[3], e.g. for the first generation:

$$L \equiv \begin{pmatrix} \nu \\ e \end{pmatrix}_L \ , \ e_R \ , \ Q \equiv \begin{pmatrix} u \\ d \end{pmatrix}_L \ , \ u_R \ , \ d_R \ . \tag{1.4}$$

As a consequence, this symmetry is referred to as $SU(2)_L$.

This $SU(2)_L$ symmetry is however not very satisfactory. First of all, the third generator τ_3 does not correspond to any physical boson. When the theory was developed the Z boson had not been discovered yet; it was observed that the corresponding boson could not be the photon, because, among other reasons, the τ_3 matrix imposes couplings to neutrinos. As a consequence, an electroweak representation was developed in the next most simple symmetry: $SU(2) \times U(1)$: this one introduces satisfactorily photons and Z bosons, as combinations of the $SU(2)$ and $U(1)$ fields. Thus the existence of the Z boson was predicted by this theory.

[2] $\tau_1 = \begin{pmatrix} 0 & 1 \\ 1 & 0 \end{pmatrix}$; $\tau_2 = \begin{pmatrix} 0 & -i \\ i & 0 \end{pmatrix}$; $\tau_3 = \begin{pmatrix} 1 & 0 \\ 0 & -1 \end{pmatrix}$.

[3] The Standard Model does not describe right-handed neutrinos, that are not sensitive to any of the three interactions described by the model. Besides, neutrinos of right helicity have not been observed experimentally and it is not known whether or not they exist.

However, the two components of a left-handed doublet in eq. (1.4) do not have the same electric charge: this means that the symmetry $U(1)_Q$ can not be applied to the doublets. This problem is solved by considering a $SU(2)_L \times U(1)_Y$ symmetry to describe the electroweak interactions. The quantum number Y is the hypercharge, a linear combination of the electric charge Q, and the weak isospin t_3:

$$Y = 2(Q - t_3) \; . \tag{1.5}$$

Its value is $-\frac{1}{2}$ for the components of the $\begin{pmatrix} \nu \\ e \end{pmatrix}_L$ doublet, and $\frac{1}{6}$ for the components of the $\begin{pmatrix} u \\ d \end{pmatrix}_L$ doublet.

1.1.2.3 The Electroweak Interaction

We call B_μ the field corresponding to the $U(1)_Y$ symmetry: like in the QED example, to a $U(1)$ symmetry acting as $\psi(x) \to e^{i\Lambda(x)}\psi(x)$ corresponds a field B_μ, coupled to the particles by a coupling g_1, which transforms as $B_\mu \to B_\mu + \frac{1}{g_1}\partial_\mu \Lambda$.

Similarly, W_μ^a $(a = 1, 2, 3)$ are the gauge fields corresponding to $SU(2)_L$. The transformation of a left-handed fermion field ψ_L under the $SU(2)_L$ symmetry writes: $\psi_L(x) \to e^{i\frac{\tau_a}{2}\Lambda_a(x)}\psi_L(x)$. The fields $W_\mu^a(x)$, coupled to the left-handed particles by a coupling g_2, transform as $W_\mu^a \to W_\mu^a + \frac{1}{g_2}\partial_\mu \Lambda^a + \epsilon^{abc} W_{\mu b}\Lambda_c$.

The covariant derivative corresponding to the $SU(2)_L \times U(1)_Y$ symmetry writes:

$$D_\mu = \partial_\mu - ig_1 \frac{Y}{2} B_\mu(x) - ig_2 \frac{\tau_a}{2} W_\mu^a(x) \; . \tag{1.6}$$

Similarly to the QED case, the $U(1)_Y$ field strength tensor writes:

$$B_{\mu\nu} = \partial_\mu B_\nu - \partial_\nu B_\mu \; . \tag{1.7}$$

Given the properties of the Pauli matrices ($[\tau_a, \tau_b] = 2i\epsilon_{abc}\tau_c$), the $SU(2)_L$ field strength tensor writes:

$$W_{\mu\nu} = \frac{i}{g_2}[\partial_\mu - ig_2 \frac{\tau_a}{2} W_\mu^a(x), \partial_\nu - ig_2 \frac{\tau_a}{2} W_\nu^a(x)] = W_{\mu\nu}^a \frac{\tau_a}{2} \; , \tag{1.8}$$

where:

$$W_{\mu\nu}^a = \partial_\mu W_\nu^a - \partial_\nu W_\mu^a + g_2 \epsilon^{abc} W_{\mu b} W_{\nu c} \; . \tag{1.9}$$

This leads to the following Lagrangian, where the fermion mass term has been voluntarily removed:

$$\mathscr{L}_{massless} = \bar{\psi}\, i\gamma^\mu D_\mu\, \psi - \frac{1}{4}(B_{\mu\nu}B^{\mu\nu} + W_{\mu\nu}^a W^{a\,\mu\nu}) \; . \tag{1.10}$$

One can check in particular that the first term is invariant under the $SU(2)_L$ symmetry, because for a spinor $\psi = \psi_R + \psi_L$:

$$\bar{\psi}\gamma^\mu\psi = \bar{\psi}_R\gamma^\mu\psi_R + \bar{\psi}_L\gamma^\mu\psi_L \ . \tag{1.11}$$

The problem of the mass

The usual fermion mass term $-m\bar{\psi}\psi$ was removed from the Lagrangian written in eq. (1.10), because it would not be invariant under the $SU(2)_L$ symmetry. For a spinor $\psi = \psi_R + \psi_L$:

$$\bar{\psi}\psi = \bar{\psi}_R\psi_L + \bar{\psi}_L\psi_R \ , \tag{1.12}$$

so a unitary transformation applied to the left-handed field would not leave this mass term invariant. One must find a way to include fermion masses while preserving the $SU(2)_L$ symmetry.

Last but not least, the Lagrangian written in eq. (1.10) does not describe precisely the electroweak interactions: weak interactions are only effective at short distances, which means that their vector bosons are massive. So a weak boson mass term must also be added to the Lagrangian. However, a general vector boson mass term as $-\frac{1}{2}M_V^2 V_\mu V^\mu$ is not invariant under the $SU(2)_L$ symmetry. Once again, a particular technique must be used to add vector boson mass terms in the Lagrangian: the electroweak symmetry breaking.

1.1.3 The Electroweak Symmetry Breaking

1.1.3.1 The Higgs Field

The classic solution to the mass problem of the electroweak model, is the addition of a complex scalar doublet: $\Phi = \begin{pmatrix} \phi_1 + i\phi_2 \\ \phi_3 + i\phi_4 \end{pmatrix}$, of hypercharge $Y = 1$. The potential of a scalar field generally writes (up to a constant):

$$V(\Phi) = \mu^2|\Phi|^2 + \lambda|\Phi|^4 \ , \tag{1.13}$$

with $\mu^2 > 0$, $\lambda > 0$. In the studied case, on chooses a negative parameter in front of the $|\Phi|^2$ term:

$$V_{SB}(\Phi) = -\mu^2|\Phi|^2 + \lambda|\Phi|^4 \ ; \ \mu^2 > 0 \ . \tag{1.14}$$

This potential is minimal for non-zero values of the field: $|\Phi|^2 = \frac{\mu^2}{2\lambda} \equiv \frac{v^2}{2}$, as illustrated in Fig. 1.1. The general shape of the potential is symmetrical in all directions; however, as soon

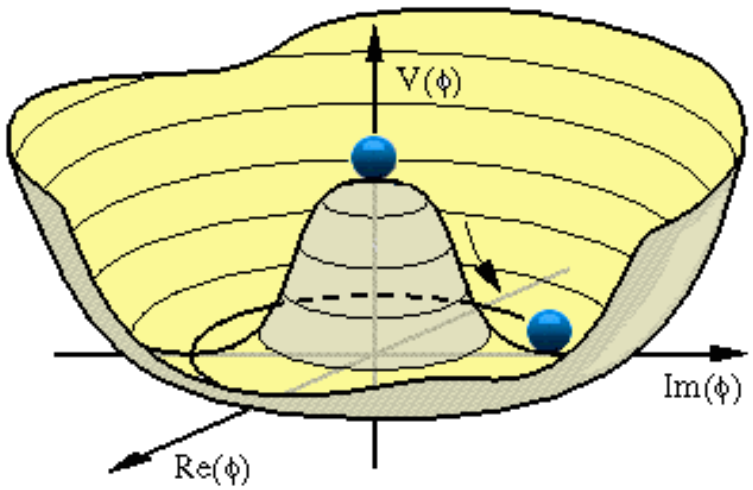

Figure 1.1: The Higgs field potential: as an illustration, the case of a one-dimensional complex scalar field is shown here.

as one minimal value, or *vacuum* is chosen (i.e. one field Φ such that $|\Phi|^2 = \phi_1^2+\phi_2^2+\phi_3^2+\phi_4^2 = \frac{v^2}{2}$), the symmetry breaks spontaneously.

A potential is defined up to a constant, hence the potential (1.14) can also be written as:

$$V_{SB}(\Phi) = \lambda\left(|\Phi|^2 - \frac{1}{2}v^2\right)^2 . \tag{1.15}$$

Without loss of generality one can consider the vacuum as $\langle\Phi\rangle = \frac{1}{\sqrt{2}}\begin{pmatrix} 0 \\ v \end{pmatrix}$. Similarly, the deviations from the vacuum value in the ϕ_1, ϕ_2 and ϕ_4 directions can be cancelled by the choice of an appropriate gauge, the so-called unitary gauge. In the end, the remaining perturbation is along the ϕ_3 axis, like the vacuum expectation value $\frac{v}{\sqrt{2}}$:

$$\Phi(x) = \frac{1}{\sqrt{2}}\begin{pmatrix} 0 \\ v + h(x) \end{pmatrix} \tag{1.16}$$

Using this form of Φ in the potential (1.17) brings out the mass of the field h, and its triple and quartic couplings:

$$V_{SB}(h) = \lambda\left(v^2h^2 + vh^3 + \frac{h^4}{4}\right) = \frac{m_h^2}{2}h^2 - \frac{ig_{h^3}}{3!}h^3 - \frac{ig_{h^4}}{4!}h^4 . \tag{1.17}$$

The field $h(x)$ describes a new particle: the Higgs boson, of mass $m_h = \sqrt{2\lambda v^2} = \sqrt{2}\,\mu$.

1.1.3.2 The Weak Boson Masses

The Lagrangian corresponding to the scalar field Φ writes:

$$\mathscr{L}_{SB} = |D_\mu \Phi|^2 - \lambda \left(|\Phi|^2 - \frac{1}{2} v^2 \right)^2 - \frac{1}{4} (B_{\mu\nu} B^{\mu\nu} + W^a_{\mu\nu} W^{\mu\nu}_a) \; . \tag{1.18}$$

The vacuum expectation value $\frac{v}{\sqrt{2}}$ generates the weak boson masses through the covariant derivative:

$$|D_\mu \Phi|^2 = \left| \left(\partial_\mu - i g_1 \frac{Y}{2} B_\mu(x) - i g_2 \frac{\tau_a}{2} W^a_\mu(x) \right) \Phi \right|^2 \; . \tag{1.19}$$

$$|D_\mu \Phi|^2 = \frac{1}{2} \partial_\mu h \partial^\mu h + \frac{1}{8} \left| \begin{pmatrix} g_2 W^3_\mu + g_1 B_\mu & g_2 (W^1_\mu - i W^2_\mu) \\ g_2 (W^1_\mu + i W^2_\mu) & -g_2 W^3_\mu + g_1 B_\mu \end{pmatrix} \begin{pmatrix} 0 \\ v + h(x) \end{pmatrix} \right|^2 \; . \tag{1.20}$$

Let us define the four gauge boson fields:

$$W^\pm_\mu = \frac{1}{\sqrt{2}} (W^1_\mu \pm i W^2_\mu) \; ; \; Z_\mu = \frac{1}{\sqrt{g_1^2 + g_2^2}} (g_2 W^3_\mu - g_1 B_\mu) \; ; \; A_\mu = \frac{1}{\sqrt{g_1^2 + g_2^2}} (g_1 W^3_\mu + g_2 B_\mu) \tag{1.21}$$

The potential corresponds exactly to the mass terms of three of these fields: $W^\pm_\mu$ ($M_W = \frac{g_2 v}{2}$) and Z_μ ($M_Z = \frac{v}{2} \sqrt{g_1^2 + g_2^2}$).

$$|D_\mu \Phi|^2 = \frac{1}{2} \partial_\mu h \partial^\mu h \; + \; \left(\frac{1}{2} g_2 (v + h) \right)^2 W^+_\mu W^{\mu -} \; + \; \frac{1}{2} \left(\frac{v + h}{2} \sqrt{g_1^2 + g_2^2} \right)^2 Z_\mu Z^\mu \; . \tag{1.22}$$

The massless field A_μ corresponding to the photon, is a mixed state; its masslessness indicates the unbroken charge ($Q = t_3 + \frac{Y}{2}$) invariance, since $(\tau_3 + \frac{Y}{2}) \langle \Phi \rangle = 0$.

1.1.3.3 The Weak Angle and the ρ Parameter

Finally, one can introduce the weak angle θ_W, such that $\cos\theta_W = \frac{g_2}{\sqrt{g_1^2 + g_2^2}}$ and $\sin\theta_W = \frac{g_1}{\sqrt{g_1^2 + g_2^2}}$. As a consequence:

$$A_\mu = \cos\theta_W B_\mu + \sin\theta_W W^3_\mu \; ; \; Z_\mu = \cos\theta_W W^3_\mu - \sin\theta_W B_\mu \; ; \; \frac{M_W}{M_Z} = \cos\theta_W \; . \tag{1.23}$$

The measured values of $M_Z = 91.1875 \pm 0.0021 \, \mathrm{GeV/c^2}$ and $M_W = 80.399 \pm 0.025 \, \mathrm{GeV/c^2}$, in very good agreement with the Standard Model predictions, give $\sin\theta_W \approx 0.23$.

The ρ parameter is defined as:

$$\rho = \frac{M_W^2}{M_Z^2 \cos^2\theta_W} \; , \tag{1.24}$$

it will be used later in this chapter. According to its definition, its tree-level value in the Standard Model is $\rho = 1$. Different experimental measurements indicate that ρ is very close to unity within a *per mille* precision.

Note: v is fixed by the low energy effective Fermi theory (G_F is the Fermi constant):

$$v = (\sqrt{2}G_F)^{-1/2} \approx 246 \text{ GeV} . \tag{1.25}$$

1.1.3.4 The Fermion Masses

Given a fermion field f, we know that $\bar{f}f = \bar{f}_R f_L + \bar{f}_L f_R$ is not invariant under an $SU(2)_Y$ transformation, so a simple fermion mass term ($-m\bar{f}f$) can not be added to the Lagrangian.

The Higgs field mass solves also the problem of fermion masses, by the introduction of Yukawa couplings:

$$\mathscr{L}_Y = -\lambda_f \left(\bar{f}_R \Phi^\dagger f_L + \bar{f}_L \Phi f_R \right) \tag{1.26}$$

$$\mathscr{L}_Y = -\frac{\lambda_f v}{\sqrt{2}} \bar{f}f \; - \; \frac{\lambda_f}{\sqrt{2}} \bar{f}fh \tag{1.27}$$

These couplings naturally introduce fermion mass terms, simultaneously with Higgs-fermion-fermion coupling terms; the corresponding coupling constant is proportional to the fermion mass.

Coming back to the fermion fields in eq. (1.4), the case is rather simple for leptons, since only charged leptons get a mass. The Yukawa couplings provide the terms:

$$-\lambda_e \left(\bar{e}_R \Phi^\dagger L + \bar{L} \Phi e_R \right) = -m_e \bar{e}e \; - \; i g_{Hee} \bar{e}eh \; , \tag{1.28}$$

where $m_e = \frac{\lambda_e v}{\sqrt{2}}$ and $g_{Hee} = i\frac{\lambda_e}{\sqrt{2}} = i\frac{m_e}{v}$. Notice that this is the first differentiation among the fermion generations, which until this point were perfect reflections of each other. Hence the choice of the generation states was arbitrary. The first generation $\left(\begin{pmatrix} \nu_e \\ e \end{pmatrix}_L , e_R \right)$ is defined as the mass eigenstate with the lightest eigenvalue m_e; the second one $\left(\begin{pmatrix} \nu_\mu \\ \mu \end{pmatrix}_L , \mu_R \right)$ corresponds to the eigenvalue m_μ, and the third $\left(\begin{pmatrix} \nu_\tau \\ \tau \end{pmatrix}_L , \tau_R \right)$ to the eigenvalue m_τ.

The case is slightly more complicated for quarks. First of all, a conjugate to the Higgs field is necessary to introduce couplings with Q and u_R: Φ_c, that develops a non-zero mean value in its first component. It is defined as:

$$\Phi_c = i\tau_2\Phi^* \; ; \; \langle\Phi_c\rangle = \frac{1}{\sqrt{2}}\begin{pmatrix} v \\ 0 \end{pmatrix} \tag{1.29}$$

The Yukawa couplings then write:

$$-\lambda_u\left(\bar{u}_R\Phi_c^\dagger Q + \bar{Q}\Phi_c u_R\right) - \lambda_d\left(\bar{d}_R\Phi^\dagger Q + \bar{Q}\Phi d_R\right) \tag{1.30}$$

A complication appears in the definition of the generations, i.e. the mass eigenstates. Like for leptons, each right-handed singlet can be defined according to its mass eigenstate; however, as far as left-handed doublets are concerned, no state can be simultaneously an 'up' mass eigenstate for the first component and a 'down' mass eigenstate for the second component. This difference is described by the quark flavor mixing matrix, or CKM matrix (for Cabibbo-Kobayashi-Maskawa).

The three left-handed generations according to the 'up' mass eigenstates are defined as:

$$\begin{pmatrix} u \\ d \end{pmatrix}_L \; ; \; \begin{pmatrix} c \\ s \end{pmatrix}_L \; ; \; \begin{pmatrix} t \\ b \end{pmatrix}_L \; , \tag{1.31}$$

while the 'down' left-handed mass eigenstates are referred to as d'_L, s'_L, b'_L. The CKM matrix V is defined as:

$$\begin{pmatrix} d' \\ s' \\ b' \end{pmatrix}_L = V \begin{pmatrix} d \\ s \\ b \end{pmatrix}_L \tag{1.32}$$

This matrix was measured to be non-diagonal, which proves the difference in the eigenstates, and is the origin of the mixing of quark flavors[4]. The general shape of the CKM matrix is a combination of rotations, and a phase δ_{13} that induces violations of the CP symmetry:

$$V = R_1(\theta_{23})\, R_2(\theta_{13}, \delta_{13})\, R_3(\theta_{12}) \tag{1.33}$$

$$V = \begin{pmatrix} 1 & 0 & 0 \\ 0 & \cos\theta_{23} & \sin\theta_{23} \\ 0 & -\sin\theta_{23} & \cos\theta_{23} \end{pmatrix} \begin{pmatrix} \cos\theta_{13} & 0 & \sin\theta_{13}e^{-i\delta_{13}} \\ 0 & 1 & 0 \\ -\sin\theta_{13}e^{i\delta_{13}} & 0 & \cos\theta_{13} \end{pmatrix} \begin{pmatrix} \cos\theta_{12} & \sin\theta_{12} & 0 \\ -\sin\theta_{12} & \cos\theta_{12} & 0 \\ 0 & 0 & 1 \end{pmatrix} \tag{1.34}$$

[4] A down quark emitted by a weak interaction in the state d_L (weak interaction eigenstate) is then projected into a mass eigenstate to propagate: d'_L, s'_L or b'_L, with probabilities indicated by the CKM matrix. If it is then measured again by a weak interaction, its state will project again, into a weak interaction eigenstate (d_L, s_L or b_L) which can be different from its emission state d_L.

1.1.4 Strong Interaction

The strong interaction is described in a theory called Quantum Chromodynamics (QCD); it applies to particles that carry a color charge: among the particles of matter, quarks are the only ones concerned. This interaction is carried by eight gauge bosons: the massless gluons, which themselves carry a color charge. It is described by a $SU(3)$ symmetry, corresponding to the conservation of the color charge: $SU(3)_c$. This symmetry is orthogonal to the electroweak symmetry mentioned in the last paragraph, hence the Standard Model is globally described by a $SU(3)_c \times SU(2)_L \times U(1)_Y$ symmetry.

Finally, gluons are massless, and this $SU(3)_c$ symmetry is not broken. Through electroweak symmetry breaking, $SU(3)_c \times SU(2)_L \times U(1)_Y$ is reduced to $SU(3)_c \times U(1)_Q$, which is believed to be an exact gauge symmetry of nature.

Short-range nuclear forces and massless gluons

Confinement is the property that no isolated colored charge can exist but only color singlet particles. For example, the potential between a quark and an antiquark has both a Coulomb part at short distances (similarly to an electromagnetic potential) and a linearly rising term at long distances: $V_{q\bar{q}} \approx C_F \left[\frac{\alpha(r)}{r} + \cdots + \sigma r\right]$. As a consequence, a quark and an antiquark created at a point and moving away from each other, generate additional pairs to neutralize color: the final state is reorganized into two jets of colorless hadrons.

Confinement is essential to explain why nuclear forces have very short range while massless gluon exchange would be long range. Nucleons are color singlets and they cannot exchange color octet gluons but only colorless states. The lightest color singlet hadronic particles are pions. So the range of nuclear forces is fixed by the pion mass: $r \approx m_\pi^{-1} \approx 10^{-13}$ cm; $V \approx e^{-m_\pi r}/r$.

1.1.5 The Standard Model Lagrangian

In addition to the electroweak model, the strong gauge fields G_μ^a $(a = 1 - 8)$ correspond to $SU(3)_c$. The transformation of a fermion field ψ under the $SU(3)_c$ symmetry writes: $\psi(x) \rightarrow e^{i\frac{\lambda_a}{2}\Lambda_a(x)}\psi(x)$, where λ_a $(a = 1 - 8)$ are the Gell-Mann matrices. The fields $G_\mu^a(x)$, coupled to the particles by a coupling g_3, transform as $G_\mu^a \rightarrow G_\mu^a + \frac{1}{g_3}\partial_\mu \Lambda^a + \epsilon^{abc} G_{\mu b} \Lambda_c$.

The covariant derivative corresponding to the $SU(3)_c \times SU(2)_L \times U(1)_Y$ symmetry writes:

$$D_\mu = \partial_\mu - ig_1 \frac{Y}{2} B_\mu(x) - ig_2 \frac{\tau_a}{2} W_\mu^a(x) - ig_3 \frac{\lambda_a}{2} G_\mu^a(x) \ , \tag{1.35}$$

and the gauge kinetic term of the Lagrangian becomes:

$$-\frac{1}{4}(B_{\mu\nu}B^{\mu\nu} + W_{\mu\nu}^a W_a^{\mu\nu} + G_{\mu\nu}^a G_a^{\mu\nu}) \ , \tag{1.36}$$

where:

$$G_{\mu\nu}^a = \partial_\mu G_\nu^a - \partial_\nu G_\mu^a + g_3 \epsilon^{abc} G_{\mu b} G_{\nu c} \ . \tag{1.37}$$

Summarizing the information of this section, the general Standard Model Lagrangian writes:

$$\mathscr{L}_{SM} = \mathscr{L}_f + \mathscr{L}_Y + \mathscr{L}_g + \mathscr{L}_H \ , \tag{1.38}$$

where $\mathscr{L}_f = \bar{\psi} i \gamma^\mu D_\mu \psi$ is the fermionic propagation term (ψ runs over all fermion fields and D_μ is as defined in eq. (1.35)), $\mathscr{L}_Y$ is the Yukawa term that provides masses to fermions (cf eq. (1.28) and (1.30)), $\mathscr{L}_g$ is the gauge kinetic term as defined in eq. (1.36), and $\mathscr{L}_H = |D_\mu \Phi|^2 - \lambda \left(|\Phi|^2 - \frac{1}{2}v^2\right)^2$ is the Higgs term, which introduces the Higgs field h and the weak boson masses.

The main properties of the particles of matter and the bosons described by the Standard Model are summarized in Tables 1.1 and 1.2 respectively.

	Leptons			Quarks		
	Name	Mass (GeV/c^2)	Charge	Name	Mass (GeV/c^2)	Charge
first generation	electron (e^-)	$0.511 \cdot 10^{-3}$	-1	up (u)	$(1.5 \text{ to } 3 \cdot 10)^{-3}$	2/3
	neutrino (ν_e)	$0^{(*)}$	0	down (d)	$(3.5 \text{ to } 6 \cdot 10)^{-3}$	$-1/3$
second generation	muon (μ^-)	0.106	-1	charm (c)	1.27	2/3
	neutrino (ν_μ)	$0^{(*)}$	0	strange (s)	$104 \cdot 10^{-3}$	$-1/3$
third generation	tau (τ^-)	1.777	-1	top (t)	172.4	2/3
	neutrino (ν_τ)	$0^{(*)}$	0	bottom (b)	4.2	$-1/3$

Table 1.1: Fermions in the Standard Model. For each of these fermions, the Standard Model contains also its antiparticle, which has the same properties, and opposite charges. (*) indicates the particularity of neutrinos, described as massless in the Standard Model, though evidence of their masses was made recently.

Name	Spin	Mass (GeV/c^2)	Charge
photon (γ)	1	0	0
$W^{\pm}$	1	80.403	± 1
Z^0	1	91.188	0
gluons (g)	1	0	0
Higgs boson $(H)^{(**)}$	0	*unknown*	0

Table 1.2: Bosons in the Standard Model. (**) indicates the particularity of the Higgs boson, which was not (yet) experimentally observed.

Running couplings and asymptotic freedom

The couplings mentioned as g_1, g_2 and g_3 in this description of the Standard Model are not constant: they depend on the energy scale of the studied particles.

In QED, this coupling raises with the considered energy scale μ, and the theory is only valid up to an energy cut-off Λ. On the contrary, in a theory like QCD, the running coupling vanishes asymptotically at large μ^2: this property is called "asymptotic freedom".

1.2 The Limitations of the Standard Model

In 1900, in a lecture entitled 'Nineteenth-Century Clouds over the Dynamical Theory of Heat and Light', Lord Kelvin compared physics to a blue sky, on which only two clouds remained. These clouds were the unsatisfactory explanations that the physics of the time could give for two phenomena: the Michelson–Morley experiment and black body radiation. Two major physical theories were developed during the twentieth century starting from these issues: for the former, the theory of relativity; for the second, quantum mechanics.

Similarly, the Standard Model was a remarkable achievement and succeeded in predicting several particles, like the Z boson and the top quark, that were experimentally confirmed later. However, the investigation of its limitations can lead to new major branches of physics.

1.2.1 Theoretical Limitations

1.2.1.1 General Discussion

The Standard Model has been a very successful theory, in very good agreement with most of the experimental results. However it does not answer all the questions that can be raised concerning fundamental interactions. For this reason it is mainly considered as an effective theory, i.e. the low energy limit of some deeper theory.

A high number of free parameters

The research of elementary particles and interactions is also a research of simplicity. The ideal theory would be made of very few bricks, and very few free parameters, out of which everything can be built, regarding some precise symmetry conditions. The Standard Model, as it was introduced, presents nineteen free parameters:

- three gauge couplings: g_1 ($U(1)_Y$), g_2 ($SU(2)_L$), g_3 ($SU(3)_c$);
- two parameters in the Higgs sector: μ and λ;
- nine quark (u, d, c, s, t, b) and charged lepton (e, μ, τ) masses;
- three mixing angles and one CP-violating phase for the quark system (in the CKM matrix);
- the QCD parameter θ (coupling of the $F^a_{\mu\nu}\tilde{F}^{a\mu\nu}$ term)[5].

As soon as numbers grow, one starts to wonder whether they are the reflect of another symmetry, or rule, that has not been identified yet. For example, physicists were very tempted to unify the three gauge couplings (g_1, g_2 and g_3) at high energy. These couplings depend on the considered energy scale μ, and are represented in Fig. 1.2: the three lines get very close for an energy scale of the order of 10^{15} GeV, however they do not converge. Grand unified theories unify these couplings at a scale of $\sim 10^{16}$ GeV.

The quantization of charge

The electric charges of all Standard Model particles are multiples of $\frac{e}{3}$, where $-e$ is the electron charge, however this property is not explained in the Standard Model. More generally, quantum numbers of quarks and leptons are such that all anomalies cancel. This question is partly dealt with in grand unified theories, which include electric charge among the non-abelian gauge symmetry generators.

The problem of fermion masses

A significant gap is noticed in the fermion masses, between the different quark and lepton

[5]There are natural terms in the QCD Lagrangian that are able to break the CP-symmetry, in particular $-\frac{n_f g^2 \theta}{32\pi^2} F^a_{\mu\nu}\tilde{F}^{a\mu\nu}$. This angle θ is very small according to experimental measurements, however the reason for this value is not understood.

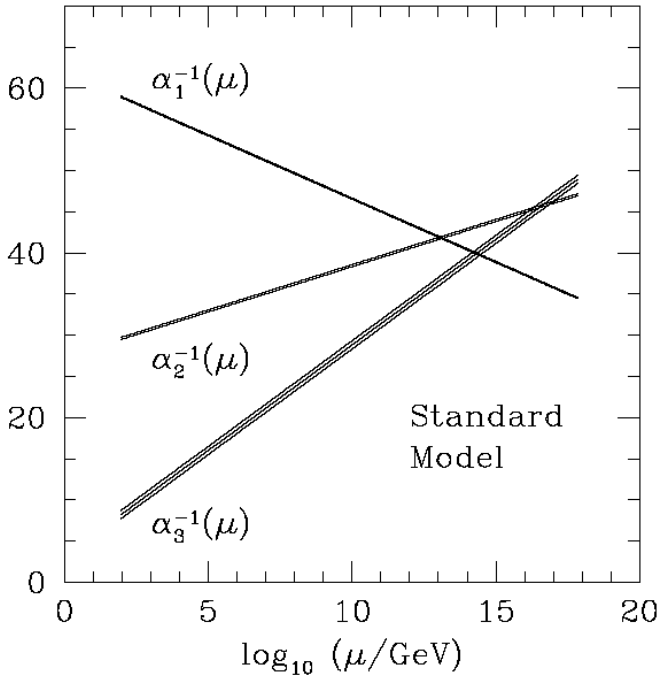

Figure 1.2: Evolution of the inverse gauge couplings $\alpha_a^{-1}(\mu)$ in the Standard Model.

families. Again, this is not explained by the Standard Model. Reminding the formula:

$$m_f^2 = |\lambda_f \langle \Phi \rangle|^2 = \lambda_f^2 \frac{v^2}{2} \tag{1.39}$$

and the value of the vacuum expectation value: $v = 246$ GeV, one can notice that only the coupling of the top quark is close to unity ($m_t = 173.3\,\mathrm{GeV/c^2}$), the other ones being unnaturally small.

Mixing angles and phases

In the quark sector, mass eigenstates do not coincide with interaction eigenstates: they are related by the Cabibbo-Kobayashi-Maskawa matrix, which involves three mixing angles and a relative phase. The large differences between these angles are not understood.

Gravity

The theory of gravity is non-renormalizable, because unlike other coupling constants, Newton's constant has a dimension ($[G_N] = M^{-2}$). As a consequence, this interaction is not described in the Standard Model.

Quantum effects of gravity become important at a scale called the Planck scale: $\left(\frac{\hbar c}{G_N}\right)^{1/2} =$

$M_P \sim 1.22 \times 10^{19}\,\mathrm{GeV/c^2}$, so the Standard Model fails to describe interactions at energies of the order of $M_P\,c^2$ or greater. Adding gravity to the field theories will probably require drastic changes, such as the one suggested in string theories.

1.2.1.2 The Higgs Boson Mass

The bare Higgs boson mass is given from eq. (1.17): $m_h = \sqrt{2}\mu = \sqrt{2\lambda v^2}$. The vacuum expectation value v is fixed: $v = (\sqrt{2}G_F)^{-1/2} \approx 246$ GeV, however the Higgs mass, and the quartic coupling λ, remain unknown.

Unitarity

The unitarity constraint on the S-matrix (the scattering matrix) is a consequence of the conservation of probabilities at the quantum level. It imposes constraints on scattering cross sections, especially at high energy. These constraints can be interpreted as upper bounds on the Higgs boson mass; the most stringent constraint results in:

$$m_h \lesssim 780\,\mathrm{GeV/c^2} \tag{1.40}$$

Triviality

In the renormalization group approach, the scalar self-coupling λ becomes a running coupling $\lambda(\mu)$, depending on the momentum scale μ characteristic of the process considered. This coupling increases monotonically with μ and a pole appears, at which λ tends to infinity: the so-called Landau pole Λ_{Landau}, that depends on the initial value $\lambda(v)$.

This pole can not be removed unless the Higgs is made massless; in order to get rid of the divergence induced by this pole, one defines an energy cut-off $\mu_c = \Lambda < \Lambda_{Landau}$ under which λ remains finite: the theory will only be considered up to this cut-off.

The condition $\Lambda < \Lambda_{Landau}$ results in a condition on $\lambda(v)$. Since $\lambda(v) = \frac{m_h^2}{2v^2}$, it translates in a condition on m_h:

$$m_h^2 < \frac{4\pi^2 v^2}{3\ln(\Lambda/v)}\ . \tag{1.41}$$

For the choice of a cut-off close to the typical GUT scale $\Lambda = 10^{16}$ GeV, this results in the condition $m_h < 170\,\mathrm{GeV/c^2}$.

Vacuum stability

If the bare Higgs boson mass is low, i.e. if $\lambda(v)$ is low, the couplings to heavy particles, in particular the coupling to the top quark, play a major role in the variations of $\lambda(\mu)$. They tend to lower this parameter, initially already small; however a negative value of $\lambda(\mu)$ would make the scalar potential unbounded from below at large values of the Higgs field. This would result in an instability of the theory.

This is prevented, again, by considering only energy scales lower than a cut-off Λ: one needs $\lambda(\Lambda) > 0$, which results in (if one neglects gauge interactions):

$$m_h^2 > \frac{3m_t^4}{\pi^2 v^2} \ln(\Lambda/v) \; . \tag{1.42}$$

For the choice of a cut-off close to the typical GUT scale $\Lambda = 10^{16}$ GeV, this results in the condition $m_h > 134\,\mathrm{GeV/c^2}$.

The hierarchy problem

The Standard Model is considered as effective, up to a given energy scale Λ. This cut-off applied in the theory introduces quadratic divergences in the description of the scalar field. In order to recover the right, physical Higgs mass $m_h \sim 10^2\,\mathrm{GeV/c^2}$, a significant fine-tuning is necessary. This is due to the great scale difference between the two energies Λ and $m_h c^2$.

Figure 1.3 shows the Higgs mass as a function of the cut-off scale Λ: the constraints corresponding to the triviality and the vacuum stability mentioned before are indicated; in the remaining space, the regions corresponding to a fine-tuning of $\frac{\delta m_h^2}{m_h^2} > 10$, and $\frac{\delta m_h^2}{m_h^2} > 100$, are indicated by hatches.

For a cut-off scale higher than 100 TeV, a fine-tuning of $\frac{\delta m_h^2}{m_h^2} > 100$ becomes necessary. Such a fine tuning would make the theory unnatural. One expects the observable properties of a natural theory (masses, charges, ...) to be stable under small variations of the fundamental parameters (the bare parameters).

1.2.2 Experimental Constraints

1.2.2.1 Electroweak Fit for the Higgs Boson Mass

The Higgs boson mass intervenes in several parameters of the Standard Model, through radiative effects. As a consequence, a precise measurement of these parameters allows to set some constraints on the Higgs boson mass.

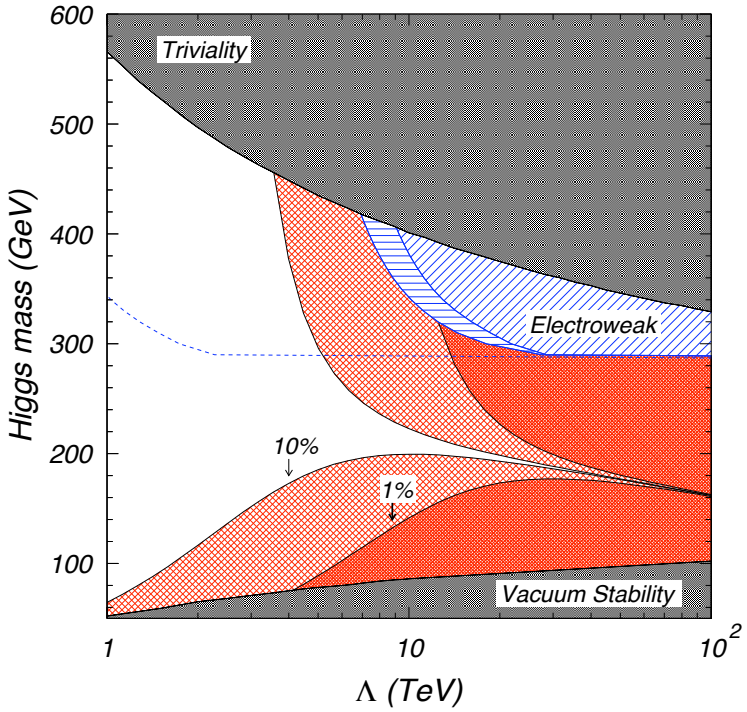

Figure 1.3: The classic constraints on the $m_h - \Lambda$ plane, including triviality (dark region at top) and vacuum stability (dark region at bottom), as well as the tuning contours. The darkly hatched region marked "1%" represents tunings $\frac{\delta m_h^2}{m_h^2} > 100$; the "10%" region means $\frac{\delta m_h^2}{m_h^2} > 10$. The empty region is consistent with all constraints and has a fine tuning $\frac{\delta m_h^2}{m_h^2} < 10$. [1]

Let us take the example of the ρ parameter defined in eq. (1.24): at tree level, the Standard Model predicts a value of 1 for this parameter. First order loop corrections were calculated:

$$\Delta\rho^{SM} \approx \frac{\alpha}{\pi}\frac{m_t^2}{M_Z^2} - \frac{\alpha}{2\pi}\ln\left(\frac{m_h}{M_Z}\right) \ . \tag{1.43}$$

Once the top quark mass is precisely measured, one can deduce from the measurement of the ρ parameter a limit on the Higgs boson mass.

Based on the various parameters for which the Higgs mass intervenes, the latest measurement of the top quark mass ($m_t = 173.3 \pm 1.1\,\mathrm{GeV/c^2}$ [2]) suggests the following constraint on the Higgs boson mass in the Standard Model: $m_h < 186\,\mathrm{GeV/c^2}$ at 95% confidence level (cf Fig. 1.4.a).

On the other hand, the direct searches carried at LEP excluded a Higgs boson of mass lower than $114.4\,\mathrm{GeV/c^2}$. The latest results from the Tevatron direct searches (cf Fig. 1.4.b) exclude the mass range $158 - 175\,\mathrm{GeV/c^2}$ [3].

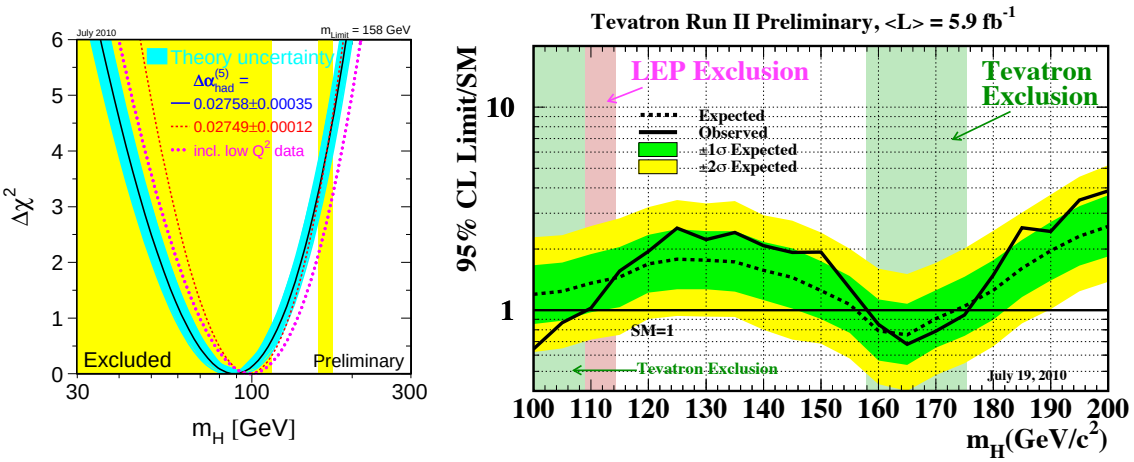

(a) (b)

Figure 1.4: (a): the blue-band plot showing the Higgs mass upper limit [4]. (b): observed and expected (median, for the background-only hypothesis) 95% C.L. upper limits on the ratios to the SM cross section, as functions of the Higgs boson mass for the combined CDF and D0 analyses [3].

1.2.2.2 Neutrino Masses

The first hint for neutrino oscillations came in the late 1960s, when a deficit in the flux of solar neutrinos was observed in Ray Davis's Homestake Experiment, using a chlorine-based detector. These results were confirmed by later experiments (SNO), and deficits were also observed for atmospheric neutrinos (SuperK), and for neutrinos issuing reactor interactions (KamLAND).

These deficits are interpreted as neutrino flavor changes, due to a mismatch between neutrino flavor eigenstates ($|\nu_\alpha\rangle$, $\alpha = e, \mu, \tau$) and their mass eigenstates ($|\nu_i\rangle$, $i = 1, 2, 3$). This implies that neutrinos have several different mass eigenvalues, while the Standard Model describes them as massless particles. Similarly to the quark flavor mixing and the CKM matrix, neutrino oscillations are described by a unitary matrix $U_{\alpha i}$, called the Pontecorvo-Maki-Nakagawa-Sakata (PMNS) matrix, or the lepton mixing matrix, such that:

$$|\nu_\alpha\rangle = \sum_i U^*_{\alpha i}|\nu_i\rangle \ ; \ |\nu_i\rangle = \sum_\alpha U_{\alpha i}|\nu_\alpha\rangle \ . \tag{1.44}$$

The probability for a neutrino emitted with the lepton flavor α, to be measured, after a

time t, with a flavor β, writes:

$$P_{\alpha\to\beta} = |\langle\nu_\beta|\nu_\alpha(t)\rangle|^2 = \left|\sum_i U_{\beta i}U^*_{\alpha i}e^{-i(E_i t-\vec{p}_i\cdot\vec{x})}\right|^2 . \tag{1.45}$$

The 3×3 PMNS matrix is naturally composed of three rotations, involving three mixing angles, called the Euler angles: θ_{12}, θ_{13}, θ_{23}. If neutrino oscillations happen to violate the CP symmetry, a phase factor δ (or Dirac phase) must be added. Finally, two other phase factors, α_1 and α_2 (or Majorana phases) can be added if neutrinos are Majorana particles, i.e. if they are their own antiparticle. Taking all these parameters into account, the lepton mixing matrix finally writes:

$$U = \begin{pmatrix} U_{e1} & U_{e2} & U_{e3} \\ U_{\mu1} & U_{\mu2} & U_{\mu3} \\ U_{\tau1} & U_{\tau2} & U_{\tau3} \end{pmatrix} \tag{1.46}$$

$$U = \begin{pmatrix} 1 & 0 & 0 \\ 0 & \cos\theta_{23} & \sin\theta_{23} \\ 0 & -\sin\theta_{23} & \cos\theta_{23} \end{pmatrix} \begin{pmatrix} \cos\theta_{13} & 0 & \sin\theta_{13}e^{-i\delta} \\ 0 & 1 & 0 \\ -\sin\theta_{13}e^{i\delta} & 0 & \cos\theta_{13} \end{pmatrix} \begin{pmatrix} \cos\theta_{12} & \sin\theta_{12} & 0 \\ -\sin\theta_{12} & \cos\theta_{12} & 0 \\ 0 & 0 & 1 \end{pmatrix} \begin{pmatrix} e^{i\alpha_1/2} & 0 & 0 \\ 0 & e^{i\alpha_2/2} & 0 \\ 0 & 0 & 1 \end{pmatrix} \tag{1.47}$$

As a consequence, the neutrino mass matrix $m_{\alpha\beta}$ for the flavor eigenstates writes:

$$m = U^\dagger diag(m_1, m_2, m_3)U , \tag{1.48}$$

where m_i ($i = 1, 2, 3$) are the three mass eigenvalues. The neutrino description involves a total of nine parameters: three mixing angle, three potential phases, and three mass eigenvalues.

Neutrino oscillations are sensitive to the mixing angles (θ_{ij}) and the Dirac phase (δ), and the absolute differences between the squared mass eigenvalues $\left(\left|\Delta m^2_{ij}\right| = \left|m^2_i - m^2_j\right|\right)$. Their experimental studies allowed the measurement of these values, except for the Dirac phase, whose effect is reduced by the low value of $\sin\theta_{13}$.

The constraints experimentally established on the different parameters, are listed in Table 1.3. The sign of Δm^2_{21} was measured on solar data: $\Delta m^2_{21} > 0$, but the sign of Δm^2_{31} remains unknown: this leads to two possible scenarios: a normal mass hierarchy ($m_1 < m_2 < m_3$), or an inverse mass hierarchy ($m_3 < m_1 < m_2$). Besides, the scale of the lowest neutrino mass (called m_0) is unknown too. It is only limited by a cosmological constraint on the neutrino masses: $\sum_i m_i \lesssim 0.75\,\mathrm{eV/c^2}$ [5], so $m_0 \lesssim 0.2\,\mathrm{eV/c^2}$. A configuration where $m_0 \sim 0.2\,\mathrm{eV/c^2}$ implies that $\Delta m^2_{21} \ll m^2_0$, $\Delta m^2_{31} \ll m^2_0$, and $m_1 \sim m_2 \sim m_3 \sim m_0$: this configuration is referred to as the degenerate state.

parameter	best fit $\pm 1\sigma$
$\Delta m^2_{21}[10^{-5}\ \mathrm{eV}^2]$	$7.59^{+0.20}_{-0.18}$
$\Delta m^2_{31}[10^{-3}\ \mathrm{eV}^2]$	2.45 ± 0.09 $-(2.34^{+0.10}_{-0.09})$
$\sin^2\theta_{12}$	$0.312^{+0.017}_{-0.015}$
$\sin^2\theta_{23}$	0.51 ± 0.06 0.52 ± 0.06
$\sin^2\theta_{13}$	$0.010^{+0.009}_{-0.006}$ $0.013^{+0.009}_{-0.007}$

Table 1.3: Experimental constraints on the neutrino oscillation parameters: results from [6]. For Δm^2_{31}, $\sin^2\theta_{23}$, and $\sin^2\theta_{13}$ the upper (lower) row corresponds to normal (inverted) neutrino mass hierarchy.

The Majorana phases do not intervene in neutrino oscillations, however other experiments are testing the possible Majorana nature of neutrinos, searching for example neutrino-less double-beta decays ($0\nu - 2\beta$), as illustrated in Fig. 1.5. No conclusive results were obtained yet with these experiments.

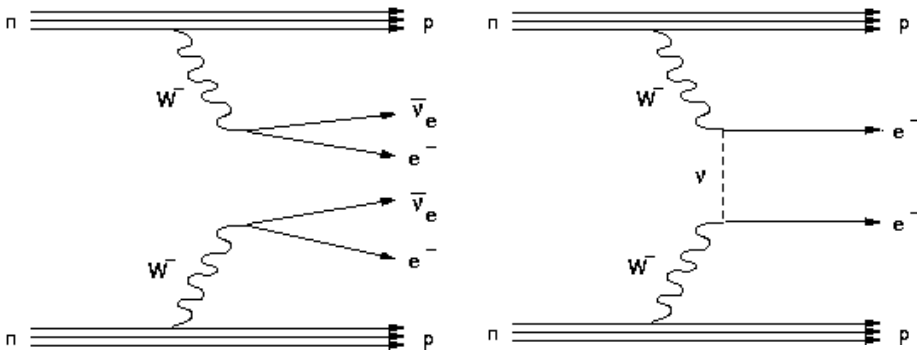

Figure 1.5: (a): the standard and known 'double beta decay', which involves two antineutrinos in the final state: two neutrons from a nucleus decay simultaneously into protons ($n \to p + W$, $W \to e\bar{\nu}_e$). (b): the researched neutrino-less double beta decay: the antineutrino emitted from the first neutron decay, intervenes in the second decay as a neutrino. The observation of this process would imply that neutrinos and antineutrinos be the same particles: they would be Majorana particles.

The Standard Model describes neutrinos as massless particles. It is possible, but not quite satisfactory, to add neutrino mass terms in the Yukawa Lagrangian, similarly to the other fermion mass terms (eq. (1.28) and (1.30)). First of all it requires the addition of right-handed neutrinos, which are neutral under all Standard Model interactions: their in-

troduction for the neutrino mass term is quite strange. The second problem comes from the smallness of neutrino masses ($\lesssim 1\,\mathrm{eV/c^2}$) in comparison with other fermions ($\gtrsim 0.5\,\mathrm{MeV/c^2}$), which the Standard Model fails to explain. Finally, neutrino oscillations violate the conservation law of the lepton number: such interactions are not allowed a priori in the Standard Model.

1.2.2.3 Dark Matter

The concept of dark matter is based on astrophysical observations. The mass of a cluster of galaxies can be measured by two different methods: either using general relativity and measuring the motions of the different galaxies, or knowing the number of galaxies and measuring the total brightness of the cluster. However these measurements do not provide the same estimation on several clusters of galaxy, and on the global universe: this is known as the "missing mass problem".

If one considers that gravity is correctly described, then some invisible matter, called dark matter, must be the reason for these discrepancies. This matter is probably cold; besides, since it is missed by optical detectors, it must be electrically and color neutral. Finally, it must account for a high mass discrepancy ($\sim 23\%$ of the mass-energy density of the observable universe).

The only Standard Model particles of matter with neutral electric and color charges are neutrinos; though they are massive particles, their small mass is not likely to account for these discrepancies. Hence the question of the nature of dark matter is not answered by the Standard Model.

1.2.2.4 Baryon Asymmetry

Baryons are colored states made by the coupling of three quarks, e.g. protons (uud). Antibaryons are made by the coupling of three antiquarks, e.g. antiprotons ($\bar{u}\bar{u}\bar{d}$). The baryon asymmetry is the observed unbalance between the amount of baryons and the amount of antibaryons measured in the universe.

The Big Bang is assumed to have produced equal amounts of matter and antimatter, and the Standard Model predicts mainly interactions preserving this equilibrium. The only exception to this rule is the existence of CP-violating weak interactions that reflect in the

CP-violating phase δ_{13} in the CKM matrix (cf eq. (1.34)). However these interactions are not sufficient to explain the observed unbalance.

Finally, the Standard Model symmetries allow for a CP-violating term in the QCD Lagrangian, but measurements showed this term to be null. The reason why the strong interaction would not violate the CP symmetry while the weak interaction does, is not understood either.

1.3 Looking for the Electroweak Symmetry Breaking at the LHC

A direct question arising from the description of the Standard Model and its limitations, is the one of the existence of a Higgs boson, and whether it has the properties predicted by the Standard Model. Besides, many extensions of the Standard Model predict the existence of one or several Higgs bosons [7] [8]. The research of Higgs bosons is a main goal of the Large Hadron Collider.

1.3.1 Phenomenology of the Standard Model Higgs Boson at LHC

The Higgs boson mass is the only remaining unknown parameter of the electroweak symmetry breaking. In particular, the couplings of the Higgs boson to fermions and bosons are fixed by the theory. As a consequence, the Higgs boson production cross section and its preferred decays depend only on the kinematical constraints set by its mass.

1.3.1.1 Higgs Boson Couplings

The coupling of the Higgs field to elementary particles is the mechanism that provides them a mass in the Standard Model. As a consequence, the Higgs boson only couples to massive particles, with a coupling that is proportional to their masses.

The couplings of the Higgs boson to fermions ($h\bar{f}f$) are proportional to their masses; as a consequence, the couplings to heavy quarks (in particular the top quark) are significantly favored:

$$g_{Hff} = ig_2 \frac{m_f}{2M_W} \ . \tag{1.49}$$

Besides, couplings to weak gauge bosons (hVV) are also proportional to the boson masses:

$$g_{HZZ} = ig_2 \frac{m_Z}{\cos\theta_W} \; ; \; g_{HWW} = ig_2 \, m_W \; . \tag{1.50}$$

Consequently, the Higgs boson couples most likely to the heaviest particles kinematically available.

1.3.1.2 Higgs Boson Production at LHC

The CERN Large Hadron Collider accelerates protons up to an energy of several teraelectronVolts (TeV), and collides them. The nominal center-of-mass energy of the collisions is 14 TeV, however for the first years of data taking, i.e. 2010-2012, collisions are performed with a center-of-mass energy of 7 TeV. Since protons are composite particles, the interactions involved during their collisions, are interactions of their partons.

A high energy proton is made of three valence quarks, interacting through gluons; by effect of these interactions, the valence quarks are surrounded by a sea of quarks and gluons. Hence LHC interactions occur either by quark fusion, or by gluon fusion.

Since the Higgs boson does not couple to gluons, and can not be created directly by a general $q\bar{q}'$ interaction, its production appears mainly through 1-loop vertices. The main production channels are presented in Fig. 1.6; the predominant one is the gluon fusion, that occurs via a quark loop (the bottom left Feynman diagram in Fig. 1.6). The production cross sections are presented in Fig. 1.7, as a function of the Higgs boson mass: they decrease with the Higgs boson mass.

1.3.1.3 Higgs Boson Decays

The comparison of the couplings (1.49) and (1.50) shows that the Higgs boson naturally decays into the highest mass final state kinematically possible. Thus, its decay spectrum depends highly on its mass, as shown in Fig. 1.8.

Low mass Higgs boson: decays into fermions

In the mass range $m_h < 130\,\mathrm{GeV/c^2}$, the decays into gauge bosons are not allowed kinematically. So the Higgs boson will preferentially decay into fermion-antifermion pairs. The decay into a $t\bar{t}$ pair is not allowed kinematically at such masses, and among the other possible final states, the pairs of highest mass are favored.

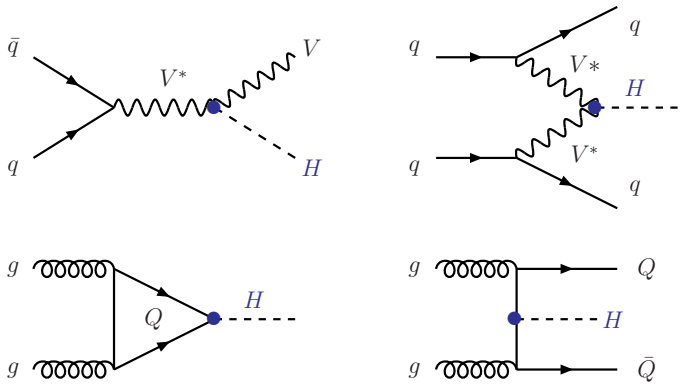

Figure 1.6: Feynman diagrams of the dominant Standard Model Higgs boson production mechanisms in hadronic collisions: Higgsstrahlung (top left), vector boson fusion (top right), gluon fusion (bottom left), $t\bar{t}$ fusion (bottom right).

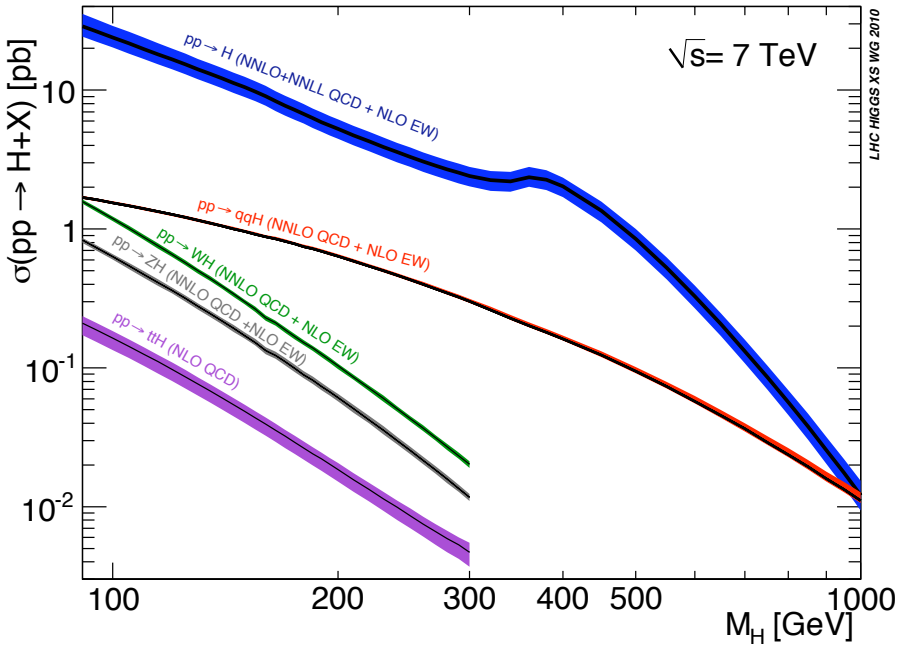

Figure 1.7: Cross section of the Higgs boson production as a function of its mass, for LHC (proton-proton) collisions with a center-of-mass energy of $\sqrt{s} = 7$ TeV. The contributions of the main production channels are presented: Higgsstrahlung (green and black), vector boson fusion (red), gluon fusion (blue), $t\bar{t}$ fusion (purple). The gluon fusion process is largely predominant.

Loop-induced decays into $\gamma\gamma$, $Z\gamma$, gg are also possible, involving loops of off-shell weak bosons, or fermions. The variety of quark loops and the importance of the strong interaction favor the $H \to gg$.

For experimental studies, the $b\bar{b}$ signatures are very difficult to differentiate from the

overwhelming multijet background produced in proton-proton collisions. The $\tau\tau$ and $\gamma\gamma$ signatures are preferred, though their low branching ratios. The particular topology of a Higgs production by vector boson fusion, and decay into τ leptons is an interesting signature. Besides, the $H \to \gamma\gamma$ decay provides the possibility to reconstruct precisely the mass resonance.

High mass Higgs boson: decays into gauge bosons

In the mass range $m_h > 160\,\mathrm{GeV/c^2}$, the decays into gauge bosons take the advantage: $H \to W^+W^-$ and $H \to ZZ$, with a ratio 2:1. In the mass range $130 - 160\,\mathrm{GeV/c^2}$, the decays $H \to WW^*$ and $H \to ZZ^*$ are already predominant (cf Fig. 1.8). For masses higher than $350\,\mathrm{GeV/c^2}$, the $H \to t\bar{t}$ decay appears, however it remains less important than the two other ones.

For experimental studies, the gauge boson leptonic decays present a clean signature, e.g. $H \to W^+W^- \to 2\ell\,2\nu$, $H \to ZZ \to 4\ell$ ($\ell = e, \mu$). However the corresponding branching ratios are very low[6]. As a consequence, the other signatures are also studied.

One particularly clean channel is put forward in this thesis: $H \to ZZ \to 4\ell$ ($\ell = e, \mu$). It provides a very clean signature of four leptons, from which the Higgs boson mass resonance is reconstructed. However it requires a very efficient reconstruction and identification of leptons, since inefficiencies count at power four.

Many theories beyond the Standard Model also provide multi-lepton signatures. It is quite tempting to look for a Standard Model Higgs boson, while keeping an eye open for new models. Two of them are presented in the next paragraphs.

1.3.2 Supersymmetry

The Standard Model considers one symmetry among elementary particles: the matter-antimatter symmetry. To each particle, it associates an antiparticle with same parameters but opposite charges. For example, the positron e^+ is the antiparticle associated to the electron e^-: it is also a lepton, with the same mass and an opposite electric charge; like the electron, it is sensitive to the electromagnetic and weak interactions, but not to the strong one.

[6] $BR(W^\pm \to e^\pm\nu_e) = 10.8\%$; $BR(W^\pm \to \mu^\pm\nu_\mu) = 10.6\%$.
$BR(Z \to e^+e^-) = 3.36\%$; $BR(Z \to \mu^+\mu^-) = 3.37\%$.

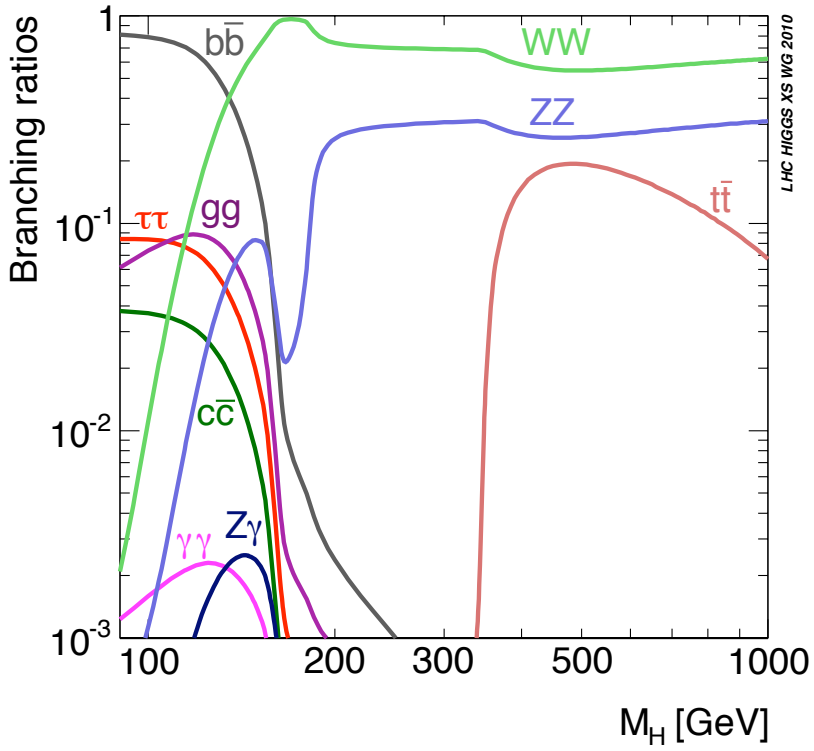

Figure 1.8: Decay branching ratios of the Higgs boson as a function of its mass.

The concept of supersymmetry (SUSY) relies on another such association: to each particle, it associates a *superpartner* with same mass and charges, but different spin. To the Standard Model fermions correspond scalars called sfermions; to gauge bosons correspond fermions called gauginos.

However these superpartners have not been experimentally observed. This is explained by the spontaneous breaking of this supersymmetry, which confers them a significantly higher mass.

The advantages of SUSY

Supersymmetry introduces neutral fermions of rather high mass ($\sim 100\,\mathrm{GeV/c^2}$): the neutralinos ($\tilde{\chi}_i^0$, $i = 1, 2, 3, 4$). The heavier of these four sparticles decay into the lighter ones. In R-parity conserved supersymmetry the lightest neutralino is a stable, electrically and color neutral, massive particle: an excellent candidate for dark matter.

Besides, if the sparticles are in the mass range[7] $100\,\mathrm{GeV/c^2} - 10\,\mathrm{TeV/c^2}$, supersymmetry

[7]This mass range is also particularly interesting for experimentalists, because it can be probed by LHC collisions.

allows the unification of the gauge couplings. The scale of this unification M_{GUT} is slightly higher than in non-supersymmetric models, providing a prediction of the proton lifetime more consistent with the absence of significant observed proton decay.

Finally, supersymmetry provides a good framework to turn on gravity, hence the development of so-called supergravity models.

Higgs bosons in supersymmetric models

A supersymmetric model requires at least two scalar doublets Φ_1 and Φ_2. The electroweak symmetry breaking happens dynamically, thanks to the large top quark Yukawa coupling. In the Minimal Supersymmetric Standard Model (MSSM) which contains exactly two scalar doublets, it results in five heavy bosons: the two neutral CP-even bosons h and H, the neutral CP-odd one A, and the charged bosons $h^{\pm}$. The MSSM predicts that the lightest neutral CP-even Higgs boson be rather light ($m_h < 135\,\mathrm{GeV/c^2}$ at the two-loop level).

These Higgs bosons keep a tendency to couple more to heavier particles; as a consequence, a neutral Higgs boson can decay into a pair of neutralinos ($A/H \rightarrow \chi_i^0 \chi_j^0$) as soon as this decay is kinematically allowed.

A second lightest neutralino χ_2^0 is likely to decay into a lightest neutralino χ_1^0 through a neutral Z boson ($\chi_2^0 \rightarrow \chi_1^0 + Z$), or to a chargino $\chi_1^{\pm}$ through a W boson ($\chi_2^0 \rightarrow \chi_1^{\pm} + W^{\mp} \rightarrow \chi_1^0 + W^{\pm} + W^{\mp}$).

Keeping the leptonic decays of the weak gauge bosons ($W \rightarrow \ell\nu$, $Z \rightarrow \ell^+\ell^-$, $\ell = e, \mu$), and keeping in mind that the lightest neutralinos, similarly to neutrinos, do not interact in the detector, this leaves us with the research of a clean final state made of four leptons and missing transverse energy [9] [10]:

$$A/H \rightarrow \chi_2^0 \chi_2^0 \rightarrow 4\ell + E_T^{miss} \; . \tag{1.51}$$

This final state is very similar to the Standard Model $H \rightarrow ZZ^{(*)} \rightarrow 4\ell$.

1.3.3 Type-II Seesaw Mechanism

Several extensions of the Standard Model have been developed in order to justify the introduction of neutrino masses.

We recall that neutrinos are fermions and can have the same kind of mass terms as other fermions (eq. (1.28) and (1.30)) These are called Dirac mass terms, and mix left-handed and

right-handed eigenstates: they require the existence of right-handed neutrinos with the same masses as the observed left-handed neutrinos.

Besides, neutrinos have no electromagnetic charge and no color charge: so they could also be described as Majorana particles, i.e. particles which are their own antiparticles. This would imply a non-conservation of the lepton number ($\nu_i \rightarrow \bar{\nu}_i$), however observed neutrino oscillations ($\nu_i \rightarrow \nu_j$) already indicate some non-conservations in the lepton numbers. The interesting fact about Majorana mass terms is that they do not mix left-handed and right-handed components of a particle. As a consequence, a description of Majorana massive neutrinos does not require the addition of right-handed neutrinos in the model.

1.3.3.1 Introducing Type-II Seesaw Mechanism

The principle of the Seesaw mechanism is to introduce a correspondence between some high-scale phenomenon, and the low-scale observed neutrino masses. For example, Type-I Seesaw introduces right-handed neutrinos with a Majorana mass of the order of the grand unification scale. The addition of Dirac mass terms that mix right-handed and left-handed neutrinos, confers a very small mass to left-handed neutrinos. The higher the right-handed neutrino mass, the lower the left-handed neutrino mass, hence the name of 'seesaw' mechanism.

Similarly, Type-II Seesaw introduces some new physics at a high scale: in this case, it is an extension of the scalar sector. To the Standard Model $SU(2)_L$ Higgs doublet $\Phi = \begin{pmatrix} \phi^+ \\ \phi^0 \end{pmatrix}$ of hypercharge $Y_\Phi = 1$, it adds a $SU(2)_L$ Higgs triplet[8] Δ of hypercharge $Y_\Delta = 2$:

$$\Delta = \begin{pmatrix} \Delta^+/\sqrt{2} & \Delta^{++} \\ \Delta^0 & -\Delta^+/\sqrt{2} \end{pmatrix} \tag{1.52}$$

Under a gauge transformation $\mathcal{U}(x)$, these fields transform as $\Phi \rightarrow \mathcal{U}(x)\Phi$ and $\Delta \rightarrow \mathcal{U}(x)\Delta\mathcal{U}(x)^\dagger$. The general Lagrangian writes, similarly to eq. (1.38):

$$\mathscr{L}_{Seesaw} = \mathscr{L}_f + \mathscr{L}_Y + \mathscr{L}_g + \mathscr{L}_{\Phi,\Delta} \ , \tag{1.53}$$

where $\mathscr{L}_f$ and $\mathscr{L}_g$ are the same ones as for the Standard Model. The term corresponding to the propagation of the Higgs fields writes:

$$\mathscr{L}_{\Phi,\Delta} = (D_\mu\Phi)^\dagger(D_\mu\Phi) + Tr(D_\mu\Delta)^\dagger(D_\mu\Delta) - V(\Phi,\Delta) \ , \tag{1.54}$$

[8] Several extensions of the Standard Model suggest the addition of a scalar triplet: Little Higgs models [11] and left-right supersymmetric models [12] for example.

where the covariant derivatives write:

$$D_\mu \Phi = \partial_\mu \Phi - i g_1 \frac{Y_\Phi}{2} B_\mu \Phi - i g_2 \frac{\tau_a}{2} W_\mu^a \Phi \ , \tag{1.55}$$

$$D_\mu \Delta = \partial_\mu \Delta - i g_1 \frac{Y_\Delta}{2} B_\mu \Delta - i g_2 \left[\frac{\tau_a}{2} W_\mu^a, \Delta \right] \ , \tag{1.56}$$

and the scalar potential writes:

$$\begin{aligned} V(\Phi, \Delta) &= -\mu^2 \Phi^\dagger \Phi + \lambda \left(\Phi^\dagger \Phi \right)^2 + \mu_\Delta^2 Tr(\Delta^\dagger \Delta) + \left[\alpha (\Phi^T i\sigma^2 \Delta^\dagger \Phi) + h.c. \right] \\ &\quad + \lambda_1 \Phi^\dagger \Phi Tr(\Delta^\dagger \Delta) + \lambda_2 (Tr \Delta^\dagger \Delta)^2 + \lambda_3 Tr(\Delta^\dagger \Delta)^2 + \lambda_4 \Phi^\dagger \Delta \Delta^\dagger \Phi \ . \end{aligned} \tag{1.57}$$

A priori both scalar fields Φ and Δ can develop a non-zero vacuum expectation value in their neutral components[9]:

$$\langle \Phi \rangle = \frac{1}{\sqrt{2}} \begin{pmatrix} 0 \\ v \end{pmatrix} \ ; \ \langle \Delta \rangle = \frac{1}{\sqrt{2}} \begin{pmatrix} 0 & 0 \\ v_\Delta & 0 \end{pmatrix} \ . \tag{1.58}$$

The minimization of the scalar potential implies non-zero values for both v and v_Δ.

Finally, the Yukawa Lagrangian $\mathscr{L}_Y$ contains, in addition to the complete Standard Model Yukawa Lagrangian, a coupling term between the scalar triplet Δ and the lepton doublets $L_i = \begin{pmatrix} \nu_{iL} \\ \ell_{iL} \end{pmatrix}$: $\mathscr{L}_Y = \mathscr{L}_Y^{SM} + \mathscr{L}_Y^{\Delta,\nu}$, where:

$$\begin{aligned} \mathscr{L}_Y^{\Delta,\nu} &= -Y_\nu L^T C \otimes i\sigma^2 \Delta L + h.c. \\ &= -Y_{ij} \left[\nu_{iL}^T C \nu_{jL} \Delta^0 - \frac{1}{\sqrt{2}} (\nu_{iL}^T C \ell_{jL} + \ell_{iL}^T C \nu_{jL}) \Delta^+ - \ell_{iL}^T C \ell_{jL} \Delta^{++} \right] + h.c. \end{aligned} \tag{1.59}$$

where C is the charge conjugation operator, and the symmetric complex matrix Y_ν is the Yukawa coupling strength ($i, j = e, \mu, \tau$). This extension of the Yukawa Lagrangian introduces the non-conservation of the leptonic number.

Taking into account the triplet vacuum expectation value described in eq. (1.58), this Yukawa Lagrangian gives rise to a neutrino Majorana mass term, $-\frac{1}{2} m_{ij} \, \nu_{iL}^T C \, \nu_{jL}$. The neutrino mass matrix m mentioned in eq. (1.48), is related to the Yukawa couplings:

$$m_{ij} = 2 Y_{ij} \langle \Delta^0 \rangle = \sqrt{2} Y_{ij} v_\Delta \ . \tag{1.60}$$

[9] An electrically charged field does not acquire any vacuum expectation value, because otherwise charge would be spontaneously broken.

1.3.3.2 Constraints on the Scalar Fields

The potential minimization imposes the two following constraints on the parameters [13]:

$$\mu^2 = \lambda v^2 - \sqrt{2}\alpha v_\Delta + \frac{\lambda_1 + \lambda_4}{2} v_\Delta^2 \tag{1.61}$$

$$\mu_\Delta^2 = \frac{2\alpha v^2 - \sqrt{2}(\lambda_1 + \lambda_4) v^2 v_\Delta - 2\sqrt{2}(\lambda_2 + \lambda_3) v_\Delta^3}{2\sqrt{2} v_\Delta} \tag{1.62}$$

Requiring the correct electroweak scale sets a constraint on the two vacuum expectation values: $\sqrt{v^2 + 2v_\Delta^2} = (\sqrt{2} G_F)^{-1/2} \approx 246$ GeV. Besides, the naturalness consideration from neutrino masses implies $v_\Delta \gtrsim 1$ eV.

Moreover, an agreement with the measurement of the constant $\rho \equiv \frac{M_W^2}{M_Z^2 \cos^2 \theta_W}$, implies a limitation on the ratio[10] $\frac{v_\Delta}{v}$: taking the electroweak scale condition into account, this results in:

$$v \approx 246 \text{ GeV} \ , \ v_\Delta \lesssim 1 \text{ GeV} \ . \tag{1.63}$$

Let us consider more closely the scalars involved in this model: the doublet Φ and the triplet Δ. After the electroweak symmetry breaking, seven physical massive Higgs bosons remain: ($H^{\pm\pm}$, $H^\pm$, h^0, H^0, A^0).

The $H^{\pm\pm}$ bosons are entirely composed of the triplet scalars $\Delta^{\pm\pm}$. The remaining eigenstates are mixtures of the doublet and triplet scalars, however the mixing angles are small (their tangent is proportional to the ratio $\frac{v_\Delta}{v}$). Thus, $H^\pm$, H^0 and A^0 are predominantly composed of the triplet scalar, while h^0 is mainly composed of the doublet scalar.

The mass of the $H^{\pm\pm}$ boson (i.e. the mass of the triplet) writes:

$$m_{H^{\pm\pm}}^2 = \frac{\sqrt{2}\alpha v^2 - \lambda_4 v^2 v_\Delta - 2\lambda_3 v_\Delta^3}{2 v_\Delta} \ . \tag{1.64}$$

Knowing that $\frac{v_\Delta}{v} \lesssim 0.03$, the doubly charged Higgs boson mass scale depends mainly on the scale of α. Besides the comparison of eq. (1.64) and (1.60) shows the seesaw concept: when the vacuum expectation value v_Δ gets small, the mass of the scalar triplet increases and the neutrino masses decrease.

The differences between the masses of $H^{\pm\pm}$, $H^\pm$, H^0 and A^0 appear through the quartic couplings in the Higgs potential. If one assumes $\lambda_i v_\Delta \ll \alpha$ ($i = 1, 2, 3, 4$), then these masses

[10] The Standard Model predicts a tree-level value $\rho = 1$, in perfect agreement with experiments. After the introduction of $v_\Delta \neq 0$, defining $x = \frac{v_\Delta}{v}$, the constant writes: $\rho = \frac{1+2x^2}{1+4x^2}$. This is still in agreement with experimental results, given that $x \lesssim 0.03$.

are degenerate, and h^0 takes the same mass as the Standard Model Higgs boson:

$$m^2_{H^{\pm\pm}} \approx m^2_{H^{\pm}} \approx m^2_{H^0} \approx m^2_{A^0} \approx \frac{\alpha}{\sqrt{2}}\frac{v^2}{v_\Delta} \; ; \; m^2_{h^0} \approx 2\lambda v^2 \; . \tag{1.65}$$

The most striking signature of this model would be the observation of the doubly charged bosons[11] $H^{\pm\pm}$. Besides, the couplings of H^{++} to charged leptons are proportional to the neutrino mass matrix (eq. (1.59) and (1.60)). Hence the comparison of its leptonic branching ratios provides a measurement of the parameters of the neutrino mass matrix that can not be measured with neutrino oscillations.

Direct searches for doubly charged Higgs bosons in leptonic final states were carried at LEP [14, 15, 16] and mass limits in the range $95.5 - 100.2\,\mathrm{GeV/c^2}$ have been obtained, depending on the decay modes. Doubly charged Higgses have also been searched for at the Fermilab Tevatron, and mass limits in the range $m_{H^{\pm\pm}} > 110 - 150\,\mathrm{GeV/c^2}$ have been set [17, 18, 19, 20].

The mass range $100 - 1000\,\mathrm{GeV/c^2}$ can be explored at LHC: this corresponds to the conditions $\alpha \sim v_\Delta$ and $\lambda_i \ll 1$ in the case of degenerate masses.

1.3.3.3 Phenomenology Involving Doubly Charged Bosons for LHC Collisions

A total of ten parameters were introduced in the description of this model: the eight parameters of the potential (1.57): μ, λ, μ_Δ, α and λ_i ($i = 1, 2, 3, 4$), and the two vacuum expectation values v and v_Δ. After the minimization of the potential (eq. (1.61) and (1.62)) and the electroweak scale constraint, seven degrees of freedom remain. Even if we neglige the quartic couplings λ_i (which is done in this paragraph for simplicity), three free parameters remain: λ sets the doublet mass, while v_Δ and α set the triplet mass and v_Δ also intervenes in the Yukawa couplings.

Besides, the Yukawa coupling matrix Y_ν depends on the neutrino mass matrix (1.60). Some parameters of this matrix were measured with neutrino oscillation studies, however the remaining uncertainties on the neutrino mass hierarchy, the mass scale m_0, and the three phases, correspond to so many uncertainties on the Yukawa couplings.

These degrees of freedom intervene in the couplings, and make phenomenology predictions difficult: in particular, the predictions depend on the triplet vacuum expectation value

[11] Singly charged or neutral bosons appear in many models, e.g. from scalar doublets in supersymmetric models. Doubly charged scalars are more unusual.

v_Δ, and on the parameters of the neutrino mass matrix.

Couplings

The covariant derivatives imply couplings of the Higgs triplet Δ with the massive gauge bosons. As a consequence, the coupling $g_{H^{++}H^{--}Z}$ is constant. If the coupling of the scalar triplet and the scalar doublet is negligible, then $g_{H^{++}H^{-}W^{-}}$ is also constant.

In the covariant derivative appear also couplings proportional to the triplet vacuum expectation value: $g_{H^{++}W^{-}W^{-}}$, and $g_{H^{+}W^{-}Z}$ in the same conditions as previously.

Scalar self-couplings appear in the potential: they are not detailed here because they are not useful for our studies.

Finally, the Yukawa Lagrangian implies Yukawa couplings between the Higgs triplet and the leptons: $g_{H^{++}\ell_i^-\ell_j^-}$, $g_{H^{+}\ell_i^-\nu_j}$. These are proportional to the neutrino mass matrix.

Production

The two constant couplings mentioned above define the two main production processes of doubly charged Higgs bosons in the context of proton-proton collisions. The pair production cross section (1.66) depends only on one unknown parameter, $m_{H^{\pm\pm}}$:

$$q\bar{q} \rightarrow Z^*, \gamma^* \rightarrow H^{++}H^{--} \ . \tag{1.66}$$

The associate production cross section (1.67) depends on the masses of $H^{\pm\pm}$ and $H^{\pm}$, which are assumed to be equal in this paragraph, because the quartic couplings are neglected:

$$q\bar{q'} \rightarrow W^{\pm *} \rightarrow H^{\pm\pm}H^{\mp} \ . \tag{1.67}$$

The two cross sections are comparable, and the latter is generally slightly higher. Since the LHC provides proton-proton collisions, the cross section of the W^+ boson is significantly higher than the one of the W^- boson: as a consequence, the cross section of $H^{++}H^{-}$ is higher than the one of $H^{--}H^{+}$.

The inclusive cross section for (1.66) and (1.67), is shown in Fig. 1.9, for several LHC collision center-of-mass energies, and for Tevatron collisions.

Branching ratios

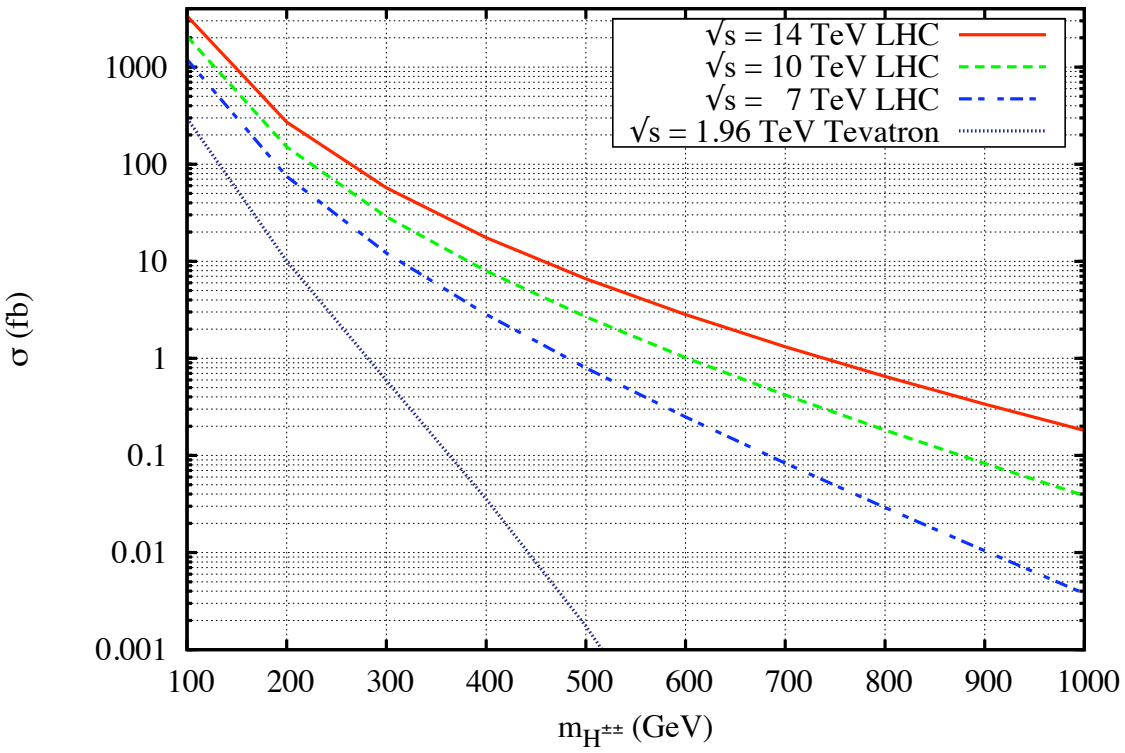

Figure 1.9: Cross section of inclusive doubly charged Higgs boson production as a function of $M_{H^{\pm\pm}}$: eq. (1.66) and (1.67). The K-factor of the processes is taken to be 1.25 for LHC and 1.3 for Tevatron [21].

Given the couplings listed above, several decay channels are to be considered[12] for the $H^{\pm\pm}$ boson, e.g. $H^{\pm\pm} \to W^{\pm}W^{\pm}$ and $H^{\pm\pm} \to \ell_i^{\pm}\ell_j^{\pm}$. Similarly, the singly charged boson $H^{\pm}$ can decay into gauge bosons $H^{\pm} \to W^{\pm}Z$ or leptonically $H^{\pm} \to \ell_i^{\pm}\nu_j$. If the mixing with the scalar doublet is significant, it may also decay into quarks[13] $H^{+} \to t\bar{b}$.

Three general situations are distinguished [22], depending on the triplet vacuum expectation value v_Δ, as shown in Fig. 1.10 and 1.11:

- $1\,\text{eV} \lesssim v_\Delta < 10^{-4}\,\text{GeV}$: in this case the bosonic decays are cancelled by the low value of v_Δ. The decay channels $H^{\pm\pm} \to \ell_i^{\pm}\ell_j^{\pm}$ and $H^{\pm} \to \ell_i^{\pm}\nu_j$ can be considered as predominant.

- $v_\Delta \approx 10^{-4}\,\text{GeV}$: all the decay channels listed above are comparable.

- $10^{-4}\,\text{GeV} < v_\Delta \lesssim 1\,\text{GeV}$: in that case the leptonic decays are suppressed and the

[12] Decays involving other scalar bosons were studied in the case of non-degenerate masses, and found to be negligible [22].

[13] This involves the coupling to quarks of the charged component of the scalar doublet, ϕ^{+}.

mixing of the scalar triplet and doublet is not negligible anymore.

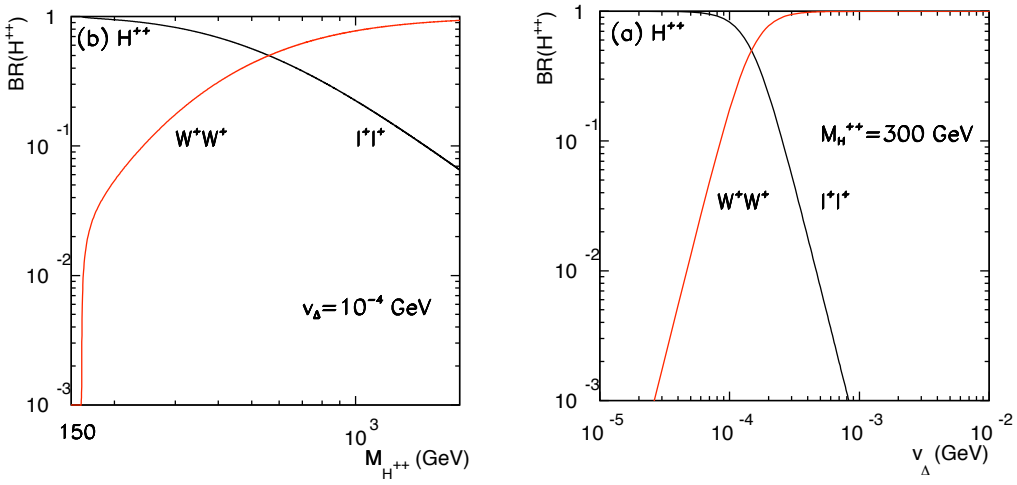

(a) (b)

Figure 1.10: Decays of $H^{\pm\pm}$ assuming $m_{H^{\pm\pm}} = m_{H^{\pm}}$ [22]. (a): as a function of its mass, for $v_\Delta = 10^{-4}$ GeV. (b): as a function of v_Δ, for $m_{H^{\pm\pm}} = 300\,\mathrm{GeV/c^2}$.

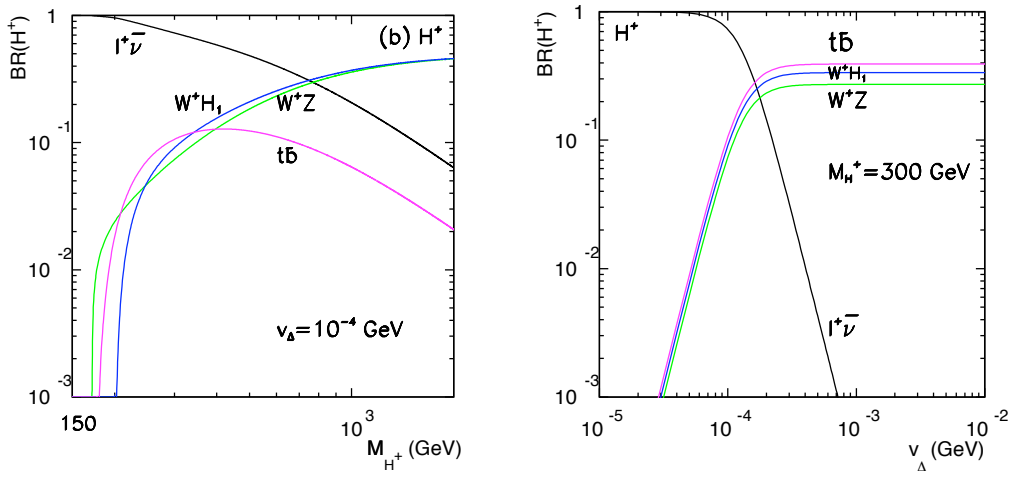

(a) (b)

Figure 1.11: Decays of $H^{\pm}$ [22]. (a): as a function of its mass, for $v_\Delta = 10^{-4}$ GeV. (b): as a function of v_Δ, for $m_{H^{\pm}} = 300\,\mathrm{GeV/c^2}$.

Study of the leptonic decays

Considering the condition 1 eV $\lesssim v_\Delta < 10^{-4}$ GeV, the $H^{\pm\pm}$ and $H^{\pm}$ bosons decay leptoni-

cally:

$$H^{\pm\pm} \to \ell_i^{\pm} \ell_j^{\pm} \ . \tag{1.68}$$

$$H^{\pm} \to \ell_i^{\pm} \nu_j \ . \tag{1.69}$$

The two production processes (1.66) and (1.67), followed by the leptonic decays (1.68) and (1.69), provide multi-lepton final states: respectively $\ell_i^+ \ell_j^+ \ell_m^- \ell_n^-$ and $\ell_i^{\pm} \ell_j^{\pm} \ell_m^{\mp} \nu_n$, where i, j, m, n run over the three lepton flavors (e, μ, τ).

This phenomenology is however not simple: the doubly charged Higgs boson possesses six different decay channels, since all lepton pairs are allowed a priori; the singly charged Higgs boson possesses three phenomenologically different decay channels, since all neutrinos present the same signature in LHC detectors.

The branching ratios for these different decays are determined by the Yukawa coupling matrix, and so by the neutrino mass matrix. Several parameters of this matrix (cf eq. (1.48)) have not been measured yet: in particular, the sign of $m_3^2 - m_1^2$ (i.e. the neutrino mass hierarchy), the smallest of the neutrino masses (m_0), the Dirac (CP-violating) phase δ, and the Majorana phases α_1 and α_2, described in (1.47).

Varying these parameters can change completely the leptonic branching ratios, as shown in Table 1.4. Hence no particular leptonic decay can be assumed to be predominant, or negligible, unless a hypothesis is made on these parameters.

Spectrum	Relations
Normal Hierarchy $m_1 < m_2 < m_3$	$BR(H^{++} \to \tau^+\tau^+), BR(H^{++} \to \mu^+\mu^+) \gg BR(H^{++} \to e^+e^+)$ $BR(H^{++} \to \mu^+\tau^+) \gg BR(H^{++} \to e^+\mu^+), BR(H^{++} \to e^+\tau^+)$ $BR(H^+ \to \tau^+\bar{\nu}), BR(H^+ \to \mu^+\bar{\nu}) \gg BR(H^+ \to e^+\bar{\nu})$
Inverse Hierarchy $m_3 < m_1 < m_2$	$BR(H^{++} \to e^+e^+) > BR(H^{++} \to \mu^+\mu^+), BR(H^{++} \to \tau^+\tau^+)$ $BR(H^{++} \to \mu^+\tau^+) \gg BR(H^{++} \to e^+\mu^+), BR(H^{++} \to e^+\tau^+)$ $BR(H^+ \to e^+\bar{\nu}) > BR(H^+ \to \mu^+\bar{\nu}), BR(H^+ \to \tau^+\bar{\nu})$
Quasi-Degenerate $m_1 \sim m_2 \sim m_3 > \sqrt{\lvert\Delta m_{31}^2\rvert}$	$BR(H^{++} \to e^+e^+) \sim BR(H^{++} \to \mu^+\mu^+) \sim BR(H^{++} \to \tau^+\tau^+) \approx 30\,\%$ $BR(H^+ \to e^+\bar{\nu}) \sim BR(H^+ \to \mu^+\bar{\nu}) \sim BR(H^+ \to \tau^+\bar{\nu}) \approx 30\,\%$

Table 1.4: Relations among the branching fractions of the lepton number violating Higgs decays for the neutrino mass patters of 'normal hierarchy', 'inverse hierarchy', and 'quasi-degenerate', with no Majorana phases $\alpha_1 = \alpha_2 = 0$ [22]. In the case of a quasi-degenerate state, the neutrino mass matrix is roughly proportional to the identity, and so is the Yukawa coupling matrix, which explains the values of the branching ratios.

For experimental considerations, the final states including only electrons and muons are much cleaner than the other ones and allow the reconstruction of a resonance. These signatures (4ℓ or $3\ell + E_T^{miss}$) are quite similar to the ones of the $H \to ZZ^{(*)} \to 4\ell$ analysis. In particular they possess the same main backgrounds. The experience of the $H \to ZZ^{(*)} \to 4\ell$ studies in leptons and in background removal is very useful for these searches too.

Chapter 2

The LHC Collider and the CMS Experiment

All perception of truth is the detection of an analogy.

Henry David Thoreau

Contents

2.1 The Large Hadron Collider

2.1.1 CERN and the LHC Project

Since its creation in 1954, the European Organization for Nuclear Research (CERN) has housed numerous particle accelerators and its experiments played a major role in the construction of the Standard Model of Particle Physics. The Large Electron-Positron Collider (LEP), built inside a 26.7 km circular tunnel located approximately 100 m in the underground, made also a giant step in the hunt for the Higgs boson, that is still ongoing today.

The Large Hadron Collider (LHC) [23, 24] was installed in the tunnel that had been constructed for the LEP machine, and took over in this search. It inherited the Proton Synchrotron (PS) and the Super Proton Synchrotron (SPS) accelerator systems (cf Fig. 2.1). Four interaction regions were equipped, and host four main detectors: ATLAS, CMS, ALICE and LHCb.

The two generalist experiments, CMS and ATLAS, study Standard Model physics processes (electroweak processes, physics of the top and bottom quarks, ...). Their main goal is the search for the Higgs boson, and physics beyond the Standard Model.

The LHC is designed for two kinds of collisions: collisions of protons, and collisions of Heavy ions. This section focuses on the case of proton collisions.

2.1.2 Performance Goals

The LHC was designed to probe the scalar sector, and new physics in case of the absence of a Higgs boson. The unitarity constraint, mentioned in paragraph 1.2.1, sets a limit on the Higgs boson mass: $m_H < 780\,\mathrm{GeV/c^2}$. Besides, when applied to the tree-level amplitude for $W_L^+W_L^- \to Z_LZ_L$ and in the absence of fundamental Higgs, it imposes that new physics appears at a scale $\Lambda \lesssim 1.2$ TeV. Hence the LHC collisions should be able to produce Higgs bosons of masses lower than the TeV; besides they should provide interactions of W_L bosons at a center-of-mass energy of the order of the TeV, in order to probe the unitarity constraint. The second requirement is tighter and requires a proton-proton center-of-mass energy of the order of 14 TeV.

The number of events of a given physics process that occur during one second, is directly related to the cross section[1] of the corresponding process, $\sigma_{process}$, via the luminosity $\mathcal{L}$ of

[1] In nuclear and particle physics, the cross section is used to express the normalized rate or probability of

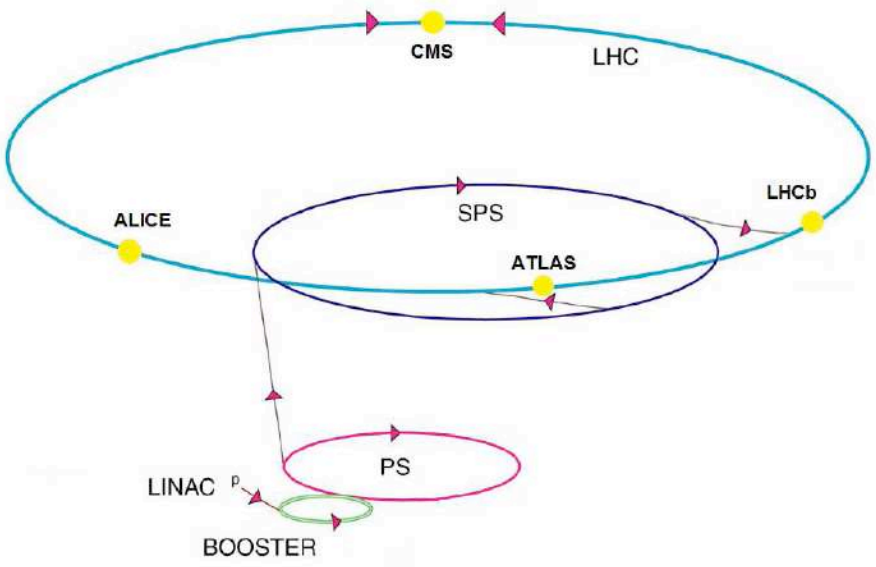

Figure 2.1: The LHC accelerator complex. Proton acceleration starts from a linear accelerator (LINAC) that injects the protons to the Proton Synchrotron (PS), which accelerates them to 25 GeV. In the following stage, the Super Proton Synchrotron (SPS) accelerates the beams to 450 GeV and subsequently injects them into the LHC ring.

the machine[2]:

$$N = \mathcal{L}\,\sigma_{process} \tag{2.1}$$

The relevant events for physics searches, such as Higgs physics and physics beyond the Standard Model, are predicted to have a quite low production cross sections in proton-proton collisions. As an illustration, Fig. 2.2 shows that the cross section for the production of a Higgs boson is several orders of magnitude smaller than the total inelastic cross section. Besides, it increases significantly more than the other ones with the center-of-mass energy of the collisions. Hence, for the expected rate of researched events to be reasonably high, both the collision luminosity and the center-of-mass energy must be as high as possible. For the LHC the choice focused on a very high collision luminosity.

The nominal center-of-mass energy for LHC collisions is $\sqrt{s} = 14$ TeV (7 TeV per beam), and the nominal peak luminosity is $\mathcal{L} = 10^{34}$ cm^{-2}s^{-1} for the CMS and ATLAS experiments. The right axis on Fig. 2.2 shows that for these values[3], a Higgs boson with a mass of

a given interaction between particles. It has the dimension of a surface, and is usually expressed in barns (b): $1\text{b} = 10^{-28}$ m^2.

[2]The luminosity is the number of particles per unit area per unit time times the opacity of the target, usually expressed in cm^{-2}s^{-1}.

[3]At such a high luminosity, approximately one billion inelastic collisions are created every second. More generally, the low proportion of physics events in comparison to the overall number of inelastic interactions suggests the necessity, for experiments, of an efficient triggering system, to select the events to be recorded.

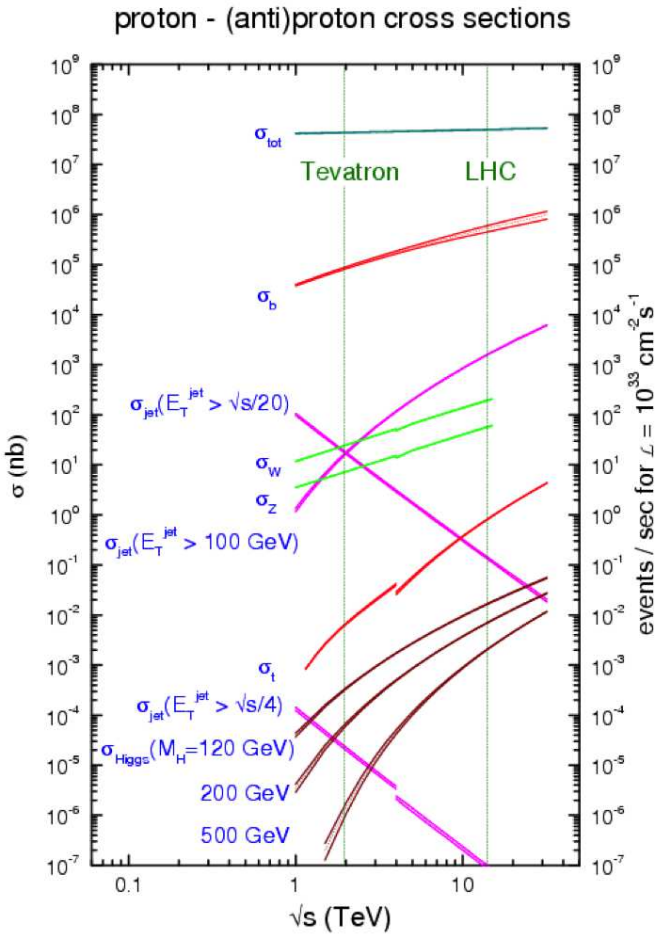

Figure 2.2: Expected cross section as a function of energy in the centre of mass system for proton-proton collisions. The cross sections are indicated in the left vertical axis. The right vertical axis shows the number of events expected per second for a luminosity of $\mathcal{L} = 10^{33}\ \mathrm{cm}^{-2}\mathrm{s}^{-1}$.

$500\,\mathrm{GeV/c}^2$ would be produced approximately every 100 s. To estimate the number of measured events, one must then take into account the Higgs branching ratios and the experiment reconstruction and (online and offline) selection efficiencies.

2.1.3 Nominal Center-of-mass Energy and Magnet Systems

The LHC being a proton accelerator with a constrained circumference, the maximal energy per beam is related to the strength of the dipole field that maintains the beams in orbit.

The nominal LHC beam energy of 7 TeV is possible thanks to a global magnet system at the edge of the technology. The system uses a total of about 9600 magnets.

The 1232 dipole magnets use niobium-titanium (NbTi) cables. They are brought to a

temperature of 1.9 K, by pumping superfluid helium into the magnets. A total of 120 t of superfluid helium is used.

At that temperature[4], the dipoles are in a superconducting state, and when carrying a current of 11850 A they provide a field of 8.33 T. Such a magnetic field is necessary to bend the 7 TeV beams around the 27-km ring of the LHC.

Among the other magnets, quadrupoles play a major role at collision points: they are used to focus the beam, and maximize the probability of collision.

2.1.4 Nominal Luminosity and Beam Parameters

The very high LHC design luminosity implies many constraints on the proton beam parameters. In the general case of two colliding beams, the luminosity $\mathcal{L}$ writes:

$$\mathcal{L} = f_{rev}\, n_b\, \frac{N_1 N_2}{A} \tag{2.2}$$

Where f_{rev} is the revolution frequency, n_b is the number of bunches per beam, N_1 and N_2 are the number of particles in the bunches of each colliding beam, and A is the cross section of the beams.

At LHC, the bunches are filled with an identical number of protons and $N_1 = N_2 = N_b$. The cross section of the beam writes:

$$A = 4\pi\epsilon_n \frac{\beta^*}{\gamma_r} \tag{2.3}$$

Where ϵ_n is the normalized transverse beam emittance[5] (with a design value of 3.75 μm), and β^* is the beta function at collision point[6], which is then corrected by the relativistic gamma factor γ_r.

Finally, the expression in (2.2) has to be corrected by a geometric luminosity reduction factor, F, due to the crossing angle at interaction point.

Hence, the final expression of the luminosity writes:

$$\mathcal{L} = \frac{f_{rev}\, n_b\, N_b^2 \gamma_r}{4\pi\epsilon_n \beta^*}\, F \tag{2.4}$$

Given the beam velocity ($v \sim c \sim 3 \cdot 10^8$ m s^{-1}) and the LHC circumference (26.7 km), the revolution frequency is $f_{rev} = 11$ kHz. Besides, the nominal value of the beta function at

[4]NbTi becomes superconducting below a temperature of 10 K. At a temperature of 4.2 K (which is the temperature in the Tevatron collider magnets), the dipoles would produce a magnetic field smaller than 7 T.

[5]The beam emittance of a particle accelerator is the extent occupied by the particles of the beam in position and momentum phase space.

[6]It measures the beam focalization.

impact point is $\beta^* = 0.55$ m. So the nominal luminosity is reached with $n_b = 2,808$ bunches per beam, and $N_b = 1.15 \cdot 10^{11}$ protons per bunch.

2.1.5 Lattice Layout

Such a high beam intensity could not be obtained with antiproton beams[7]. This is why a 'simple' particle-antiparticle accelerator collider configuration[8] could not be used at LHC.

The LHC is therefore designed with two rings: two separate magnet fields and vacuum chambers, in a twin-bore magnet design. The only common sections are located at the insertion regions, equipped with the experimental detectors. The configuration is shown in Fig. 2.3.

A summary of the machine parameters [25] is given in Table 2.1. The numbers indicated correspond to the nominal values. In addition to the previously mentioned parameters, the luminosity lifetime is an important parameter at LHC and colliders in general. The luminosity tends to decay during a physics run, because of the degradation of intensities and emittances of the circulating and colliding beams.

Circonference	26.659 km
Center-of-mass energy ($\sqrt{s}$)	14 TeV
Nominal Luminosity ($\mathcal{L}$)	10^{34} cm^{-2}s^{-1}
Luminosity lifetime	15 hr
Time between two bunch crossings	24.95 ns
Distance between two bunches	7.48 m
Longitudinal max. size of a bunch	7.55 cm
Number of bunches (n_b)	2808
Number of protons per bunch (N_b)	1.15×10^{11}
beta function at impact point (β^*)	0.55 m
Transverse RMS beam size at impact point (σ^*)	16.7 μm
Dipole field at 7 TeV (B)	8.33 T
Dipole temperature (T)	1.9 K

Table 2.1: The LHC nominal parameter values, for proton-proton collisions, relevant for the detectors.

[7] In comparison, the highest luminosity achieved at the Tevatron proton-antiproton collider after the latest upgrades, is $3 \cdot 10^{32}$ cm^{-2}s^{-1}: this corresponds to the highest antiproton density ever produced, with the most performant technology. The LHC design luminosity must be two orders of magnitude higher.

[8] In such a configuration, both beams can share the same phase space, so a single ring can be used.

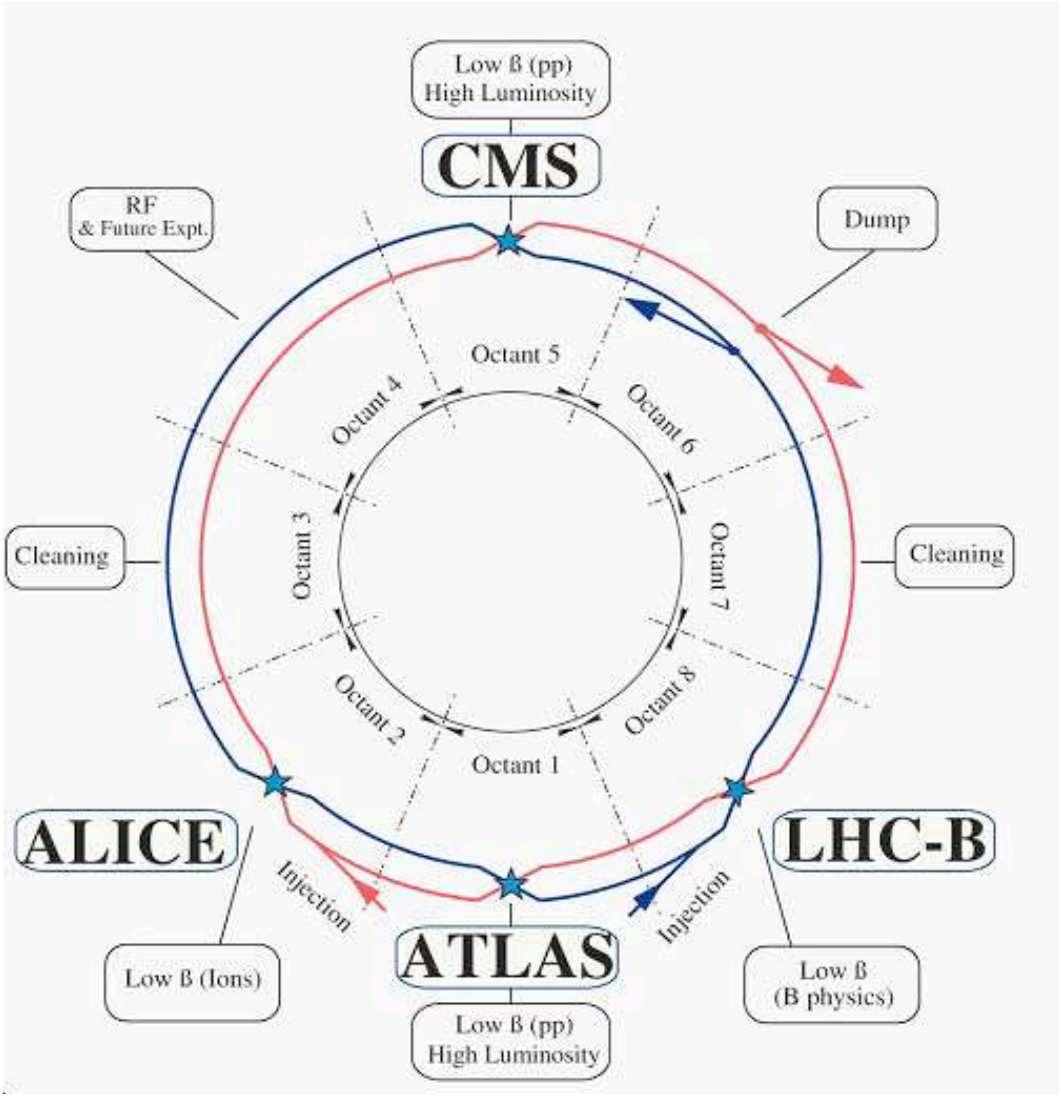

Figure 2.3: Schematic layout of the LHC (Beam1- clockwise, Beam2- anticlockwise).

2.1.6 LHC Collision Detectors

The design parameters necessary to reach the high luminosity makes the LHC a unique machine and imposes important constraints for the detectors.

Under nominal conditions, the LHC will produce 10^9 inelastic collision events per second: a bunch crossing rate of 40 MHz (i.e. a bunch crossing spacing of 25 ns), with ~ 20 collision events expected per bunch crossing.

2.1.6.1 Pile-up Events

Because of the large number of protons per bunch, a significant number of inelastic collisions are expected to occur at each crossing, corresponding to an average of 1000 particles per bunch crossing. To distinguish such events from one another, a high granularity is mandatory, which implies a large number of detector channels.

Besides, the detectors must provide a fast response (mainly concentrated in one bunch spacing, i.e. 25 ns), with a good time resolution (few ns), in order to distinguish the events from two consecutive bunch crossings. This requires a precise synchronization of all detector channels. The limit where two consecutive signals start to overlap is called out-of-time pile-up, and affects the shape of the signal, which is typically a few bunch crossings. This case must also be taken into account.

2.1.6.2 Collision Rate

Under nominal conditions, the LHC will produce 10^9 inelastic collision events per second. Though the very important computing and storage facilities, events can only be recorded at a rate of $\sim$ 300 Hz. Hence the necessity of an online selection system that determines in a very small amount of time[9] whether an event is worth being recorded. Not only must this system be fast: it should be very selective to reduce the event rate by seven orders of magnitude. Finally, this selection system must keep a very high efficiency on interesting collision events.

2.1.6.3 High Radiation

The large flux of particles emitted by LHC collisions implies high radiation levels[10]. So the detectors shall not only be precise and selective, they must be highly resistant to radiations. The same condition applies to their front-end electronics. Detectors were designed to operate during ten years of nominal LHC collisions.

[9] Bunch crossings occur every 25 ns in the case of LHC nominal collisions; during the latency of the first step of the event selection, all information of the event must be stored in the electronics; hence this latency should be at most few orders of magnitude higher than the bunch spacing (25 ns): typically 128 BX.

[10] For example, at nominal luminosity, the CMS electromagnetic calorimeter (located $\sim 2-3$ m from the collision point) is submitted to a radiation of $\sim$ 0.2 to 6.5 Gy/h.

2.2 The CMS Detector

2.2.1 Coordinate System

In this section and the following ones, the same system of coordinates will be used when considering the detector: it is illustrated in Fig. 2.4. The detector has a cylindrical shape around the beam axis (z axis).

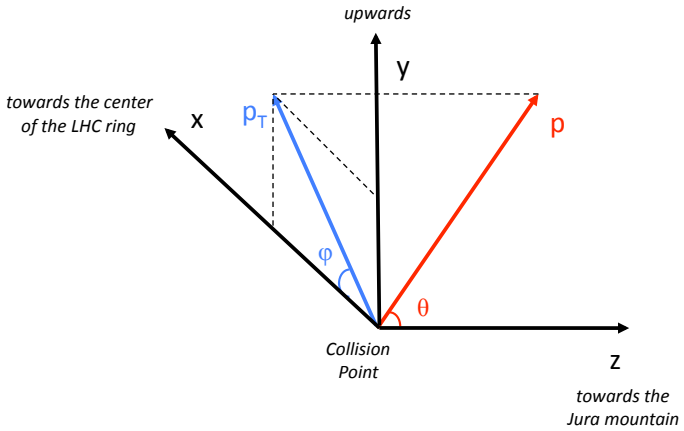

Figure 2.4: The CMS coordinate system.

The origin is centered at the nominal collision point inside the experiment; the x axis points horizontally towards the center of the LHC, and the y axis points vertically upwards, so the z (longitudinal) axis, horizontal and colinear to the beam trajectory, points towards the Jura mountain.

In the transverse (x-y) plane, the azimuthal angle ϕ is measured from the x axis and the radial coordinate is denoted r. The polar angle θ is measured from the z axis. In particular the pseudorapidity[11] η will be used, defined as $\eta = -\ln\tan(\theta/2)$.

The direction of a particle trajectory at production point is described by the coordinates (η, ϕ).

Keeping in mind the cylindrical shape of the detector, the η coordinate makes the difference between two parts of the subdetectors: the 'barrel' corresponds to the central, cylindrical region, and the 'endcaps' are the two discs at the extremities that close the detector along the beam axis.

[11] The pseudorapidity η is an approximation of the rapidity $\rho = \ln(\frac{E+p_z}{E-p_z})$ in the relativistic limit ($\frac{mc^2}{E} \to 0$). These units are interesting in particle physics, because a Lorentz boost along the z axis ($\rho = \rho - \frac{1}{2}\ln(\frac{1+\beta}{1-\beta})$), leaves the variable $\frac{dN}{d\rho}$ unchanged ($\frac{dN}{d\rho}$ is the number of emitted particles by rapidity unit).

An inelastic collision event is the collision of two partons: one from a proton of the first beam, and one from a proton of the second beam. The energy of each parton is an unknown fraction of the proton energy, so the collision energy is not fixed. However the parton momentum, before the collision, is expected to be longitudinal (along the beam axis): the transverse momentum of each parton being negligible, and the total transverse momentum being conserved during an interaction, the transverse momentum of the collision is expected to be negligible too.

As a consequence, the particle trajectories are often described in the transverse plane, in particular their transverse energy writes: $E_T = E \sin\theta = \frac{E}{\cosh\eta}$. For a massless particle, the transverse energy is equal to the transverse momentum: $E_T = p_T$. For electrons and muons, and for the energies considered[12], the masses are negligible and one will assume that $E_T = p_T$.

A particle escaping the detection creates an unbalance in the total transverse energy measurement, also called missing transverse energy. If the detector is hermetic, this missing transverse energy can be interpreted as the transverse energy of the particles that the detector is not intended to measure, such as neutrinos or new physics particles that interact as little as neutrinos with matter (e.g. neutralinos).

2.2.2 The CMS Detector and its Magnet

A multi-purpose detector contains two calorimeters. Electromagnetic particles are stopped and measured in the first one; hadronic particles are measured in both and stopped in the second one. In addition, an inner tracking device measures the trajectories of all charged particles, while an outer device measures the charged particles that crossed both calorimeters, i.e. muons and antimuons. Finally, the tracking devices are submitted to a magnetic field that curves the trajectories of charged particles.

In the design of the CMS detector [26], a particular attention is given to muons: unlike other detectable particles, their energy can not be measured by any of the calorimeters; this measurement only relies on the curvatures of the tracks in the two tracking devices. The degree of curvature of the trajectory of a particle decreases when its transverse momentum

[12]Generally, the studied leptons are reconstructed for $E_T \gtrsim 5$ GeV, and their transverse energy distribution is centered at $E_T \sim 40$ GeV, with a main contribution of leptons from the decays of W and Z bosons.

increases, making the charge and p_T measurements more difficult.

For the research of the Higgs boson in the decay channel $H \rightarrow ZZ \rightarrow 4\mu$, a precise measurement of the quadri-lepton mass is mandatory ($\approx 1\%$ at 100 GeV). Hence the necessity of a precise measurement of the muon momentum, at least for p_T values up to $\sim 100\,\mathrm{GeV}/c$.

For these two reasons, a precise measurement of the muon track curvatures was put forward. Hence the necessity of a large bending power, effective in a wide tracking region: a 4-T superconducting solenoid is used. The tracker, and both calorimeters are positioned inside the solenoid, and subject to its longitudinal magnetic field. The flux is returned through a 10,000-t iron yoke comprising 5 wheels and 2 endcaps, composed of three disks each. The return field extends to a distance of 1.5 m from the solenoid, allowing the integration of 4 muon stations.

The geometry of the CMS detector [27] is illustrated in Fig. 2.5. The subdetectors and the online selection ('trigger') system are presented in the next sections. The emphasis is put on the electromagnetic calorimeter, which plays a major role in the following chapters.

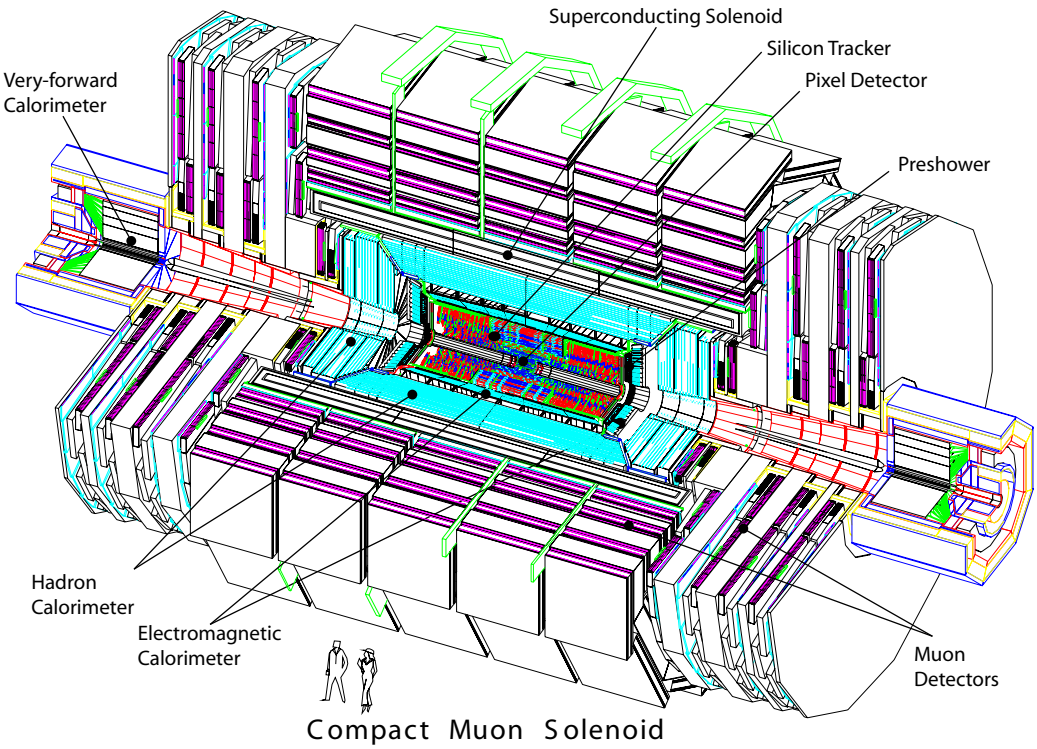

Figure 2.5: A perspective view of the CMS detector. Its length is 21.6 m and its diameter is 14.6 m.

2.2.3 Inner Tracking System

The CMS tracker is a fundamental tool for the charge and momentum measurements on charged particles. Surrounding the interaction point, it has a length of 5.8 m and a diameter of 2.5 m. It covers a pseudorapidity range of $|\eta| < 2.5$. Being positioned directly around the collision point, the tracker material must be very resistant to radiation.

Besides, a very fine granularity in the innermost part is essential to identify the different vertices in a bunch crossing: besides the primary vertex, which corresponds to the interaction point of the spotted collision, secondary vertices can indicate another interaction that occurred during the same bunch crossing (pile-up), or the late decay of a particle[13].

To meet these conditions, the choice was made of a tracker design entirely based on silicon detector technology. This very powerful system has however some disadvantages: it implies a high power density of on-detector electronics, which requires an efficient cooling system. In addition, particles from collisions may interact with the corresponding high amount of dense material, when they cross the tracker (multiple scattering, bremsstrahlung, photon conversion and nuclear interactions), implying complications in their reconstruction and a loss of efficiency and precision. This effect will be detailed when dealing with electron objects, in particular in chapter 4.

The high number of particles crossing the tracker results in a high hit density, which decreases when the distance to the center increases. Under nominal LHC conditions (1000 particles every 25 ns), the hit density reaches:

- 1 MHz/mm^2 at a radius of 4 cm,
- 60 kHz/mm^2 at a radius of 22 cm,
- 3 kHz/mm^2 at a radius of 115 cm.

For a good performance, the occupancy of a detector cell must be kept at or below $\sim 1\%$. Thus, the expected hit density of a given region dictates the granularity.

The CMS tracker is made of two kinds of silicon sensors. Silicon pixels constitute the very fine pixel detector in the most inner part, while the rest of the tracker is made of silicon strips; thicker silicon sensors are used for the outer tracker region in order to maintain a signal

[13] Leptons issued from late decays indicate a background event in the $H \to ZZ^{(*)} \to 4\ell$ ($\ell = e, \mu$) analysis for example (e.g. b quark decays from $Zb\bar{b}$ events).

to noise ratio well above 10. The tracker structure contains several parts of central barrel layers, completed by endcap disks on both sides, as illustrated in Fig. 2.6. For a primary particle, the pixels should provide the three first hits of the track. They allow a very precise measurement of a particle impact parameter and the identification of secondary vertices.

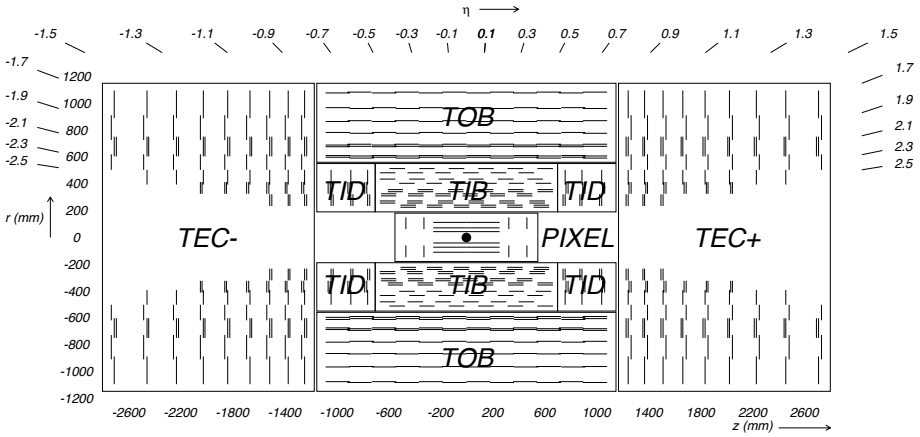

Figure 2.6: Schematic cross section through the CMS tracker. Each line represents a detector module. Double lines indicate back-to-back modules which deliver stereo hits. The pixel detector contains barrel and endcap modules; the silicon strip detector contains two collections of barrel modules: the Tracker Inner Barrel (TIB) and the Tracker Outer Barrel (TOB), and two collections of endcap modules: the Tracker Inner Discs (TID) and the Tracker EndCaps (TEC).

Some details about the detector cells can be found in Table 2.2. Overall, the pixel detector covers an area of about 1 m^2 with 66 million pixels. The silicon strip tracker has a total of 9.3 million strips and 198 m^2 of active silicon area.

	region (as in Fig.2.6)	modules	size in $r-\phi$ and z	occupancy
pixel detector	$r < 10$ cm (PIXEL)	pixel detectors	$100 \times 150\ \mu m^2$	10^{-4} per pixel
silicon strip tracker (1)	20 cm $< r <$ 55 cm (TIB + TID)	silicon microstrip detectors	10 cm $\times$ 80 μm^2	$2-3\%$ per strip
silicon strip tracker (2)	55 cm $< r <$ 110 cm (TOB + TEC)	thicker silicon sensors	up to 25 cm $\times$ 180 μm^2	$\sim 1\%$ per cell

Table 2.2: Structure of the Silicon Tracker Detector.

To prevent risks of thermal runaway[14], the silicon tracker is coupled to a cooling system made of liquid Perfluorohexane (C_6F_{14}), and operates only at a temperature below $-10\,^{\circ}$C.

[14]The increased detector leakage current can lead to a dangerous positive feedback of the self-heating of the silicon sensor and the exponential dependence of the leakage current on temperature.

The expected resolution of the tracker on some track parameters is shown in Fig. 2.7, for muons of different transverse momenta and as a function of the pseudorapidity. The transverse momentum resolution varies according to the tracker modules crossed: a resolution of $\sim 1\,\%$ in the most central region, and raising to $\sim 3\,\%$ for high pseudorapidities, is expected in the p_T range of W and Z boson decays ($p_T \sim 40\,\mathrm{GeV}/c$).

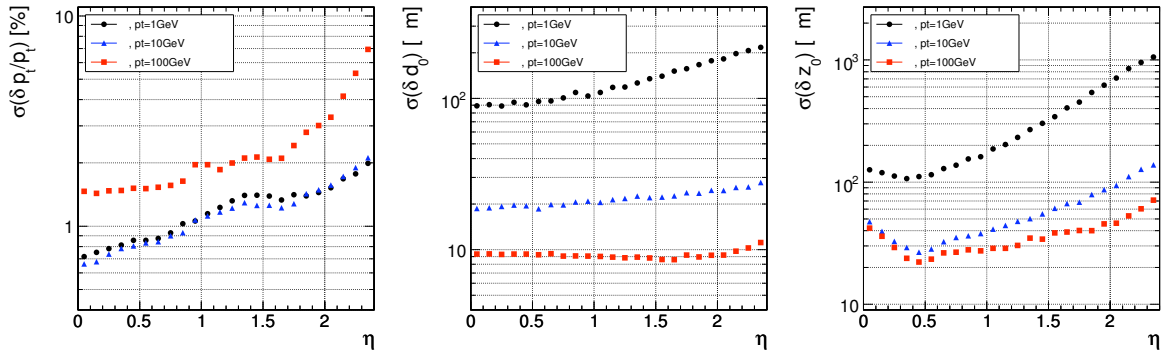

Figure 2.7: Resolution of several track parameters for single muons with transverse momenta of 1, 10 and 100 GeV, using only the tracker information: transverse momentum (left panel), transverse impact parameter (middle panel), and longitudinal impact parameter (right panel).

2.2.4 Electromagnetic Calorimeter

The Electromagnetic Calorimeter (ECAL) was designed according to the requirements of the $H \rightarrow \gamma\gamma$ search. It is the only subdetector to provide information about photons. For a precise diphoton mass reconstruction (a resolution of $\sim 0.1\,\mathrm{GeV/c^2}$), a very precise position and energy measurement (a resolution of a few per mille) must be provided by the ECAL.

The ECAL is also of primary importance for the electron reconstruction in a Higgs boson analysis in a multi-lepton final state. The combination of its information with the one from the tracker must ensure a very precise measurement of electrons (position, momentum) and a significant background removal. A good segmentation is essential to distinguish the energy deposit shape of an electromagnetic particle, from the one of a hadronic particle.

The CMS ECAL is a hermetic and homogeneous calorimeter, that covers the rapidity range of $|\eta| < 3$. It is made of 75848 lead tungstate ($PbWO_4$) crystals, mounted in a barrel ($|\eta| < 1.479$) and two endcaps ($1.479 < |\eta| < 3.0$).

The crystals are followed by photodetectors that read and amplify their scintillation. Avalanche photodiodes (APDs) are used in the barrel. A higher resistivity to radiation and the magnetic field is necessary in the endcaps, hence the use of vacuum phototriodes (VPTs).

The pion population is particularly important in the forward region, and the decay $\pi^0 \to \gamma\gamma$, presenting two photons very close to each others, is quite difficult to distinguish from a single photon. For a better photon identification, a preshower detector is installed in front of the ECAL endcaps.

A longitudinal view of the electromagnetic calorimeter is shown in Fig. 2.8.

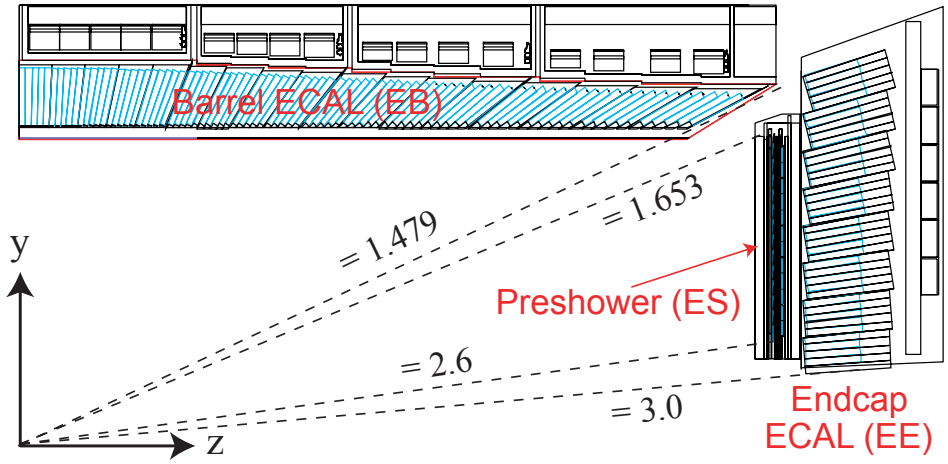

Figure 2.8: Longitudinal view of part of the CMS electromagnetic calorimeter showing the ECAL barrel and an ECAL endcap, with the preshower in front.

2.2.4.1 ECAL Crystals and Geometry

The choice of lead tungstate crystals is driven by the constraints assigned by the CMS detector design. First, to include both calorimeters inside the magnet, the ECAL must be compact. This condition is fullfilled with lead tungstate: its high density (8.28 g/cm^{-3}) and short radiation length[15] (0.89 cm) ensure the possibility to absorb electron and photon showers with reasonably short crystals. Crystals of a length of 25.8 X_0 are used in the barrel and 24.7 X_0 in the endcaps.

A second requirement is the good separability of electromagnetic showers. This is possible thanks to the small Molière radius[16] (2.2 cm) of lead tungstate: in short crystals of a material

[15] A material's radiation length is the mean distance over which a high-energy electron loses all but 1/e of its energy by bremsstrahlung; this is equal to 7/9 of the mean free path for pair production by a high-energy photon.

[16] The Molière radius R_μ is a characteristic constant of a material giving the scale of the transverse dimension

with a small Molière radius, an electromagnetic shower keeps a reasonable size. Hence the use of thin crystals of typical cross section 2.2 cm × 2.2 cm, which ensures a good shower separation.

Finally, the scintillation decay time of the crystals is as fast as necessary for the context of LHC collisions (80% of the light is emitted in 25 ns).

Nevertheless the light output (i.e. the amount of light transferred to the photodetectors) is relatively low and varies with temperature. To ensure a stable response, a cooling system has been installed, maintaining the crystals and photodetectors at a temperature of 18°C ± 0.05°C, decoupled from the cold silicon tracker, and the readout electronics. The temperature is also monitored during data taking.

The barrel part of the ECAL covers the pseudorapidity range $|\eta| < 1.479$, with a granularity 360-fold in ϕ and (2×85)-fold in η. The centers of the front faces of the crystals are at a radius 1.29 m.

In comparison, the endcaps cover the rapidity range $1.479 < |\eta| < 3.0$ and are made of crystals with a slightly larger surface. The longitudinal distance between the interaction point and the endcap envelope is 315.4 cm.

A comparison of the number and dimensions of crystals in the barrel and the endcaps is given in Table 2.3.

	Barrel	Endcaps
number of crystals	61200	14648
crystal cross-section in (η,ϕ)	0.0174 × 0.0174	not fixed
crystal cross-section at the front face	22 × 22 mm^2	28.62 × 28.62 mm^2
crystal cross-section at the rear face	26 × 26 mm^2	30 × 30 mm^2
crystal length	230 mm 25.8X_0	220 mm 24.7X_0

Table 2.3: Ecal crystals.

The crystals are mounted in a quasi-projective geometry to avoid cracks aligned with particle trajectories, so that their axes make a small angle (3° in the barrel, 2° to 8° in the endcaps) with respect to the vector from the nominal interaction vertex, in both the ϕ and

of the fully contained electromagnetic showers initiated by an incident high energy electron or photon. It is defined as the mean deflexion of an electron of critical energy after crossing a width $1X_0$. A cylinder of radius R_μ contains on average 90% of the shower's energy deposition.

η projections.

Structurally speaking, the ECAL barrel is made of 36 identical *Supermodules*, each covering half the barrel length ($-1.479 < \eta < 0$ or $0 < \eta < 1.479$), with a width of 20° in ϕ. Each *Supermodule* is separated into four *Modules* in the η direction (cf Fig. 2.9). The presence of acceptance gaps, called cracks, between *Modules*, complicates the energy reconstruction. A larger crack is present in the border $\eta = 0$ between *Supermodules*, and an even larger one marks the barrel-endcap transition.

Each ECAL endcap is made of two semi-circular plates called *Dees* (cf Fig. 2.9). Small cracks are also present between the endcap Dees, but their effect negligible.

The energy loss in the barrel cracks has been quantified. It is measured by comparing the energy measured in the ECAL with the momentum measured in the tracker on electrons with little bremsstrahlung, considering that the difference is due to energy loss in cracks. The measured loss is of $\sim 3\,\%$ for the gaps in ϕ, affecting regions of $\sim 2°$, and $\sim 10\,\%$ for the gaps in η ($\sim 15\,\%$ in the barrel-endcap transition), affecting regions of ~ 0.01 unit in η. A recovery method cancels these losses for all gaps, except the border $\eta = 0$ and the barrel-endcap transition, where energy losses of respectively $\sim 5\,\%$ and $\sim 10\,\%$ remain.

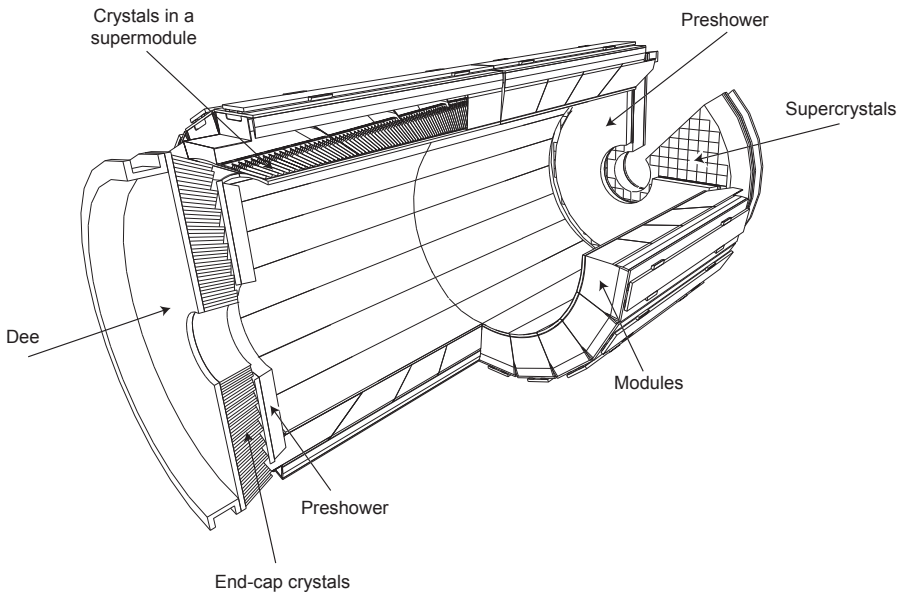

Figure 2.9: Layout of the CMS electromagnetic calorimeter showing the arrangement of crystal modules, supermodules and endcaps, with the preshower in front.

2.2.4.2 Photodetectors

Photodetectors need to be fast, radiation tolerant, and able to operate in the longitudinal 4-T magnetic field. According to the different expected levels of radiation, two different kinds of photodetectors were used for the barrel and for the endcaps; these two devices were developed specially for CMS.

Avalanche photodiodes (APDs) are used in the barrel. Each APD has an active area of 5×5 mm^2; a pair is mounted on each crystal. They are operated at gain 50 and read out in parallel.

Vacuum phototriodes (VPTs) are used in the endcaps. Each VPT is 25 mm in diameter, with an active area of ≈ 280 mm^2; one VPT is glued to the back of each crystal. They have a single gain stage, with a value of ~ 10.2 at zero magnetic field; a 4-T magnetic field lowers this value by less than 10%. In comparison with the APDs, the lower quantum efficiency and internal gain of the VPTs is offset by their larger surface coverage on the back face of the crystals.

2.2.4.3 Preshower

The preshower is a 20-cm thick sampling device, made of two parts located at each end of the tracker, in front of the ECAL endcaps, in the pseudorapidity range $1.653 < |\eta| < 2.6$ (cf Fig. 2.9). Its absorber, made of lead radiators, initiates electromagnetic showers from incoming electrons and photons. Behind each radiator are two layers of silicon strip sensors positioned with orthogonal orientation. These sensors measure the deposited energy and the transverse shower profiles for a better identification of electromagnetic particles.

At a pseudorapidity value of $\eta = 1.653$, the material crossed by a particle in the preshower before it reaches the first sensor plane is $2X_0$, with an additional $1X_0$ before reaching the second sensor plane. A particular attention has been given to a full coverage of lead by silicon sensors, including the effects of shower spread, primary vertex spread, etc.

Each silicon sensor measures 63×63 mm^2, with an active area of 61×61 mm^2, divided into 32 strips. The nominal thickness of the silicon is 320 μm.

An electron or a photon emitted in the direction of the preshower, deposits $\sim 5\,\%$ of its energy in the preshower, and the rest in the ECAL endcap.

2.2.4.4 Laser Monitoring

ECAL lead tungstate crystals are resistant, but not insensitive to radiations: their optical transmission is reduced by few percents during a run. This limited but rapid effect is due to the production of color centers which absorb a fraction of the transmitted light.

The effect is neither constant[17], nor uniform: it is more visible for higher radiations, e.g. higher luminosity, or higher pseudorapidity for a given luminosity. Besides, at the ECAL temperature of 18°C, this effect tends to be compensated by an annealing effect[18].

Under LHC conditions of runs (≈ 10 hours) alternating with machine refills (≈ 1 hour), the crystal transparency has a cyclic behavior, with a progressive degradation during runs (when the radiation effect dominates), and a fast recovery during breaks (due to the annealing).

The magnitude of the changes is dose-rate dependent, and is expected to range from $1-2\,\%$ at low luminosity in the barrel, to tens of per cent in the high η regions of the endcaps at high luminosity.

Such evolutions must be taken into account for a proper calibration of the energy[19]; hence a regular measurement of the crystal transparency, using laser pulses injected into the crystals via optical fibres. The response is normalized by the laser pulse magnitude measured using silicon PN photodiodes. The ratio of the crystal response to the photodiode measurement gives the crystal transparency.

Laser monitoring occurs regularly during runs (during the beam gap[20], in each LHC beam cycle, i.e. every $88.924\,\mu$s). It monitors transparency changes for each crystal at the 0.2% level.

The sensitivity of the energy resolution to the radiation, is illustrated in Fig. 2.10, that shows the π^0 invariant mass history, with and without laser corrections, over a month of data taking [28]. The effect is significantly higher under higher luminosity conditions (in these runs: $\mathcal{L} \sim 10^{31} - 10^{32}$ cm^{-2}s^{-1}), and in more forward regions (these results show only the barrel region). In 2010 and after laser corrections, an ECAL stability of $\sim 0.2\%$ (resp. $\sim 1\%$)

[17] Many years of research showed that the sites of light production are not destructed by radiation.

[18] Annealing consists in heating a material to a temperature higher than the recrystallization temperature, maintaining a suitable temperature, and then cooling. This process is used to change some of the material properties such as strength and hardness: in this case, transparency.

[19] They are also planned to be taken into account in the online selection system, when LHC collisions get to a luminosity close to the nominal value.

[20] The beam gap is $3.17\,\mu$s long; about 1% of this time is used for laser monitoring.

is observed in the barrel (resp. in the endcaps).

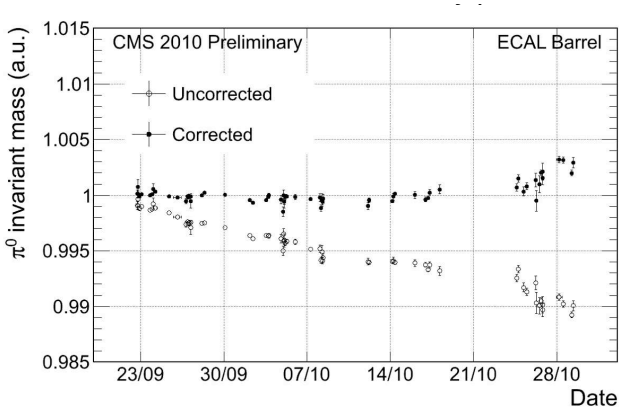

Figure 2.10: π^0 invariant mass history, from the reconstruction of di-photon events in the ECAL Barrel for the last month of 2010 collisions. Histories are shown before and after corrections to ECAL crystal energy due to transparency loss are applied. The invariant mass is normalised to unity at the start of the run period considered.
The last days of this run range correspond to a high luminosity period, for which larger luminosity corrections must be applied.

2.2.4.5 Detector Calibration

The main source of channel-to-channel disparities is the difference between the crystal scintillation light yields. The total variation among all barrel crystals is $\approx 15\%$; the value is higher in the endcaps ($\approx 25\%$), because of non-negligible variations in the VPTs, like the gain.

Corrections from laboratory measurements and calibration of crystal light yield and photodetector/electronics response reduced the channel-to-channel variation to less than 5% in the barrel, less than 10% in the endcaps.

A good precision on intercalibration constants was further achieved for the whole barrel ($< 2\%$) with the use of cosmic rays, with a further improvement for nine supermodules of the barrel ($\sim 0.5\%$) and 500 crystals in the endcaps ($< 1\%$), with electron test beams.

The ultimate intercalibration precision is to be achieved *in situ*, with physics events. The results on 2010 data allowed to uniformize the precision of the intercalibration constants, which is in 2010 $\sim 0.5 - 1\,\%$ in the barrel and $\sim 2 - 3\,\%$ in the endcaps.

Several measurements were combined to obtain this precision: the information from stopped circulated beams (also called splash events) in the barrel was used. Besides, for

barrel and endcaps, two data-driven methods were applied. The ϕ-symmetry method [29, 30] is based on the assumption that the total transverse energy deposited from minimum bias events should be the same for all crystals in a ring at a fixed pseudorapidity[21]. The π^0 calibration method [28] consists in uniformizing the peak positions for individual crystals.

To the intercalibration corrections is added a global correction factor, corresponding to the detector energy scale. The ECAL barrel and ECAL endcap energy scales have been measured *in situ*, using $Z \to e^+e^-$ events collected over the year 2010 ($\sqrt{s} = 7$ TeV, $\int \mathcal{L} = 36\text{pb}^{-1}$). The systematic errors have been evaluated to be 0.5 % for the barrel factor and 1.4 % for the endcap factor in 2010.

2.2.4.6 Energy Resolution

The energy resolution has been measured on one barrel supermodule, using incident electrons, during a beam test in 2004 [31]. The result is shown in Fig. 2.11:

$$\left(\frac{\sigma(E)}{E}\right)^2 = \left(\frac{2.8\,\%}{\sqrt{E}}\right)^2 + \left(\frac{0.12}{E}\right)^2 + (0.30\,\%)^2\,, \tag{2.5}$$

It is made of a stochastic, a noise and a constant contribution. A resolution better than 1% is achieved for electrons of energy higher than 15 GeV; for 40 GeV electrons it is of 0.6%.

These tests correspond to optimal conditions: the electrons hit radially the center of a crystal, so the energy loss corresponding to crystal junctions, and the effect of the angle of incidence variation (due to the magnetic field), are minimized. The same tests applied on electrons hitting uniformly the crystal, showed that after a general energy correction the resolution is $\sim 0.15\%$ worse than the previous results (for 120 GeV electrons).

2.2.4.7 Position Resolution and Alignment

The ECAL position resolution reflects the fluctuations of the energy measurements, and follows the same dependence in energy as (2.5). Studies based on simulations [32] demonstrate

[21] Two factors alter this ϕ-symmetry. The ECAL geometry itself is not uniform in azimuth: because of the non-projective crystal orientation, crystals located at the border of cracks in ϕ are also hit by particles on their side face, and receive more hits than others. The corresponding effect is of $5 - 10\,\%$ in the mentioned regions. Besides the material budget between the calorimeter and the interaction point is not perfectly homogeneous: this results in an inhomogeneous particle flux impinging on the calorimeter. The corresponding effect is generally $\sim 1\,\%$, and $\sim 10\,\%$ in two regions of two crystals each, due to the rails and associated sliding pads used to support the silicon tracker. These factors are taken into account in the so-called *phi*-symmetry method.

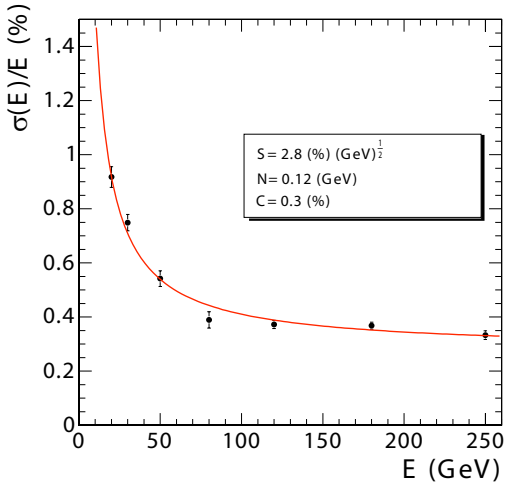

Figure 2.11: ECAL barrel energy resolution, $\sigma(E)/E$, as a function of electron energy as measured from a beam test. The energy was measured in an array of 3×3 crystals with an electron impacting the central crystal. The points correspond to events taken restricting the incident beam to a narrow (4×4 mm^2) region. The stochastic (S), noise (N), and constant (C) terms are given.

that a resolution of about 10^{-3} units in η and 1.6 mrad in ϕ can be reached on 35 GeV electrons; in terms of distance, this corresponds to ~ 2 mm for each coordinate (x, y).

These expectations were confirmed by test beam experiments [33]. *In situ* measurements taken to align the ECAL and the tracker provide similar results.

2.2.5 Hadron Calorimeter

Located behind the Tracker and the Electromagnetic Calorimeter as seen from the interaction point, the hadron calorimeter (HCAL) plays a major role in the measurement of hadron jets. Hence, it should provide a sufficient containment to stop hadron showers. Besides, a wide extension in pseudorapidity is necessary to have a precise description of the total collision event, allowing a reliable measurement of the missing transverse energy, and thereby a measurement of neutrinos and some exotic particles.

From the point of view of a Higgs boson analysis in a multi-lepton final state, the HCAL measurement is very useful to distinguish electrons from hadron jets.

The HCAL is a sampling calorimeter. Like the ECAL, it contains a barrel part (HB) and an endcap part (HE). To follow the containment and wide coverage goals, the HCAL must

be completed by two other calorimeters (HO and HF).

The HCAL Barrel covers the pseudorapidity range $|\eta| < 1.3$; it is radially restricted, between the outer extent of the ECAL and the inner extent of the magnet coil: $1.77\,\text{m} < R < 2.95\,\text{m}$. To ensure adequate sampling depth for $|\eta| < 1.3$, the Hadron Calorimeter is extended outside the solenoid with a tail catcher called the HO, or outer calorimeter.

The HCAL Endcaps cover a wide rapidity range: $1.3 < |\eta| < 3$. The forward hadron calorimeters (HF) placed at 11.2 m from the interaction point extend the pseudorapidity coverage down to $|\eta| < 5.2$.

The structure of the Hadron Calorimeter is illustrated in Fig. 2.12.

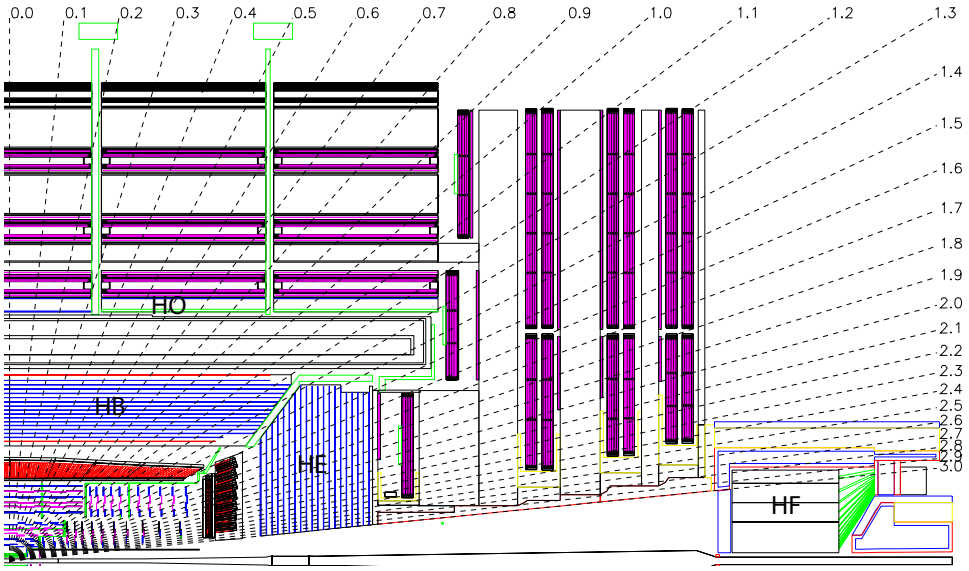

Figure 2.12: Longitudinal view of the CMS detector showing the locations of the hadron barrel (HB), endcap (HE), outer (HO) and forward (HF) calorimeters.

Given the wide pseudorapidity coverage, the calorimeters experience very different particle fluxes. Hence the use of different material, depending on the radiation level, and on the particular goal of each calorimeter.

Flat brass absorber plates are used in the HCAL Barrel, with a segmentation of $(\Delta\eta, \Delta\phi) = (0.087, 0.087)$. The HB effective thickness increases with polar angle (θ) as $1/\sin\theta$, resulting in $10.6\,\lambda_I$ at $|\eta| = 1.3$, where λ_I is the interaction length[22]. The electromagnetic crystal calorimeter in front of HB adds about $1.1\,\lambda$ of material.

[22]Nuclear interaction length is the mean path length in which the energy of relativistic charged hadrons is reduced by the factor 1/e as they pass through matter.

The HO uses the solenoid coil as an additional absorber equal to $1.4/\sin\theta$ interaction lengths and is used to identify late starting showers and to measure the shower energy deposited after HB. Scintillation light from the tiles is collected using multi-clad Y11 Kuraray wavelength shifting (WLS) fibres.

The material in the HCAL Endcaps must face a consequent radiation, and handle high counting rates. Because of the magnetic field, the absorber must be made from a non-magnetic material; finally, the HE must fully contain hadronic showers. These considerations lead to the choice of C26000 cartridge brass. The total length of the calorimeter, including electromagnetic crystals, is about 10 interaction lengths (λ_I).

On average, 760 GeV per proton-proton interaction is deposited into the two forward calorimeters, compared to only 100 GeV for the rest of the detector. For that reason, the HF calorimeter uses a Cherenkov-based, radiation-hard technology, with quartz fibres.

The calorimeter barrel (EB + HB + HO) resolution has been measured on pions of varying energy ($3 - 500$ GeV) by test beams, and found to be:

$$\left(\frac{\sigma(E)}{E}\right) = \left(\frac{84.7\,\%}{\sqrt{E}}\right) \oplus 7.4\,\% \,. \tag{2.6}$$

This resolution is dominated by the HCAL contribution.

2.2.6 The Muon System

In multi-purpose detectors, like CMS, muons are particularly easy to identify and distinguish from backgrounds, thanks to the absorbers constituted by the calorimeters.

Muons play a major role in many physics analyses, particularly for the search of a Higgs boson in a multi-lepton final state. The topology of the final state of $H \to ZZ \to 4\mu$ analysis motivates the construction of a muon system with a wide angular coverage, with no acceptance gap.

Given the shape of the CMS solenoid magnet, the muon systems were divided into a cylindrical barrel section, and two planar endcap regions. 25 000 m^2 of detection planes are used in robust muon chambers.

In this case too, the barrel region is an easier case than the endcaps: less background, a low muon rate, and a uniform 4-T magnetic field, mostly contained in the steel yoke.

Drift tube (DT) chambers were used, with standard rectangular drift cells, covering the pseudorapidity region $|\eta| < 1.2$. Chambers measuring the muon coordinate in the $r - \phi$ bending plane alternate with chambers providing a measurement in the z direction. Each of the four stations contains four chambers of each kind. The main problem of this design is the presence of 'cracks', i.e. dead spots in efficiency, between the chambers. This is solved by an offset of the drift cells between neighbor chambers.

The endcaps cover a region of higher rates, and where the magnetic field is large and non-uniform. Cathode strip chambers (CSC) are used to cover the pseudorapidity region $0.9 < |\eta| < 2.4$. Each of the four stations contains six layers of chambers and anode wires. The chambers are positioned perpendicular to the beam line and provide a precision measurement in the $r-\phi$ bending plane, whereas the anode wires provide measurements of η and the beam-crossing time of a muon. Efficient tools are used to reject non-muon backgrounds and match hits to those in the other stations and in the CMS inner tracker.

A complementary system, consisting of resistive plate chambers (RPC) was added in both barrel and endcap regions, over a large portion of the rapidity range ($|\eta| < 1.6$). These are double-gap chambers, operated in avalanche mode to ensure good operation at high rates: six layers are present in the barrel, three in each endcap. They produce a fast response, with good time resolution but coarser position resolution than the DTs or CSCs. They provide an independent trigger system with good time resolution. Besides, they help to reduce ambiguities in attempting to make tracks from multiple hits in a chamber.

Finally, a sophisticated alignment system measures the positions of the muon detectors with respect to each other and to the inner tracker, in order to optimize the muon momentum resolution. A general representation of the muon system is shown in Fig. 2.13.

The expected resolution of the transverse momentum of muons is of $\sim 10\,\%$ in the barrel and $\sim 20\,\%$ in the endcaps, for muons from W or Z boson decays ($p_T \sim 40$ GeV). For global muon objects, the momentum is measured by the combination of the tracker and the muon system informations. Figure 2.14 shows the effect of this combination: in the p_T range below $\sim 100\,\mathrm{GeV}/c$, the tracker contributes mainly to the transverse momentum measurement. However for higher p_T values, the muon system information provides a significant improvement.

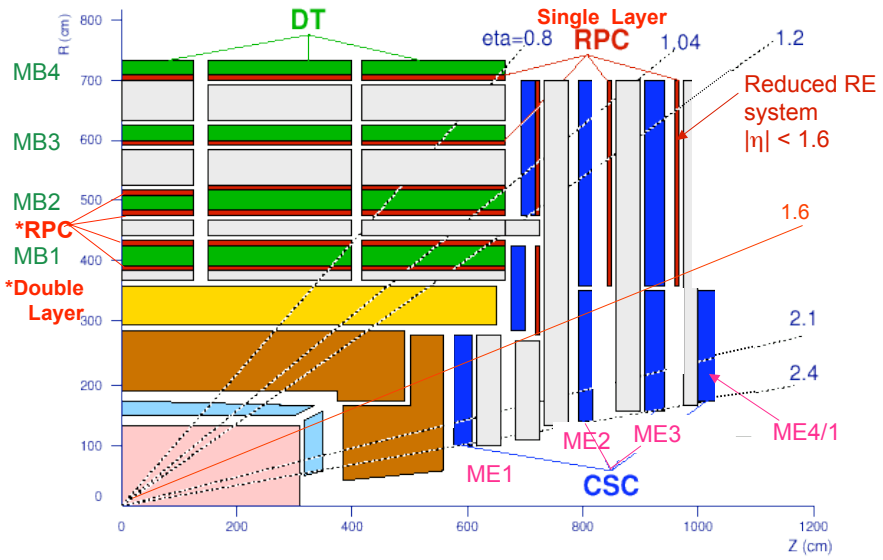

Figure 2.13: Longitudinal view of the muon detectors: DT, RPC and CSC.

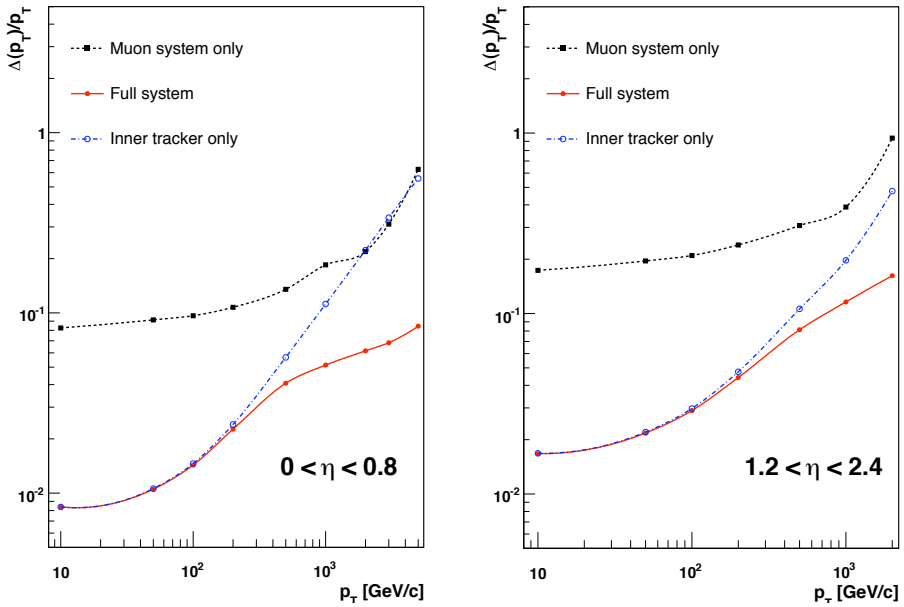

Figure 2.14: The muon transverse momentum resolution as a function of the transverse momentum (p_T) using the muon system only, the inner tracker only, and both. Left panel: $|\eta| < 0.8$, right panel: $1.2 < |\eta| < 2.4$.

2.2.7 Trigger

The trigger system can be seen as the first step of the physics event selection process. Unlike the following steps, this one is not reversible, and needs therefore a very precise upstream study. It performs a fast selection of events likely to be interesting for physics analyses, among the huge amount of events produced by LHC collisions.

This selection must drastically reduce the event rate, from the LHC bunch crossing rate (40 MHz under nominal conditions) to a reasonable rate for data recording, that was fixed at $\sim$ 300 Hz. Besides, all collision data must be kept until the trigger decision, which requires a fast decision.

These constraints lead to a highly flexible two-level trigger system. The Level-1 (L1) Trigger is a hardware system made of largely programmable electronics, that provides a first rate reduction, to 100 kHz, with a fast event scan in a fixed amount of time: 3.2 μs. To satisfy this timing constraint, it considers coarse granularity objects from the calorimeters and the muon system. During these 3.2 μs, the complete high-resolution event information is held in pipelined memories.

If the L1 decision is positive, the complete event information is transferred to the next selection step: the High Level Trigger (HLT). This software system is implemented in a filter farm of about one thousand commercial processors. It is based on algorithms of increasing complexity, that use the fine granularity of the event. Hence the HLT decision time varies according to the event, with a mean value of $< T > \approx$ 50 ms. The HLT can access the complete event data: this flexibility requires a high bandwidth of the order of 1 Tb/s.

In the case of a Higgs boson analysis in a multi-lepton final state, the trigger will naturally search events containing electron or muon signals. For the Level-1 Trigger, an electron signature is a narrow and highly energetic energy deposit in the ECAL, and a muon signature is a track segment or a hit pattern in muon chambers.

The High-Level Trigger considers higher granularity objects (it reconstructs the total energy deposits in the calorimeters, and muon tracks) and combines them with the tracker and preshower information.

2.2.7.1 Level-1 Trigger Architecture

Figure 2.15 describes the Level-1 Trigger architecture: it is divided in two parallel trigger systems (one corresponding to the calorimeters, the other to the muon chambers). Each system is based on a local, a regional, and a global part, after which they are merged into a Global Trigger for the final L1 decision.

Several categories of Level-1 Trigger candidates are created:

- Muon (built in the Muon Trigger);
- Electron/Photon (isolated and non-isolated: e/γ), Jet (central and forward), Tau (built in the Regional Calorimeter Trigger);
- Total Transverse Energy (ΣE_T), Missing Transverse Energy (E_T^{miss}), Scalar Transverse Energy Sum of all Jets (above a given threshold: H_T) (built in the Global Calorimeter Trigger).

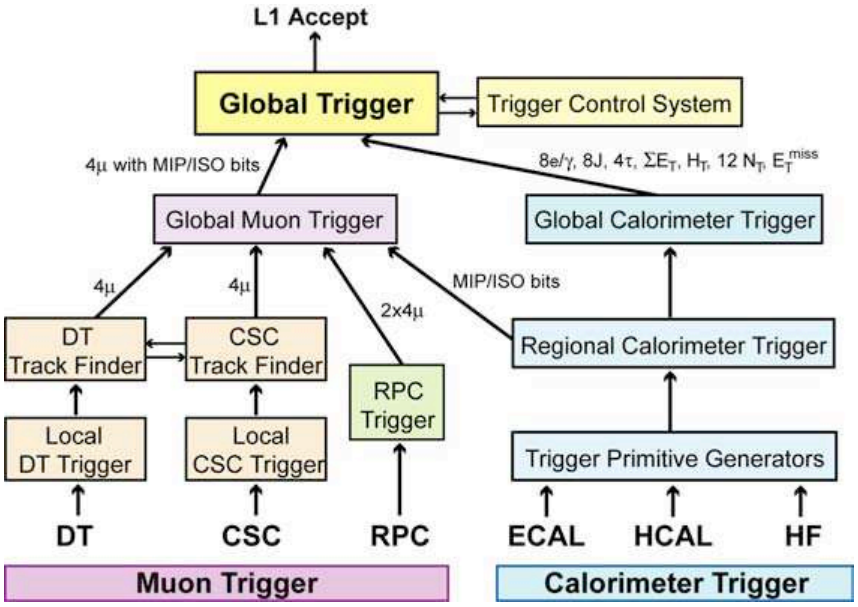

Figure 2.15: Architecture of the Level-1 Trigger.

Local Triggers

On each subdetector the local trigger creates coarse-granularity information. In the calorimeters, this information is a collection of Trigger Primitives.

Regional Triggers

The Regional Calorimeter Trigger collects the local information to build Level-1 Trigger Candidates; it combines the information of both calorimeters, for example for isolation considerations.

For the muon trigger, a DT track finder and a CSC track finder collect the local DT and CSC information to build Level-1 Trigger Candidates as tracks. The RPC trigger is directly regional.

The four most relevant candidates of each category are sent to the Global Calorimeter Trigger, or the Global Muon Trigger respectively. The Regional Calorimeter Trigger also sends the Global Calorimeter Trigger the regional summed transverse energy.

Global Calorimeter Trigger and Global Muon Trigger

Finally, the Global Calorimeter Trigger sorts the Level-1 Trigger Candidates to send the four most relevant ones of each category to the Global Trigger. It also calculates the summed transverse energy (ΣE_T) and the missing transverse energy (E_T^{miss}) of the event, as well as the scalar transverse energy sum of all jets above a given threshold (H_T). This information is also sent to the Global Trigger.

The Global Muon Trigger collects and compares the candidates from the DT, CSC and RPC Triggers. It combines them into four Muon Candidates. It also uses some information from the Regional Calorimeter Trigger for isolation considerations. The four Muon Candidates are sent to the Global Trigger.

Global Trigger

The Global Trigger collects the candidates produced by the Global Calorimeter Trigger and the Global Muon Trigger, and compares them to the Level-1 Trigger Menu. This menu is a list of Level-1 enabled triggers. At most 128 algorithms can be used, possibly prescaled[23], including at most 64 technical triggers[24].

If the candidate collection satisfies at least one of the listed triggers, the Level-1 Trigger decision is positive and the fine granularity event information is sent to the High-Level Trigger. Some trigger rules are also applied at that step, to prevent any memory overload. For example, the Level-1 Trigger can not accept two events separated by only one bunch crossing.

A trigger algorithm can consist in a threshold applied to the highest energetic candidate of one category. For example, 'L1_SingleEG8Iso' requires at least one isolated (i.e. with little activity in the surrounding calorimeter regions) electron/photon candidate with a transverse

[23]When a trigger is expected to have too high a rate at the considered luminosity, two possibilities appear to reduce the rate. Either the trigger conditions are tightened, or this exact selection is kept, but the rate is reduced by a prescaling factor n: only every n^{th} event satisfying the trigger conditions, is accepted.

[24]Technical triggers are based on technical information, like the LHC beam counters, or the CMS beam scintillators. They provide a way to select events independently from the calorimeter information. They can be a very interesting tool to test the trigger efficiency; however they trigger systematically on collision events, and must be highly prescaled, unless the collision rate is very low ($\lesssim 10^{30}$ cm^{-2}s^{-1}).

energy higher than 8 GeV.

A combined condition is sometimes a better way to reduce backgrounds while keeping a good efficiency on physics: for the same rate reduction, the use of a lower threshold is possible; double triggers also exist, like 'L1_DoubleEG5Iso', which requires at least two isolated electron/photon candidates with a transverse energy higher than 5 GeV.

2.2.7.2 High-Level Trigger Architecture

The High-Level Trigger builds candidates corresponding to all kinds of reconstructed objects considered in the offline analyses, using very similar algorithms: photons, electrons and muons, τ-jets and hadronic jets, missing transverse energy... Its inner sub-structure is in several steps of increasing complexity, starting at Level 2.

The Level 2 starts generally with the Level-1 Trigger information, and builds fine granularity objects around the Level-1 candidates, using only the information from the calorimeters and the muon system. The tracker information is used, when necessary, starting at the next level: Level 2.5.

The example of electron candidates

Let us explain the role of each of the three steps described above, for the reconstruction of electron objects. In that case three HLT levels are considered: Level 2, Level 2.5 and Level 3.

At Level 2, energy *clusters*, built from the ECAL and preshower information, are matched to Level-1 e/γ candidates. The remaining energy of the initial particle, that was spread by bremsstrahlung, is then collected, forming what is called a *supercluster*. Some conditions are applied to the *supercluster* transverse energy, its shape, and isolation in comparison with the surrounding ECAL and HCAL regions, for it to be consistent with an electromagnetic signal. At this level, no difference is made between electrons and photons.

Level 2.5 extrapolates the position of the *supercluster* towards the innermost part of the tracker (the pixels), taking the curvature from its measured transverse energy, assuming that this *supercluster* corresponds to an electron. Two hits are searched in the corresponding region in the tracker pixel layers, and in the TEC layers in the forward region, to form a *seed*.

If a track seed is found, Level 3 applies a complete track reconstruction.

The selections on the electron transverse energy, its isolation, its *supercluster* shape, and the width of the matching *supercluster-seed* window, are dictated by the HLT menu.

High-Level Trigger menu

The High-Level Trigger uses around 150 trigger algorithms, and sorts the selected events into several datasets with as little overlap as possible. An event passing at least one of these trigger selections, will be accepted by HLT, flagged according to the passed selections, and recorded in the corresponding datasets.

Selecting exceptional events

The signatures of interesting physics events are likely to provide high energy leptons (electrons or muons), missing transverse energy (corresponding to neutrinos or particles described by theories beyond the Standard Model), or jets (τ-jets, or quark jets). Triggers are developed for all these signatures, in particular very high energy triggers, and coupled triggers (electron-muon, electron-jet...), can select exceptional events.

Besides, the trigger presents a high flexibility and if unexpected events of a different topology are noticed, it can be adapted to select also these topologies. The data recorded in 2010 provided interesting events with a high multiplicity of low-energy charged particle. These events are quite interesting to study long-range, near-side angular correlations [34]. Given the flexibility of the HLT, a dedicated high multiplicity trigger was designed and used to select such events.

2.2.8 Topology of Leptons in CMS

2.2.8.1 Electrons

Being charged particles, electrons (and positrons) interact in the silicon tracker and create hits in the sensors on their trajectory. They are then absorbed in the ECAL, where their energy deposit is measured.

Hence, an electron (or positron) object is the association of a high and local energy deposit in the ECAL with a track in the silicon tracker.

Because of the magnetic field, the electron trajectory is curved: the degree of curvature depends on the electron transverse momentum (p_T), while the orientation of the curvature

determines the charge.

However, the context of CMS complicates the electron (and positron)[25] topology [35]. The high amount of material crossed by an electron while in the silicon tracker (up to $\sim 2X_0$: see Fig. 2.16) enhances the probability to create an electromagnetic shower (the electron emits bremsstrahlung photons, which can convert into electron-positron pairs, and so on). Finally, the high magnetic field bends the trajectories of the charged particles, spreading the shower in the ϕ direction. A typical case of electron with a complicated topology is shown in Fig. 2.17.

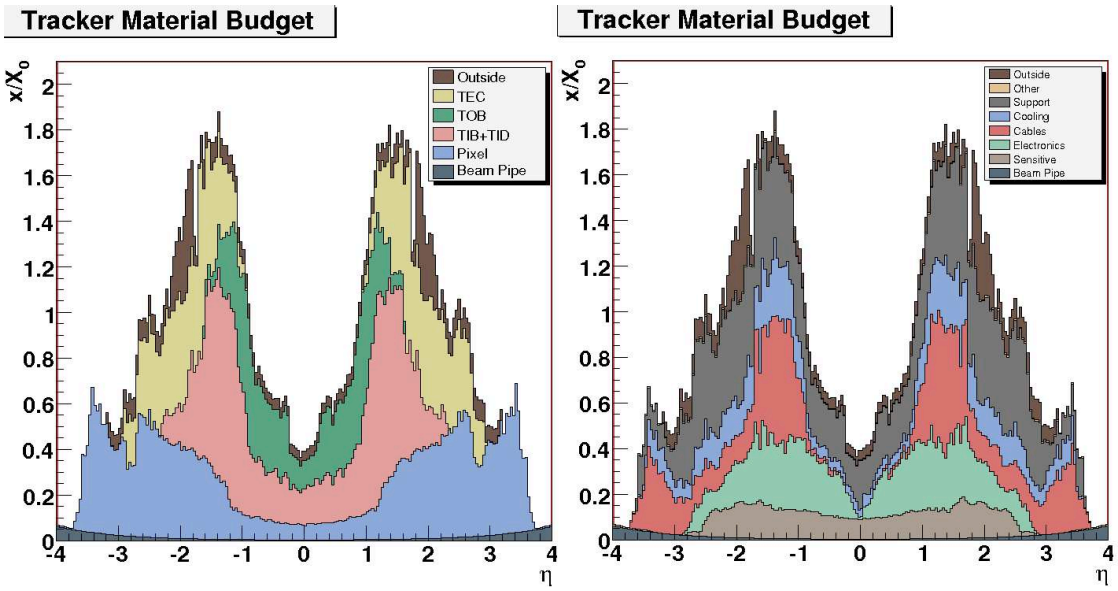

Figure 2.16: Distribution of the tracker material budget with respect to the pseudorapidity (from simulation), in radiation length units.

The variation of the track curvature at bremsstrahlung points is taken into account in the track reconstruction algorithms. In the ECAL, an energy 'cluster' is reconstructed for each particle that reaches the calorimeter[26]. The clusters that correspond to the same shower are assembled into a *supercluster* corresponding to the initial particle.

[25] From now on, unless specified, the word 'electron' will stand for electrons and positrons; positrons will be described as electrons with positive charge.

[26] When a particle hits the ECAL, it initiates a shower of particles, that spread its energy in few crystals: these few crystals are grouped to form a cluster.

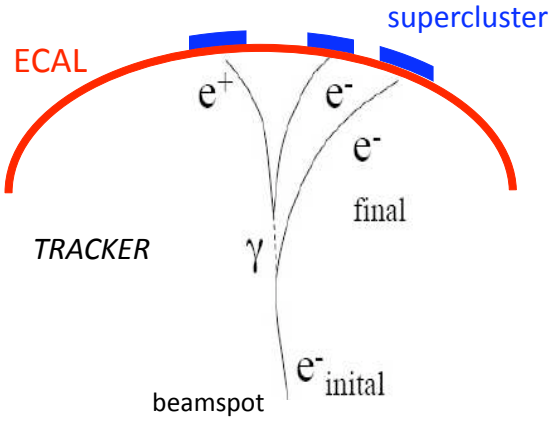

Figure 2.17: An example of complicated electron object: emission of a bremsstrahlung photon, which converts into an e^+e^- pair. Three tracks are present in the tracker, and the energy deposit (supercluster) in the ECAL is spread among three clusters.

2.2.8.2 Muons

Muons (and antimuons), being also charged particles, leave a track in the silicon tracker. They interact little in the calorimeters (ECAL, then HCAL) and keep going through the muon systems.

Hence, muon (or antimuon) objects are the association of two tracks: one in the silicon tracker (or *tracker track*), and a second one in the muon systems (or *standalone track*).

An ideal muon object, called *global muon*, is made of these two tracks: starting from a standalone track in the muon system, a matching tracker track is found and a global-muon track is fitted combining hits from the tracker track and standalone-muon track.

If no complete standalone track is reconstructed, the muon object is built from the inner track: this track is extrapolated to the muon system and matched to a muon segment (i.e. a short track stub made of DT or CSC hits): this is a *tracker muon*.

Finally, if only a standalone track is found, given the very low background rate in the muon systems, the object is also qualified as a muon: a *standalone muon*.

The CMS solenoid subjects the tracker to a 4-T longitudinal magnetic field, and the muon chambers to a return field in the opposite direction, of value ~ 2 T. Hence the trajectory of a muon is curved in opposite orientations in the tracker and in the muon chambers.

The degree of curvature gives the muon transverse momentum (p_T), while the orientation of the curvature determines its charge. For a global muon, these parameters are mainly based

on the tracker information, because of the very precise inner tracking system. However at high p_T the length of the muon systems is very useful as a lever arm.

2.2.8.3 Identification and Isolation

The populations of electron and muon candidates contain contributions from fakes, in particular hadronic jets faking electrons. An identification selection is often applied to reduce these backgrounds. It consists in selecting objects with a characteristic shape.

In the case of muons, restricting the selection to global muons improves the purity. For electrons, that suffer from more background contributions, some parameters are used. The most usual ones are:

- comparison of the supercluster measured position with the one extrapolated from the track, either from the innermost track position or from the outermost track position,
- comparison of the supercluster energy and the track momentum measurements,
- shape of the supercluster (electron superclusters are narrow in the η direction, they often contain additional contributions in the ϕ direction from bremsstrahlung sub-clusters).

Besides, leptons originating from Z boson decays, and more generally leptons used in the analyses presented in this thesis, are isolated, in opposition to leptons emitted inside a jet from a quark hadronization. Isolation conditions can be applied to lepton samples. They consist in measuring the transverse energy in a fixed-size cone around the lepton. Three contributions are measured: the ones in the tracker, in the ECAL, and in the HCAL.

For electrons like for muons, the isolation condition is a set of cuts on these variables, or on these variables normalized to the lepton transverse momentum.

Chapter 3

Performance of the Level-1 Electron and Photon Trigger System

Next in importance to having a good aim is to recognize when to pull the trigger.

David Letterman

Contents

This chapter is dedicated to the study of the Level-1 electron and photon trigger. Section 3.1 describes the context of the first year of LHC collisions from the point of view of the trigger.

The study of the trigger contains two main tasks. On the one hand, a regular check of the good technical behavior of the trigger is necessary, considering the different trigger channels one by one, and the different steps of the trigger algorithm. This study is performed by ECAL shifters and trigger experts, who use a common analysis. When I entered the ECAL prompt feedback group in January 2010 I got acquainted with this analysis and improved it. This analysis and the performed improvements are described in sections 3.2 and 3.3.

On the other hand, the ultimate measurement to be made is the one of the trigger efficiency on offline physics objects. This verifies that the trigger structure is adapted to its function: selecting events containing electrons and photons. I performed these measurements in the different time periods of 2010. These studies are described in section 3.4. The sources of inefficiency were understood. These results were approved by the collaboration and used as reference by physics analyses, and by the trigger teams for the choices of new trigger menus.

3.1 A First Year of LHC Collisions

Proton beams were injected in the LHC in November 2009, followed by proton-proton collisions with a center-of-mass energy of 900 GeV, and then 2.32 TeV, in the end of 2009. After this starting period, the LHC provided stable collisions in 2010, at a center-of-mass energy of 7 TeV and increasing luminosity.

The CMS detector records events according to a trigger system. Under nominal LHC collisions, this trigger must reduce the event rate by a factor $\sim 10^5$, however for lower luminosities a less selective trigger is preferred. Besides a very high efficiency on interesting physics events is essential. The electron and photon trigger plays a major role in the selection of events relevant for the $H \rightarrow 4\ell$ and $H \rightarrow \gamma\gamma$ analyses. The electron trigger is also fundamental for electroweak physics (W and Z bosons), top physics ($\ell+X$ or $\ell\ell+X$ channels), and searches at the TeV scale (e.g. Z').

Figure 3.1 shows the integrated luminosity[1] delivered to, and recorded by the CMS experiment during the 2010 collisions: overall, 47.03 pb^{-1} of data have been delivered, with a data-taking efficiency of 91.79 %. In terms of LHC machine parameters, the last month of collisions corresponded to bunch trains of 150 ns spacing and nominal bunch intensities, with a total number of bunches increasing from 24 to 368 within few weeks. A single test fill with 50 ns was attempted at the end.

As can be seen in Fig. 3.1, the instantaneous luminosity of LHC collisions increased in major and rather abrupt steps during the seven months of collisions, depending on the technical improvements achieved in the machine. These conditions required frequent changes of the trigger menu. It is crucial to control and validate the trigger performance on data, in particular the electron and photon trigger. The study and the validation of the electron trigger performance during the first year of high energy proton-proton collisions at LHC is the purpose of the work described in this chapter.

3.1.1 Evolution of the Trigger Menu

The trigger menu changed a lot according to the LHC luminosity. The first electron/photon trigger to appear in the menu required only a supercluster of transverse energy above 10 GeV

[1]The integrated luminosity has the dimension of an inverse surface: it is the integral, over a given period, of the (instantaneous) luminosity. The number of collisions of one kind, during this period, is the product of the integrated luminosity by the cross section of this kind of collision event.

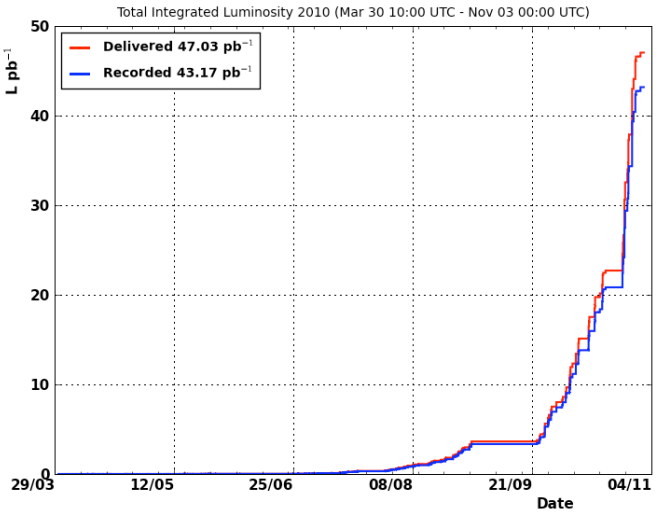

Figure 3.1: Integrated luminosity versus time delivered to (red), and recorded by CMS (blue) during proton-proton stable beams at 7 TeV centre-of-mass energy, in 2010.

(HLT_Photon10). These conditions were then tightened in the threshold and in the selection, and for the data taking conditions of late 2010 runs all unprescaled photon triggers had a threshold above 40 GeV and isolation and/or identification cuts. Over the few hundreds of Hertz of trigger, around 30 Hz were assigned to each category (single electron, double electron, ...).

In the late 2010 recorded data, many different triggers were used on electrons: some examples are given in Table 3.1. Some of them required two electrons passing the same selection[2]. Some other ones required two electrons passing different selections. Finally, some of them required only one electron passing a tight selection.

Double electron triggers that applied the same selection on both electrons, were seeded by Level-1 double e/γ triggers (isolated and non-isolated collections were merged by that time). Single electron triggers, and double electron asymmetrical triggers, were seeded by Level-1 single e/γ triggers.

Several different triggers were used on muons too, requiring one or two muons. Also some triggers required one electron and one muon.

Events selected by electron-related triggers were stored in an '/Electron' dataset; events selected by muon-related, or electron-muon-related triggers, were stored in a '/Muon' dataset.

[2]By selection, one means here: transverse energy threshold, isolation and identification (*supercluster* shape, *supercluster-seed* matching) cuts.

High-Level Trigger name	conditions	Level-1 Trigger seed
HLT_DoubleEle17_SW_L1R_v1	two electrons (same selection)	L1_DoubleEG5
HLT_Ele17_SW_TightCaloEleId_Ele8HE_L1R_v2	two electrons (different selections)	L1_SingleEG8
HLT_Ele17_SW_TighterEleIdIsol_L1R_v3 HLT_Ele22_SW_TighterCaloIdIsol_L1R_v2 HLT_Ele22_SW_TighterEleId_L1R_v3	one electron	L1_SingleEG8

Table 3.1: Some examples of electron triggers used in the latest 2010 data.

3.1.2 Anomalous Signals (Spikes)

The 2009 and 2010 data showed events with unexpected signal in the ECAL, namely anomalous energy deposits.

The anomalous signals were mostly of high energy, as indicated in Fig. 3.2.a, and concentrated in one crystal, unlike electromagnetic energy deposits necessarily spread over few crystals. These signals were observed only in the barrel, and uniformly distributed over the geometrical acceptance.

Their origin was identified as the energy deposited by heavy ionizing particles in the Avalanche Photodiodes. The endcap photodetectors (VPTs) being of a different kind, the signal in the endcaps was not affected by those particles.

These anomalous signals, or spikes, present a different topology than electromagnetic signals. Besides, their reconstruction time is spread on a much wider range[3], as shown in Fig. 3.2.b. To remove these anomalous signals from the collection of reconstructed energy deposits, two conditions are applied: a topology condition, and a timing condition.

The topology condition is a simple cut on a variable that compares the energy of the highest crystal (E_1) to the summed energy of its four direct neighbors (E_4):

$$1 - \frac{E_4}{E_1} < 0.95 \; . \tag{3.1}$$

The distribution of this variable is shown in Fig. 3.3. The cut at 0.95 ensures a good efficiency on normal signal. Only spikes that are embedded in a normal energy deposit will survive this cut, hence the necessity on an additional timing cut.

Anomalous signals are understood and rejected offline. However they are also dangerous for the trigger. Given their narrow shape and their high energy they are very likely to set

[3]Anomalous signals are in time with the collision event. However their pulse shape is quite different, and the time reconstruction is not adapted to them.

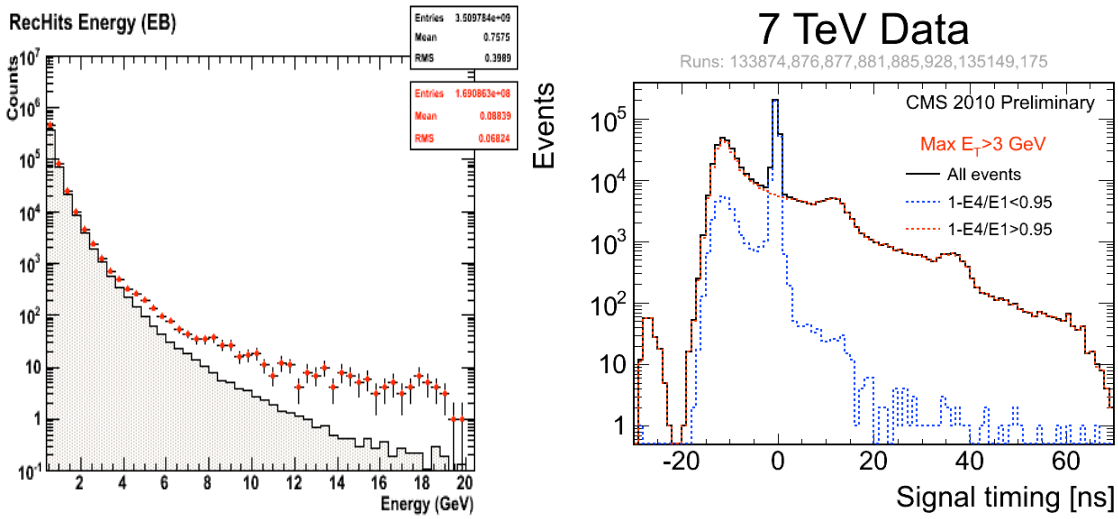

(a) (b)

Figure 3.2: Left: energy deposits in the ECAL barrel: data are shown by red crosses, and simulation, by a histogram. The discrepancies are due to the presence of anomalous signals in data. Right: energy deposit reconstruction time. The red line indicates the contribution of anomalous signals.

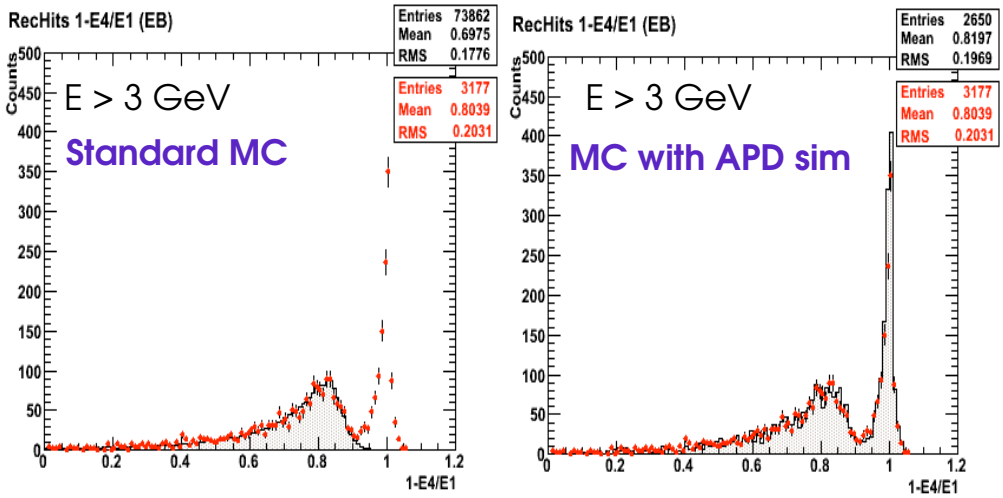

Figure 3.3: Distribution of the variable $1 - E_4/E_1$ for data (red dots) and simulation (histogram): on the right plot, the simulation includes the interactions in the APDs.

off an electromagnetic trigger. Studies on 7 TeV recorded events showed that their rate increases linearly with the rate of minimum bias, with approximately 3×10^{-3} anomalous signals ($E_T > 3$ GeV) by minimum bias event. Besides, their contribution increases with the considered energy, as shown in Fig. 3.2.a. Hence sooner or later an online rejection of these signals is necessary.

The offline topological selection described above was adapted and included in the HLT

algorithms in 2010. A next critical step was the introduction of a pattern recognition at the Level-1 Trigger. The total rate of the Level-1 trigger is limited to $\sim$ 100 kHz, and the contribution assigned to the electron and photon trigger is $\sim$ 15 kHz. The contribution of anomalous signals is expected to largely dominate the Level-1 triggers of a threshold of 20 GeV or greater, with a rate of 65 kHz for a luminosity of 10^{34} cm^{-2}s^{-1}. The luminosity achieved in the end of 2010 ($\sim 10^{32}$ cm^{-2}s^{-1}) presented already a contribution of anomalous signals to the rate of the Level-1 trigger with $E_T > 15$ GeV, of the order of 1 kHz. Hence the necessity to use a pattern recognition at that level from the start of the 2011 data. This was developed and implemented at the LLR, the group responsible for ECAL Level-1 Triggers in CMS. It is used since the first 2011 runs.

3.1.3 Level-1 Trigger

The Level-1 trigger architecture has been described in paragraph 2.2.7. In the following the Level-1 (L1) Electron and Photon trigger algorithm is described in details. The electronics which implements these algorithms have been designed and realized at the LLR [36, 37]. I then present an analysis intended to verify the technical performance of the construction of Level-1 Trigger objects. Finally, the measurement of the efficiency of the Level-1 Electron and Photon Trigger on physics objects, during the 2010 data-taking period, is presented.

3.2 Local Trigger: Trigger Primitive Generation (TPG) Analysis

3.2.1 ECAL Local Trigger, and Trigger Primitive Generation

At the local level, the L1 trigger does not consider the fine granularity of the ECAL in units of crystals, it considers trigger towers (cf Table 3.2). This unit coincides, and is aligned with the HCAL granularity in the barrel. In the barrel, a trigger tower is a square of 5×5 crystals in η and ϕ. In the endcaps, the geometry is less simple and the number of crystals in a trigger tower decreases with the pseudorapidity, in order to follow a projective geometry.

A Trigger Primitive (TP) is created for each Trigger Tower, at each bunch crossing. It is a 9-bit word containing two pieces of information: the transverse energy contained in the tower (8 bits), and the *fine grain veto bit* (FGVB, 1 bit) that characterizes the compactness

Detector	index $\lvert i\eta \rvert$	$\lvert\eta_{\mathbf{max}}\rvert$	$\boldsymbol{\Delta\eta \times \Delta\phi}$
EB	1-17	$0.087 \times i\eta$	0.087×0.087
EE	18-20	$0.087 \times i\eta$	0.087×0.087
EE	21	1.830	0.090×0.087
EE	22	1.930	0.100×0.087
EE	23	2.043	0.113×0.087
EE	24	2.172	0.129×0.087
EE	25	2.322	0.150×0.087
EE	26	2.500	0.178×0.087
EE	27	2.650	0.150×0.087 effective, 0.150×0.175 real
EE	28	3.000	0.350×0.087 effective, 0.350×0.175 real

Table 3.2: ECAL trigger tower granularity.
Concerning the two innermost endcap rings (at highest η), the real granularity is as seen at the local trigger level: it is coarser than for the other towers for geometrical reasons (a same ϕ window corresponds to a much smaller area in this region). When the information is transferred to the regional calorimeter trigger, the real towers are artificially divided in two, recovering an effective granularity in ϕ similar to the ones of the other towers.

of the energy deposit in the tower. This word is transmitted to the Regional Calorimeter Trigger for the construction of Level-1 candidates.

Given the fixed number of bits assigned to the trigger primitive transverse energy (8 bits), the choice of its least significant bit (LSB) is a compromise between the precision and the energy range to be described. The Level-1 electron and photon trigger uses Trigger Primitives; it is expected to be used with thresholds up to $\sim$ 30 GeV; jet triggers also use the TP information, and consider higher energy thresholds: up to $\sim 50 - 100$ GeV. Besides all trigger tower energies higher than the TP saturation value are underestimated, and this estimation enters the measurement of the missing transverse energy (E_T^{miss}), in the corresponding trigger.

In 2010, the trigger primitive energy was quantified in units of 250 MeV (for 1 Analog-Digital Converter (ADC) count), implying a saturation at transverse energies of 64 GeV. For 2011, the decision was made to use the E_T^{miss} trigger and the LSB choice changed to 500 MeV (for 1 ADC count), pushing the saturation to a transverse energy of 128 GeV.

The aim of the fine grain veto bit is to distinguish the shape of the ECAL energy deposit of an electromagnetic particle (electron, photon: $FGVB = 0$), from the one of a hadronic particle (jets, particularly pions: $FGVB = 1$). While bremsstrahlung can cause the energy deposit of an electron or a photon to be spread in the ϕ direction, this deposit is expected to be quite narrow in the η direction[4].

[4] A crystal cross section has the width of the $PbWO_4$ Molière radius, hence $\sim 90\,\%$ of the electron energy is expected to be concentrated in a width of two crystals in the η direction.

In the barrel, a Trigger Tower (5×5 crystals) is subdivided in five strips of 5 crystals in the ϕ direction. The electromagnetic compactness condition is illustrated in Fig. 3.4; it requires that a significant amount of the Trigger Tower transverse energy is concentrated in two consecutive strips. The endcap algorithm follows the same strategy. It is adapted to the irregular geometry of endcap towers: it combines the strip fine grain veto bits ($sFGVB$) of its different strips. This algorithm is not detailed in this thesis.

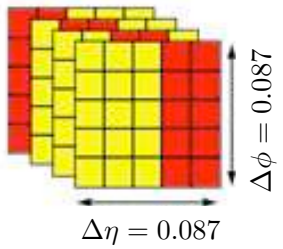

Figure 3.4: Illustration of the fine grain bit algorithm, in the barrel, where a Trigger Tower is made of 5×5 crystals.

Anomalous signals (described in paragraph 3.1.2) present in the ECAL barrel tend to significantly increase the trigger rate. To identify and suppress them, a *spike bit* was developed and tested in 2010, using the strip fine grain bits[5]. It is used since the start of the 2011 data taking. This bit is not transmitted to the RCT, however it is consulted during the Trigger Primitive Generation, and recorded with the TP information, in case the event passes the trigger conditions. Anomalous signals are identified as high energy trigger primitives, with no energy spread in the ϕ direction. Trigger primitives corresponding to this description (i.e. with none of their strips presenting an energy spread in ϕ) are zeroed before being sent to the RCT.

3.2.2 Trigger Primitive Analysis

It is a major issue to control the behavior of the trigger, because any deviation may result in an efficiency loss for the data selection. Two aspects are thoroughly checked during data taking and shortly afterwards: the timing and the stability of the trigger objects. On the one hand, a wrong bunch crossing assignment of the trigger primitives results in the recording of wrong

[5]These channels were present also the ECAL barrel, though used only in the ECAL endcaps.

events. On the other hand, the contribution of noisy channels increases the trigger rate: in cases of high amplitude, even a high trigger threshold does not suppress these contributions, the trigger rate spirals out of control and the data taking must be stopped.

To prevent this, the behaviors of all trigger towers are checked constantly during a data taking period, and more thoroughly a posteriori if necessary. The towers responsible for irregularities must be identified: generally they are masked for trigger decisions in a first time, and unmasked as soon as the problem is solved. Unlike offline processes, the problem cannot be solved by the use of an algorithm, because of the fixed timing of the Level-1 trigger decision, and the fixed Level-1 Trigger architecture. The problem is sometimes solved by a tuning of the constants used in TP generation (e.g. fluctuations of small amplitude are dealt with by using a higher threshold for a non-zero trigger primitive), or by the replacement of some damaged material. Otherwise, a precise identification of the problematic channels prevents the masking of large regions (e.g. one crystal can be masked rather than the whole trigger tower, or the whole region).

Precise tools are necessary for the identification of a problematic tower. An offline analysis has been developed in this purpose: the Trigger Primitive Generation Analysis[6]: it is applied on a chosen uninterrupted data-taking period (a *run*).

This analysis is used regularly by members of the ECAL Prompt Feedback group, as soon as some irregularities are noticed in the trigger rate, or in the general ECAL behavior. It can be launched interactively by a shifter or a member of the group, and its results are presented as distributions, on a webpage (cf Fig. 3.5). I took part in the development of this analysis: I added some options, some complementary information, and I developed the navigation in the webpage and the descriptions of the different distributions. The basic content of the analysis is described in this paragraph, while the next paragraph focuses on the developments that I added.

The TPG analysis shows some typical distributions of the trigger primitives, from which anomalies can be spotted. The results are shown separately for the barrel, and for each endcap; in addition, 2D distributions help to identify irregular trigger towers.

For example, the TP energy spectrum is expected to follow an exponentially decreasing shape, as illustrated in Fig. 3.6. Noisy channels are generally the reason for a hump, or a spike, which becomes problematic if present in the end of these distributions (i.e. for high

[6]In a second time, a more specific analysis can be applied to a problematic tower, in order to identify its responsible crystal.

ECAL TPG Analysis

Run: 140399

L1 Candidates shown in plots below are the ones firing EG2 trigger.

Options used: .

ALL Triggers

More details on these plots can be found on the twiki page

Legend for all plots:

1. **Vertical hatches show towers having cristals masked for readout (based on TTF value).**
2. **Oblique hatches show towers being masked for the trigger.**

General Run Info

Fired Triggers

These plots show the number of times triggers were fired.

1. **"Active Triggers Fired" means triggers for which the algo bit was "true", and enabled by the Global Trigger.**
2. **"Triggers Fired (Before Matching)" means triggers for which the algo bit was "true".**

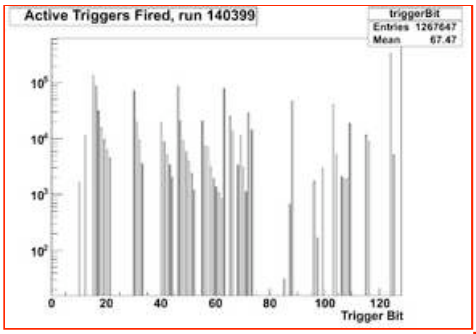

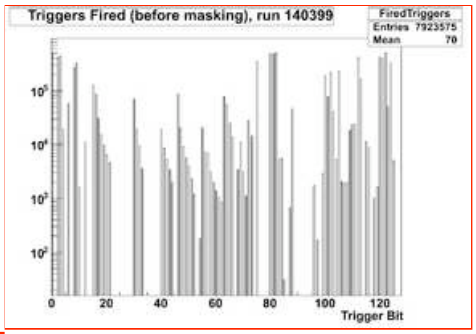

Figure 3.5: The presentation of the TPG analysis page. The analysis is made on a chosen run, with conditions (described in the next paragraph) that are summarized at the top of the page. I customized the page with the options, navigation links and descriptions of the distributions. The distributions show the activity of the different triggers in the run, by trigger bit: before (right) and after (left) the prescale condition.

transverse energies): these channels are easily identified in the 2D distributions, due to their high activity.

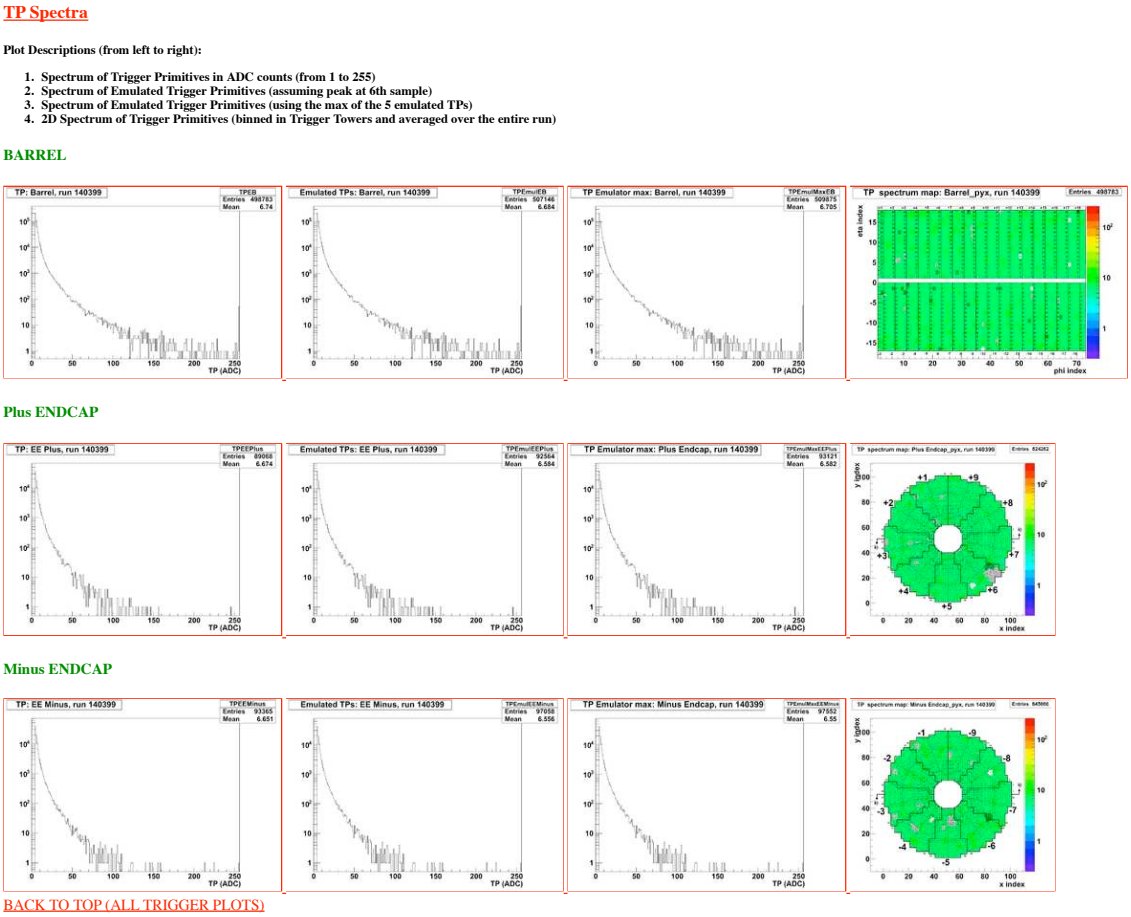

Figure 3.6: An example of distribution shown on the analysis page: the spectrum of trigger primitives, and for comparison, the one of emulated trigger primitives.

If an incident (e.g. trigger overrate) happened at a particular period, it is easily identified with the distributions of the trigger rate vs time (cf Fig. 3.7).

To control the correctness of the TP generation, both in energy and timing, a comparison to the fine granularity recorded information is necessary. In a recorded event, for each tower of transverse energy higher than 1 GeV, the precise information of all crystals is stored ('full readout'). From this information, TPs are emulated offline, with the same parameters as the online trigger system, and compared to the recorded trigger primitives. The information corresponding to one or two bunch crossings before and after the recorded event can also be reconstructed.

Figure 3.8 shows the comparison distributions between TPs (that were used by the trig-

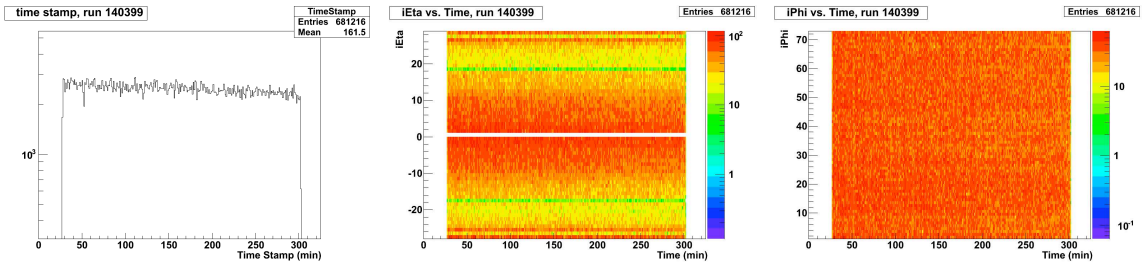

(a) (b) (c)

Figure 3.7: An example of distribution shown on the analysis page: the number of recorded events by time unit. The 2D distributions show this number by coordinate index for the complete ECAL ($1 \leq |i\eta| \leq 17$ for the barrel, $18 \leq |i\eta| \leq 28$ for the endcaps). A sudden trigger overrate would be spotted as a peak in the first distribution, and its origin could be identified by high activity regions in the 2D distributions.

ger) and emulated TPs. It can be checked that, for each event and each tower:

- The TP transverse energy corresponds to an emulated TP transverse energy, in other terms, the energy reconstruction is correct: this corresponds to positive entries in the first distribution; all colors but grey or white in the first 2D distribution.
- This matching is made with the emulated TP of the current bunch crossing, in other terms, the TP timing is correct: this corresponds to the entry 3 in the first distribution, and to the green color in the first 2D distribution.
- The energy in the current bunch crossing is higher than the one in the two earlier and later bunch crossings, in other terms, the time decision is correct: this corresponds to the entry 3 in the second distribution.

If the first 2D distribution is completely green, but the first 1D distribution shows contributions to other entries than 3, then each trigger tower generally behaves as expected, but some of them give sometimes a different answer: these towers can be spotted in the two last 2D distributions.

3.2.3 Improvements of the Trigger Primitive Analysis

The Trigger Primitive Analysis, as described in the last paragraph, is a very powerful tool to check the overall correctness of the ECAL local trigger on a chosen run. In case of irregularities, a corresponding time period, and/or a corresponding trigger tower, can often

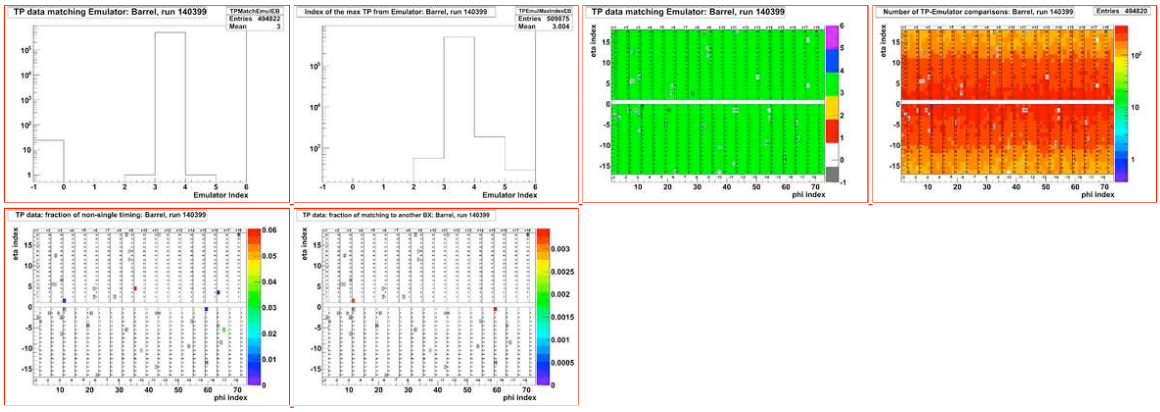

Figure 3.8: An example of distribution shown on the analysis page: the matching of trigger primitives with emulated trigger primitives. The barrel distributions are shown here; similar distributions are made, for each endcap. If the trigger works correctly, the TP is equal to the emulated TP of the current bunch crossing, and higher than the other emulated TPs: the two first distributions are expected to peak at 3, the first 2D distribution should be completely green (for each trigger tower: most generally a matching with the right emulated TP), and the two last 2D distributions should be empty (no exceptions to the good matching indicated in the first 2D plot).

be identified. Improvements were made on this analysis, for a more complete description of a run, keeping in mind two essential goals: the consistency of the trigger primitive generations for all trigger towers, and the primordial control of the trigger rate.

For a case of high trigger rate, with several high activity trigger towers, an estimation of the effect of each of the towers is particularly useful. It is generally a major issue to estimate the effect of a high activity tower: if this effect is not dangerous for the trigger rate, then one prefers leaving the tower unmasked[7]; on the other hand, if this activity is a threat for the trigger stability, a masking is preferable, and the consequent local inefficiency is a low price to pay in comparison with an uncontrolled trigger.

I improved the analysis, so that for a chosen run, one can study the trigger primitives

[7]In case of a signal, the tower response is correct, and the event is triggered; besides the noise does not imply an increase of the trigger rate.

on chosen time periods[8], and/or chosen trigger towers, as illustrated in Fig. 3.9. It can also study only trigger primitives above a chosen threshold: this is quite useful to determine the danger of a high activity trigger tower, because if it is concentrated in the low energy range (significantly below the trigger threshold), it does not have a dangerous impact in the trigger rate.

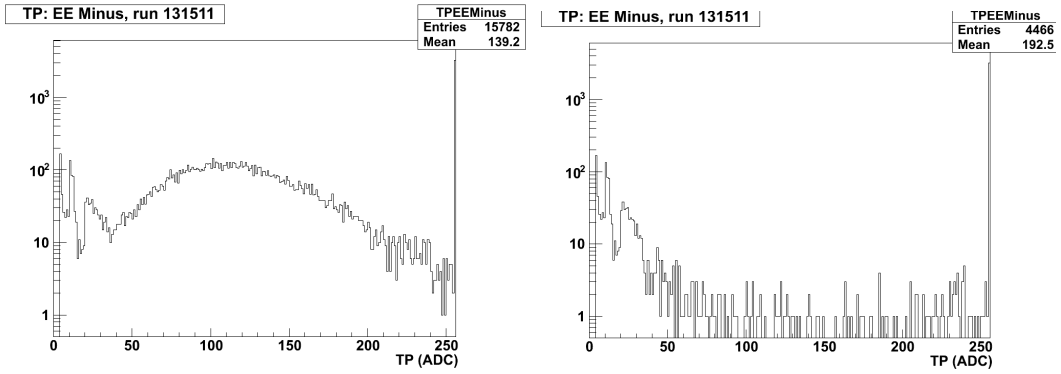

(a) (b)

Figure 3.9: Distribution of the TP spectrum in the ECAL minus endcap for run 136511: for the complete run (left), and removing the trigger tower ($i\phi = 2, i\eta = -23$) (right). This trigger tower is explicitely identified as responsible for the high energy hump visible on the left plot.

Another important aspect of the trigger primitives, is their consistency. The 2D distributions in Fig. 3.6 and 3.8 show a good stability of the trigger primitives, and an adequacy to the emulation; however the presence of white trigger towers remains problematic. The white color indicates that no comparison could be done for these towers: either no trigger primitive was generated, or the recorded data did not contain the information of all crystals, and no emulated TP could be made.

The first case (no TP) is usually due to a mask applied on the tower for trigger considerations: this is a controlled trigger inefficiency, chosen for a good reason. The second case (no emulated TP) is the consequence of a masked crystal for the readout: this is also controlled. If no mask was applied, then these white towers may indicate an uncontrolled trigger inefficiency which must be understood.

In order to differentiate these cases, I extended the analysis to retrieve the masking information, and indicate it by hatches on 2D distributions, as shown in Fig. 3.10: diagonal

[8]These periods can be counted in minutes, event numbers, or luminosity sections. This last option is particularly useful, since the data is validated by ranges of luminosity section.

hatches show towers being masked for the trigger; vertical hatches show towers having cristals masked for readout. Most of the white towers are explained by these masks. The remaining ones were studied individually: they correspond to areas where link errors were noticed in the trigger path; these problems can only be solved by replacing these links (or the transmitters), which requires a long intervention, so for now the trigger primitives are systematically set to 0 in these towers. These links are planned to be changed during the LHC long technical stop at the end of year 2012. In the meantime, the corresponding towers are areas of trigger inefficiency.

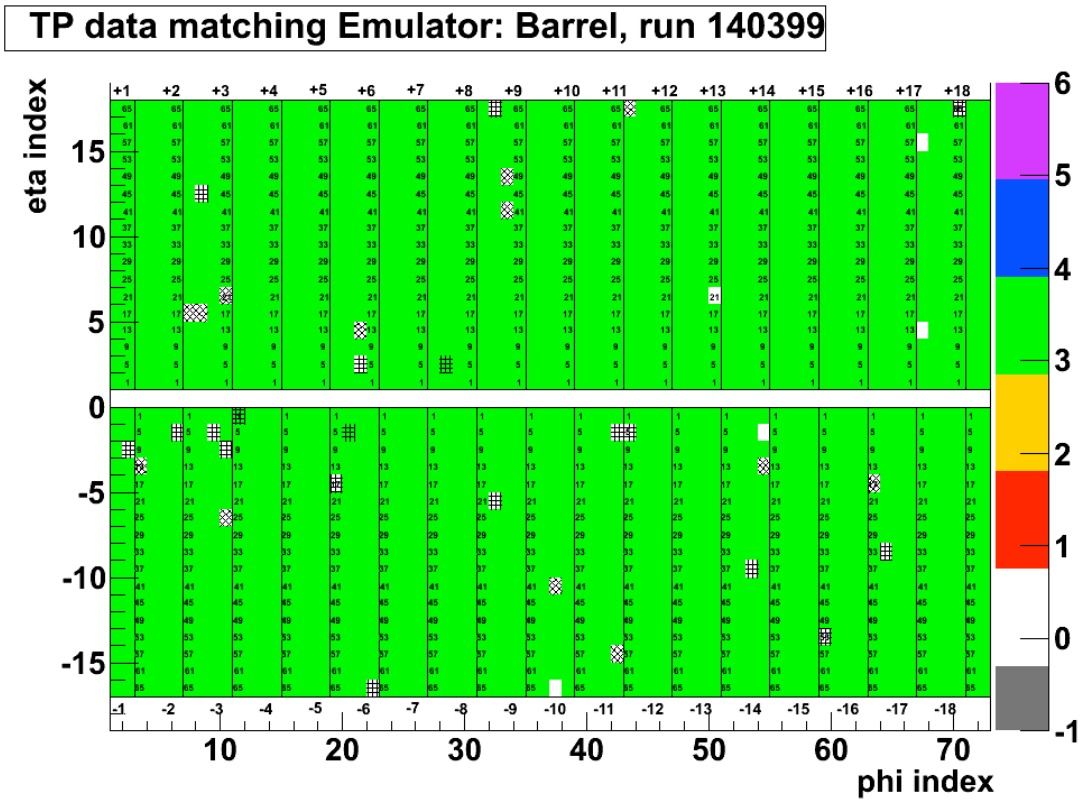

Figure 3.10: An example of distribution shown on the analysis page: the matching of trigger primitives with emulated trigger primitives in the ECAL barrel. This distribution is the same as the third one in Fig. 3.8, zoomed for the hatches to be visible: diagonal hatches indicate towers masked for trigger; vertical hatches indicate towers in which crystals were masked for readout.

3.3 Regional Trigger: Level 1 Trigger Candidate Generation Analysis

3.3.1 Level-1 Electron and Photon Candidate Generation (Regional Calorimeter Trigger)

A region is made of 4×4 Trigger Towers, hence a granularity of $\Delta\eta \times \Delta\phi = 0.35 \times 0.35$ in the barrel. In each region, the Regional Calorimeter Trigger (RCT) collects all synchronized Trigger Primitives, and builds Level-1 e/γ candidates of two kinds: isolated, and non-isolated.

A Level-1 candidate is the sum of the Trigger Primitives built from two adjacent Trigger Towers. Its transverse energy is the sum of the transverse energies of these two TPs; it is coded in 6 bits, with a granularity twice as large as the one of the TPs:

- 500 MeV (for 1 ADC count) for 2010 data, implying a saturation at transverse energies of 32 GeV;
- 1 GeV (for 1 ADC count) for 2011 data, implying a saturation at transverse energies of 64 GeV.

Before computing the sum, correction factors can be applied to the trigger primitives according to their position, in order to compensate some inefficiencies. These were not applied at the start of 2010 data taking; they will be described during efficiency studies, where their utility gets visible.

For the construction of Level-1 e/γ candidates, a sliding window of 3×3 towers in the $\eta - \phi$ plane is used in the electromagnetic and hadronic calorimeters (cf Fig. 3.11). The central tower and its highest energy neighbor constitute the potential L1 e/γ candidate. A compactness condition is applied to the central tower via its fine grain veto bit (requiring $FGVB = 0$). A radial compactness is also required, by applying a cut in the energy deposit in the HCAL tower located right behind the central tower: typically $H/E < 5\,\%$.

For isolated L1 e/γ candidates, an additional *quiet corner* condition is applied in the ECAL. Four corners of 5 towers are formed around the central tower, as illustrated in grey in Fig. 3.11. For at least one such corner, the transverse energy of each of the 5 towers must be below a certain threshold, typically 1.5 GeV. Besides, the FGVB and H/E conditions mentioned above are applied to all towers of the 3×3 window.

During the 2010 data taking, the trigger was used in a simplified way: in particular,

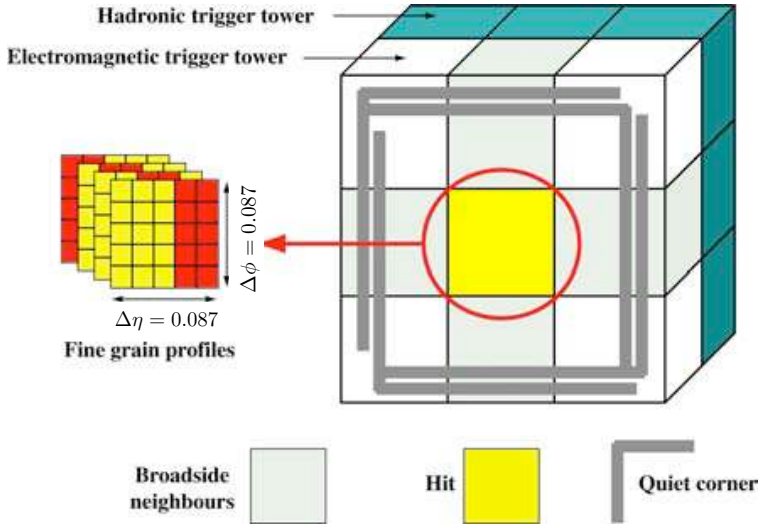

Figure 3.11: Level-1 Electron and Photon candidate algorithm.

the H/E and FGVB conditions were not applied. Only the quiet corner condition made the difference between isolated and non-isolated L1 e/γ candidates. The complete conditions were applied at the start of 2011 data taking.

After their generation in the Regional Calorimeter Trigger, L1 e/γ candidates are sent to the Global Calorimeter Trigger, that orders them and sends the four isolated and the four non-isolated ones with highest transverse energy to the Global Trigger. These candidates take part in the L1 trigger decision, and are recorded with the event in case of a positive trigger decision. So the recorded candidates have the exact characteristics given by the RCT; however only eight candidates are stored for each bunch crossing.

3.3.2 Extension of the TPG Analysis to a Comparison with L1 Candidates

The Trigger Primitive Analysis described in the last paragraph, was extended to the emulation of the highest energetic Level-1 e/γ candidate of a given region, from the online trigger primitives.

Starting with a registered L1 candidate, the Trigger Primitive Analysis searches, in the trigger region corresponding to this candidate, the highest energetic pair of adjacent trigger towers. It calculates the approximated sum corresponding to the L1 granularity, and shows

the ratio $\frac{L1}{TP_1+TP_2}$. This ratio is calculated in ADC counts, hence its expected value[9] is $\frac{1}{2}$.

An example of comparison is shown in Fig. 3.12. The first distribution indicates the isolated L1 e/γ candidate occupancy: the trigger region granularity (4×4 trigger towers) is quite visible in this figure. The uniformity of the distribution of the last plot indicates the agreement of the L1 candidates built by the RCT, with our emulation from the trigger primitives. The same distributions for non-isolated candidates are also displayed in the analysis page.

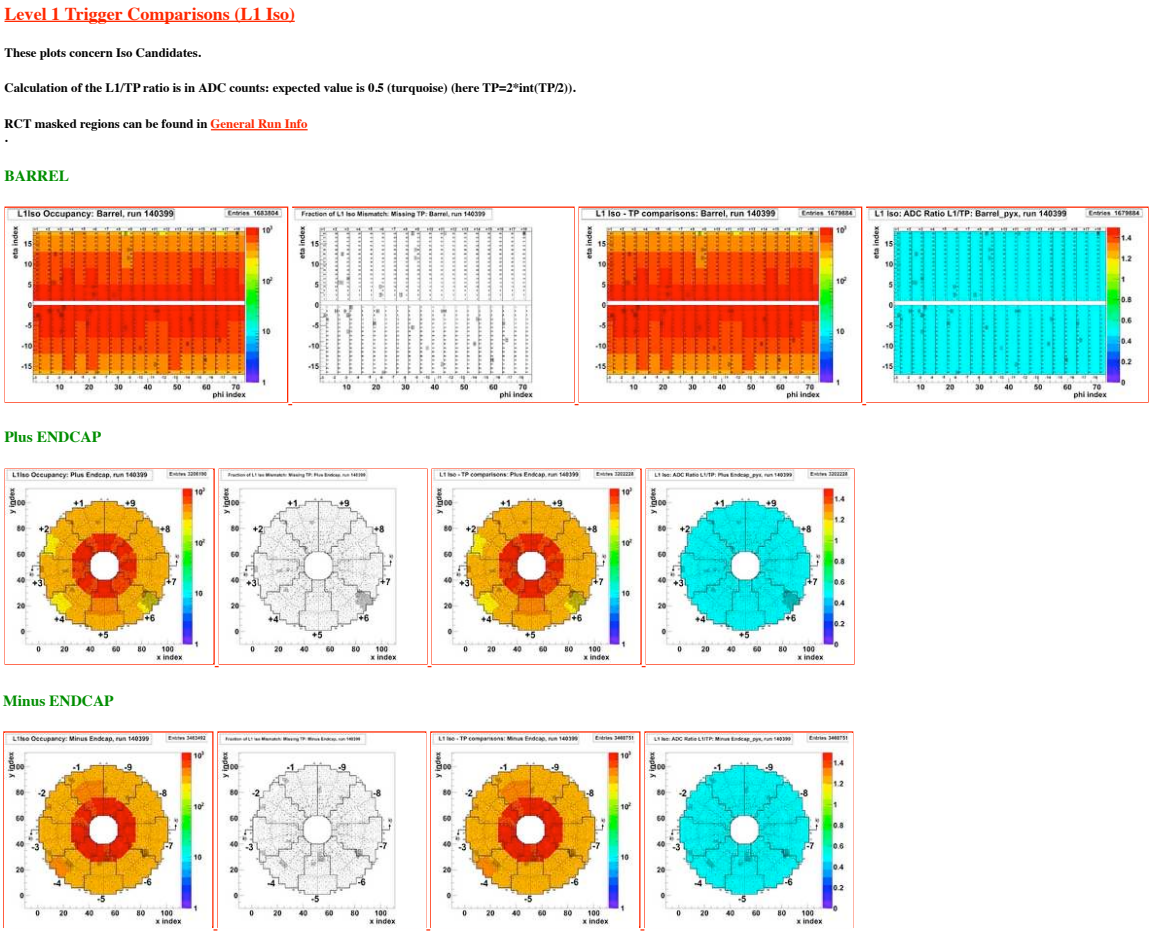

Figure 3.12: An example of distribution shown on the analysis page: a comparison between Level-1 isolated candidates, and their emulation from trigger primitives. From left to right: L1 isolated candidate occupancy; occupancy of L1 candidates for which no TP pairs were found; number of L1-TP comparisons; mean of the ratio $\frac{L1}{TP_1+TP_2}$ for each region (turquoise corresponds to the expected value of 0.5).

Finally, for a registered event, in addition to the eight L1 e/γ candidates of the current

[9] $L1$ and $TP_1 + TP_2$ are expected to have the same value (in GeV), and the L1 candidate granularity is twice coarser than the one for the trigger primitives.

bunch crossing, the eight candidates of the previous and the following bunch crossings are also stored. This information is very useful for an estimation of the pre-firing and post-firing of the trigger, i.e. the cases when the L1 e/γ trigger decision is applied one bunch crossing too early or too late. Taking events that were recorded independently of the L1 e/γ trigger[10], the proportion of L1 e/γ candidates found in the previous or in the following bunch crossing is the proportion of pre- or post-firing of the L1 e/γ trigger.

Timing distributions for the L1 candidates are also displayed on the analysis page, as illustrated in Fig. 3.13. The measured proportions of pre-firing ($\lesssim 1\,‰$) and post-firing ($\lesssim 1\,\%$) are satisfyingly small.

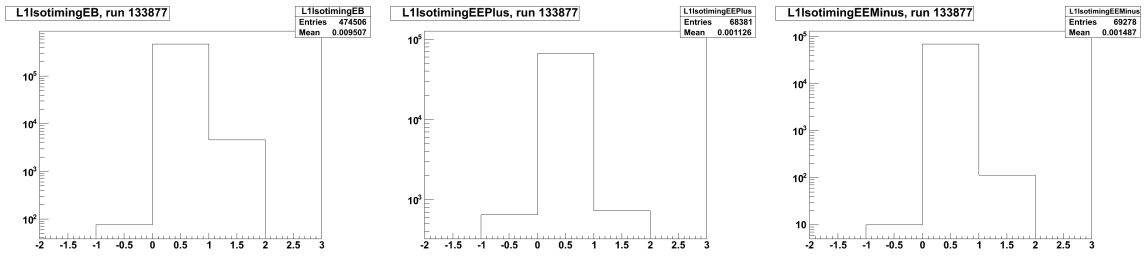

(a) (b) (c)

Figure 3.13: An example of distribution shown on the analysis page: timing distribution of the isolated L1 e/γ candidates, for events recorded by minimum bias triggers. (a): ECAL barrel, (b): ECAL Endcap (Positive η), (c): ECAL Endcap (Negative η). The rather high proportion of postfiring in the ECAL barrel ($\sim 1\,\%$) corresponds to anomalous signals (the example given here is a run in 2010). In 2011 data the spike cleaning is applied also for the Level-1 trigger, and the proportions of pre- and postfiring are both at the per mille level.

3.4 Measurement of the Level 1 Trigger Efficiency on Physics Objects

3.4.1 Particularities of Trigger Efficiency Measurements

3.4.1.1 Efficiency on Physics Objects

The role of the Level-1 e/γ trigger is to set off the recording of events containing electrons or photons passing a chosen transverse energy condition. As a first verification, the Trigger Primitive analysis checks that the trigger technically behaves as expected. However, even for a correct technical behavior, a significant difference is expected between a physics object like an electron or a photon, and the Level-1 trigger candidate that it generates. This motivates

[10]Ideally for such a study, events recorded by Minimum Bias triggers, i.e. based on scintillator counters, are chosen. Hence they are independent from the CMS trigger timing.

a direct efficiency measurement on chosen physics objects. Four main reasons explain the differences between physics objects and their corresponding L1 candidates:

- Containment: as mentioned in paragraph 2.2.8, the energy deposit of an electron or a photon in the ECAL has a varying size, depending on the number of final particles reaching the ECAL (by effect of bremsstrahlung and conversions), and on its transverse momentum. However the size of a Level-1 trigger candidate is constant: two trigger towers. Hence a varying fraction of the particle transverse energy can be reconstructed in its Level-1 candidate.

- Preshower energy: a particle emitted in the direction of the endcaps, crosses the preshower before reaching the ECAL endcaps; it leaves generally $\sim 5\,\%$ of its energy in the preshower. Level-1 trigger candidates are built from the ECAL endcap crystal information only: consequently, they are expected to slightly underestimate the particle transverse energy. Besides, the fraction of energy left in the preshower varies, which implies a poor resolution.

- Effect of trigger masks: a Level-1 candidate is usually based on the two adjacent trigger towers where the physics object leaves most of its energy. However if one of them is masked for trigger considerations, the candidate considers the next best one. Hence, except if the particle energy is concentrated in one masked trigger tower, the effect of a mask is not the absence of a trigger candidate, but a lowered transverse energy.

- Energy determination: finally, for a given pair of adjacent trigger towers, the trigger object construction approximates the transverse energies, with a precision of 250 MeV for TP's and 500 MeV for L1 candidates during 2010 data.

3.4.1.2 Global Strategy

A study of the efficiency of Level-1 single e/γ triggers, on offline electrons or other electromagnetic objects passing a chosen selection, is presented here. In the 2010 period of data taking, two different thresholds were studied, according to the period: L1_SingleEG5 (with a threshold of 5 GeV) and L1_SingleEG8 (with a threshold of 8 GeV); besides, extrapolations for the choice of the 2011 trigger menu were made with the full 2010 statistics: L1_SingleEG12 and L1_SingleEG15 were then studied. To probe the efficiency, the principle match geomet-

rically each selected electron with a Level-1 e/γ trigger candidate, and then compare the transverse energy of the found candidate to the studied trigger threshold. These candidates are the trigger candidates that were used for the trigger decision, and recorded together with the event.

If a selected electron is matched to a candidate with a transverse energy higher than the threshold, then the studied trigger was efficient on this electron; on the other hand, if no candidate was matched to the electron, or if the candidate had a transverse energy lower than the threshold, the trigger was inefficient.

I then studied the identified cases of inefficiency, in order to understand the source of the inefficiency and consider possible improvements.

3.4.1.3 How to Make an Unbiased Measurement

The measurement of the trigger efficiency on data events must be done carefully to avoid possible biases, since the data sample contains events that were recorded by the trigger under study. Two different strategies can face this difficulty:

- The first method is to work on events that were selected by a different trigger system: e.g. events selected by muon triggers, to study the efficiency of the electron and photon triggers. This strategy is unbiased, however its major inconvenient is the low statistics, as the selected events do not contain electromagnetic objects in general.

- The second strategy is to work on events selected by the studied trigger, identify the physics object(s) that fired the trigger, and measure the efficiency on another object of the event. For the study of single triggers, the object that fired the trigger is simply the one attached to the trigger candidate of highest transverse energy, provided this transverse energy is higher than the single trigger threshold.

3.4.1.4 Matching of the Offline Object to the Trigger Candidate

Electron and photon objects contain a reconstructed supercluster that collects the energy deposited in several clusters of crystals. Going through all of these crystals, one makes the list of the trigger regions where the supercluster leaves a non-negligible part of its energy. If the studied physics object generated a trigger candidate, it must be in one of these regions.

The four isolated and four non-isolated trigger candidates of highest transverse energy are stored in the event. Hence, if an event contains four superclusters of higher transverse energy than a physics object, this object is not considered for trigger efficiency measurements: the absence of matched candidate would be due to the limited number of candidates allowed in the system and not to a trigger inefficiency.

Finally, if a supercluster spreads on a small part of a trigger region, the trigger candidate present in this region could be due to additional activity present in the region. Such circumstances are generally prevented if a calorimeter isolation condition is applied to the physics objects. If no such isolation is applied, the analysis requires the absence of a supercluster with higher transverse energy in the considered regions.

3.4.2 Measurement on Minimum Bias Data

3.4.2.1 An Unbiased Selection of Electromagnetic Objects

Choice of an unbiased sample

During the initial period of 7 TeV collisions in 2010, the LHC instantaneous luminosity was quite low, with few proton bunches in the vacuum tube. Because of the low collision rate, and CMS could record a large sample of events via minimum bias triggers, therefore independently of the triggers foreseen for higher luminosity. Minimum bias triggers are based on the detection of proton bunches in the vacuum tube and in coincidence, also coinciding with some activity in the Beam Scintillator Counters (BSC), located in front of the HCAL Forward calorimeter. Such a trigger basically sets off the recording of inelastic proton-proton collisions.

This event selection independent of the Level-1 e/γ system, was a good opportunity to measure the efficiency of the Level-1 e/γ trigger [38, 39]. When the instantaneous luminosity increased, the use of the designed electron and photon trigger became necessary for the data taking. However an 'ECAL activity' trigger, based on Minimum Bias conditions, was developed for Level-1 e/γ trigger studies. This trigger requires Minimum Bias conditions at Level-1, with a prescale, i.e. a reduction factor[11] that ensured a reasonable rate, and the presence at High-Level Trigger of an ECAL supercluster passing a chosen transverse energy threshold. Hence an event selection unbiased from the Level-1 e/γ trigger, and enriched in

[11] If a trigger rate is too high for a given luminosity, the events selected by this trigger can be considered as interesting per se, even if only a subset of them is recorded. In such cases, the trigger rate is reduced by a prescaling factor n: only every n^{th} event satisfying the trigger conditions, is accepted.

electromagnetic objects, was provided.

For the first five months of data taking, the trigger efficiency was measured on events selected by these triggers, independently of the Level-1 e/γ trigger.

Electromagnetic objects

The very first measurements were made on samples of ECAL superclusters. These objects are common to electrons and photons, however their population, without any selection, is largely dominated by hadronic contributions. As soon as the population of candidates from real electrons gained statistics, one was tempted to apply the efficiency studies to these objects. However also the electron populations in minimum bias events were largely dominated by hadron fakes, and to a lower extent, photon conversions. While a simple selection can enrich the population in prompt electrons, no pure population is obtained unless a resonance condition or a higher p_T threshold is applied. Figure 3.14 indicates that for standard electron selections (cf Annex B) designed for isolated electrons in the W/Z region (all distributions except the yellow one), a proportion of fakes of at least 40 % remains, on electrons in the transverse momentum range corresponding to the study of the L1_SingleEG8 trigger[12].

In order to select a population of electromagnetic objects, a selection of electrons from conversions was developed. Minimal isolation and identification conditions are applied to the electron candidates; in order to identify conversions, the electron track must have left no signal in the innermost layer of the tracker, and a second track, corresponding to the second leg of the conversion, must be found with the same origin. Figure 3.14 indicates in yellow the composition of this selection: a proportion of electrons from conversions of $\sim 84\,\%$ is expected, based on simulation results.

3.4.2.2 Results

Efficiency on electrons from conversions

Figure 3.15 shows the measured trigger efficiency of L1_SingleEG8, on electrons from conversions, as a function of the electron supercluster transverse energy in the ECAL[13]. The turn-on

[12]The selection requires $8\,\mathrm{GeV}/c < p_T < 20\,\mathrm{GeV}/c$, corresponding approximately to the turn-on region. The momentum distribution of electrons from minimum bias events is exponentially decreasing, hence the studied electrons have mainly $p_T \sim 8\,\mathrm{GeV}/c$.

[13]The energy deposit in the preshower is not counted: this allows to identify the effect of the other factors mentioned in paragraph 3.4.1. Besides, it allows a direct comparison of the barrel and endcap performances.

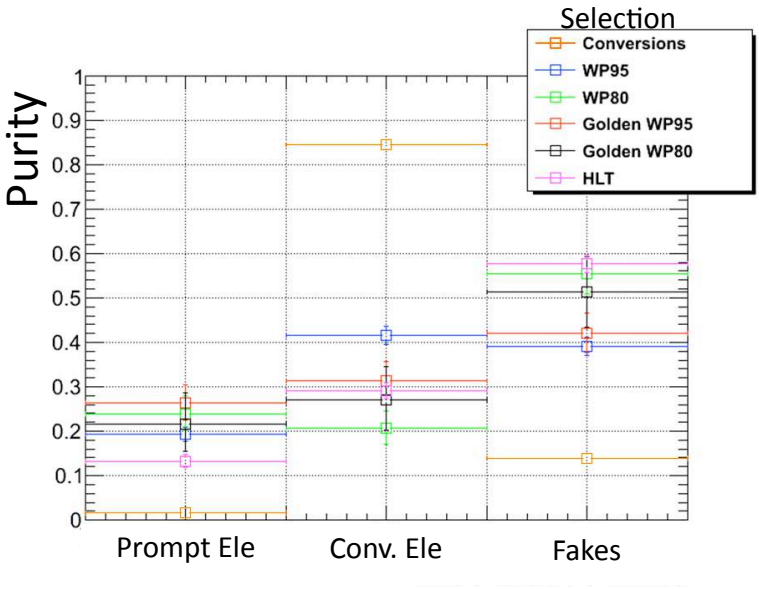

Figure 3.14: Expected purity (from Monte Carlo) of several standard electron selections (cf Annex B), and of the selection of electrons from conversions (shown in yellow), on Minimum Bias events, for electron candidates with a transverse momentum of 8 to 20 GeV/c.

of the trigger efficiency starts at the same point for the barrel and the endcaps, however it is significantly sharper for the barrel. This is mainly due to the fact that endcap electron superclusters usually cover more trigger towers than barrel electron superclusters. Besides the proportion of masked towers for the trigger was also slightly higher in the endcaps.

Detector	50 % efficiency	95 % efficiency	width: $20-80$ % efficiency
EB	10.41 GeV	18 GeV	5.1 GeV
EE	12.54 GeV	19.99 GeV	5.2 GeV

Table 3.3: Turn-on transverse energy of L1_SingleEG8 on electrons from conversions.

For an electron of a given transverse momentum, the size of the supercluster depends on the amount of bremsstrahlung and possible conversion of the bremsstrahlung photons; besides, a bremsstrahlung or a conversion that occurs in an inner region of the tracker results in a larger ϕ extension. Hence the size of an electron supercluster depends on the amount of material crossed on its trajectory, and more particularly the amount of material in the innermost part. Since the amount of material present in the innermost tracker region, the pixel detector, increases with the pseudorapidity (cf Fig. 2.16), the size of a supercluster behaves likewise.

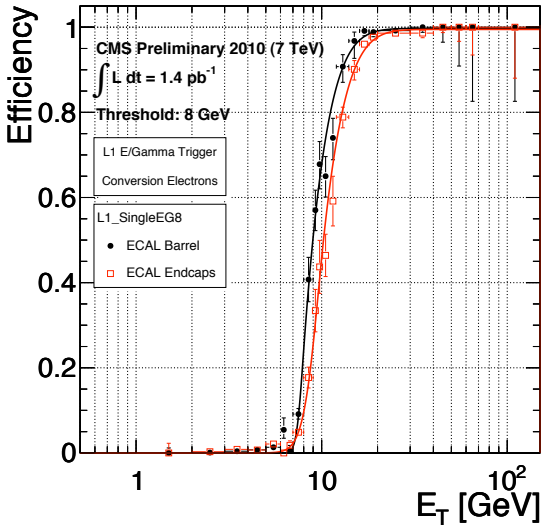

Figure 3.15: Efficiency of L1_SingleEG8 on electrons from conversions: the measured efficiency for electrons in the ECAL barrel (resp. the ECAL endcaps) is indicated by black dots (resp. red squares). The curves represent unbinned fits of the distributions, with the same color code.

Intrinsic efficiency

As a trigger tower always has the same width in the ϕ direction: 0.087 rad (cf Table 3.2), an electron supercluster tends to be spread on more trigger towers when its pseudorapidity is higher. This tendency is increased in the endcaps because of the less regular geometry of trigger towers. This effect is illustrated in Fig. 3.16, for superclusters in general. The distribution on the left shows the size of the supercluster, in units of trigger towers, that is significantly higher in the endcaps than in the barrel. Figure 3.16.b shows the trigger intrinsic efficiency, for superclusters contained within two unmasked trigger towers: the efficiency turn-ons are much sharper than in Fig. 3.15. A similar, quasi-immediate response is observed for barrel and endcaps, except for the innermost endcap trigger regions (shown in blue).

This difference is explained by the particularity of the two innermost trigger tower rings, mentioned in Table 3.2: one tower in the geometrical sense (one 'real' tower), is divided in two 'effective' trigger towers, containing each a trigger primitive with a half of the measured energy, when the information is transferred to the RCT. Hence what is considered as a (real) tower for the supercluster, counts like two distinct (effective) towers for the construction of a Level-1 trigger candidate. The constraint of containment of superclusters in two trigger towers, does not have the same impact in these particular regions.

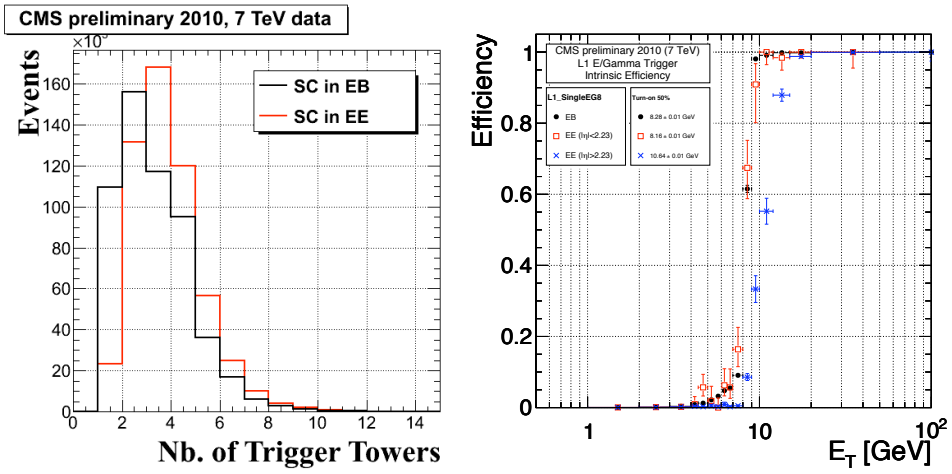

(a) (b)

Figure 3.16: Left: number of trigger towers over which a supercluster is spread. Right: intrinsic efficiency of L1_SingleEG8, measured on superclusters contained in two trigger towers unmasked for the trigger. The measured efficiency for superclusters in the ECAL barrel is indicated by black dots; for the endcaps except their innermost regions, by red squares; for the ring of innermost endcap trigger regions, by blue crosses.

Trigger correction factors

The comparison of Fig. 3.15 and Fig. 3.16.b indicates that the proportion of an electron supercluster energy contained in the surface of a Level-1 candidate, varies significantly with the pseudorapidity, implying a slow-down of the efficiency turn-on. To compensate this effect, η-dependent correction factors were calculated and applied to the trigger primitives by the Regional Calorimeter Trigger (RCT), before the building of Level-1 candidates. One shall however keep in mind that the average size of an electron supercluster, given an amount of material to be crossed, increases when the electron transverse momentum decreases: as a consequence, these factors are adapted to the lowest trigger threshold used, and updated with it. The effect of these correction factors on the Level-1 e/γ trigger efficiency, for electrons from conversions, is shown in Fig. 3.17. The comparison of Tables 3.3 and 3.4 shows that these correction factors imply an earlier and sharper turn-on of the trigger efficiency. However the trigger performance remains less efficient in the endcaps than in the barrel.

Trigger efficiency for different electron selections

I also compared the Level-1 trigger response to the different selections of electron candidates

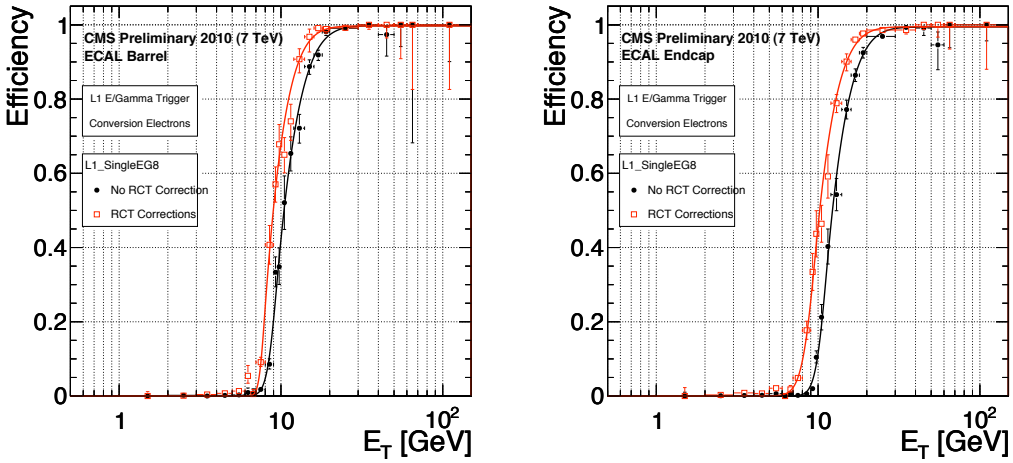

(a) (b)

Figure 3.17: Effect of the RCT correction factors on the Level-1 e/γ trigger efficiency, on electrons from conversions (L1_SingleEG8 is studied): (a) in the ECAL barrel and (b) in the ECAL endcaps. Black dots show the efficiency without RCT corrections; red squares show the efficiency with RCT corrections. The curves represent unbinned fits of the distributions, with the same color code.

Detector	50 % efficiency	95 % efficiency	width: $20-80$ % efficiency
EB	8.89 GeV	14.54 GeV	3.26 GeV
EE	10.32 GeV	17.22 GeV	4.07 GeV

Table 3.4: Efficiency of L1_SingleEG8 on electrons from conversions, using RCT correction factors.

described in Fig. 3.14 (cf Annex B). Though their rather low purity in electromagnetic objects, these selections present the interest of providing different topologies of objects (more or less narrow, more or less isolated):

- For isolation and identification conditions, the 'conversion', 'WP95' and 'WP80' selections use similar variables, with an increasing tightness.
- The conversion rejection variables are the same for 'WP95' and 'WP80', with tighter cuts for the 'WP80' selection.
- In addition, the 'golden' selection identifies explicitly objects that were not or little affected by bremsstrahlung: the same degree of curvature is required at the innermost and outermost parts of the track; besides the supercluster is required to be made of only one subcluster; finally the energy measured from the supercluster and the momentum measured from the track must present a very good agreement.

The response of the Level-1 trigger (L1_SingleEG8) for these different selections is presented in Fig. 3.18, for electrons in the ECAL barrel: the same color code as for Fig. 3.14 is used. A comparison of the measurements for the selections of conversion electrons (yellow), WP95 (blue) and WP80 (green) shows a significant improvement by effect of a tightened selection. Besides, the trigger response is quasi-immediate on electrons satisfying also 'golden' condition, as suggested by the 'golden WP95' (red) and 'golden WP80' (black) measurements: this response is very similar to the intrinsic trigger efficiency shown in Fig. 3.16.b.

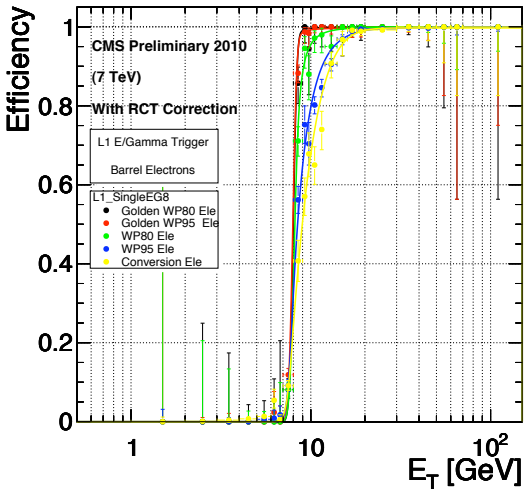

Figure 3.18: Efficiency of L1_SingleEG8 on several selections of electron candidates, and the selection of electrons from conversions (shown in yellow). The curves represent unbinned fits of the distributions, with the same color code.

3.4.3 Measurement on Electrons from $Z \to e^+e^-$ Events

The autumn 2010 was marked by a tremendous increase of the LHC instantaneous luminosity, resulting in a huge rise of the integrated luminosity (cf Fig. 3.1: the integrated luminosity was multiplied by a factor 10 in the 40 last days of collisions). Thousands of $Z \to e^+e^-$ events were recorded in CMS, providing a pure collection of electrons with a transverse energy generally greater than the Level-1 trigger threshold of 8 GeV, and comparable to, or greater than the HLT threshold of 17 GeV (corresponding to the lowest threshold of HLT single electron unprescaled trigger by that time).

3.4.3.1 A Pure and Unbiased Electron Selection

A pure electron selection

The usual method to select a pure electron population from $Z \rightarrow e^+e^-$ events, is called 'tag and probe'. It is based on a Z boson mass resonance condition, coupled to a tight selection applied on one electron, the 'tag', which warranties a high purity on the second electron, the 'probe'. Thus to test one property on a chosen selection of electrons, this selection is applied to the 'probe' electron sample, on which the property can then be tested (by counting the number that satisfy the property).

An unbiased electron selection

A population of $Z \rightarrow e^+e^-$ events with reasonable statistics can only be obtained on events selected by electron triggers. However, to study the Level-1 e/γ trigger efficiency on 'probe' electrons without any bias, one must make sure that their signal did not take part in the trigger decision: this is solved by making sure that the 'tag' electron is the reason of the recording of the event.

Thus, in addition to a usual 'tag' electron selection consisting in isolation and identification cuts, the 'tag' electron must be matched to the event Level-1 trigger candidate of highest transverse energy (which must be higher than the Level-1 trigger threshold). As a consequence, the event is known to have been recorded because of the 'tag' electron signal. The search for a trigger candidate matching the 'probe' electron is an unbiased test of the Level-1 trigger efficiency.

Choice of the studied electron collection

The remaining decision corresponds to the selection of 'probe' electrons on which the Level-1 trigger efficiency is to be measured. Unlike Minimum Bias studies, the 'tag and probe' method ensures a high purity of the 'probe' electron population, even for relatively loose 'probe' selections.

The chosen strategy was to test the consistency of the Level-1 and High-Level trigger systems. The unprescaled HLT single electron trigger of lowest transverse energy threshold that was used in the autumn 2010 requires an electron of transverse energy higher than 17 GeV, passing some identification and isolation cuts. This electron selection was reproduced on offline electrons; the transverse energy threshold was relaxed when the trigger efficiency

was studied as a function of the electron transverse energy.

Finally, the transverse energy measured by High-Level trigger takes the preshower measurement into account: for consistency, the trigger efficiency is measured as a function of the electron transverse energy (including the preshower measurement).

Summary

A 'tag and probe' selection is used to select electrons from $Z \rightarrow e^+e^-$ events. The invariant mass reconstructed from the 'tag' and 'probe' electrons is required to be greater than $60\,\mathrm{GeV/c^2}$ and lower than $120\,\mathrm{GeV/c^2}$. 'Tag' electrons are required to pass the tight identification and isolation selection 'WP80' (cf Annex B), detailed in Table 3.5. Finally, the 'HLT' selection described in Table 3.6 is applied to 'probe' electrons.

	H/E	$\Delta\eta^{in}$	$\Delta\phi^{in}$ (mrad)	$\sigma_{i\eta i\eta}$	$\frac{ecalIso}{p_T}$	$\frac{hcalIso}{p_T}$	$\frac{trackIso}{p_T}$
Barrel	< 0.04	< 0.004	< 0.06	< 0.01	< 0.07	< 0.1	< 0.09
Endcaps	< 0.025	< 0.007	< 0.03	< 0.03	< 0.05	< 0.025	< 0.04
	No ambiguous track, no missing hits in the inner part of the track.						

Table 3.5: Selection applied to the 'tag' electrons ('WP80' selection). In addition, these electrons must satisfy $p_T > 20\,\mathrm{GeV}/c$ and be matched to the Level-1 e/γ trigger candidate of highest transverse energy in the event.

	H/E	$\Delta\eta^{in}$	$\Delta\phi^{in}$ (mrad)	$\sigma_{i\eta i\eta}$	$\frac{ecalIso}{E_T}$	$\frac{hcalIso}{E_T}$	$\frac{trackIso}{E_T}$
Barrel	< 0.05	< 0.008	< 0.1	< 0.011	< 0.125	< 0.05	< 0.15
Endcaps	< 0.05	< 0.007	< 0.1	< 0.031	< 0.075	< 0.05	< 0.1

Table 3.6: Selection applied to the 'probe' electrons ('HLT' selection).

The purity of this selection was tested: when the 'HLT' transverse energy threshold of 17 GeV is also applied to the 'probe' electron, the distribution of the invariant mass is shown in Fig. 3.19: on the left, when the probe is matched to a Level-1 trigger candidate of transverse energy above the 8 GeV threshold; on the right, when either the matching or the threshold constraint failed. Both distributions are largely dominated by the Z boson mass resonance around $91\,\mathrm{GeV/c^2}$, which reflects the purity of the selection.

Since the energy plays a major role in this study, the data sample chosen includes a reprocessing with first energy corrections, taking laser information into account.

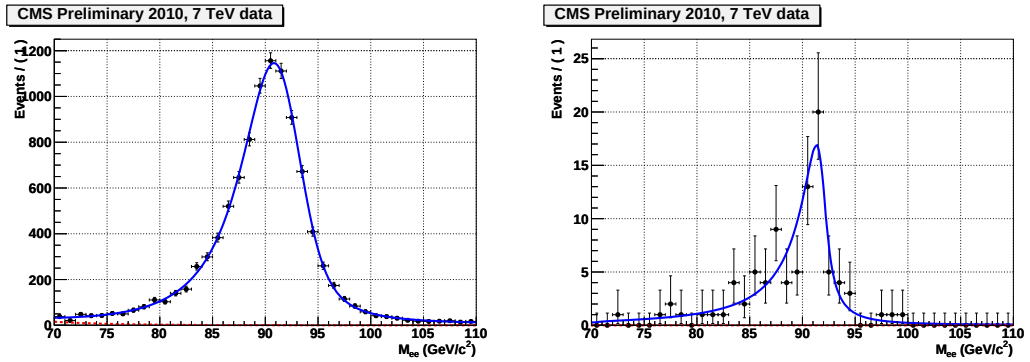

(a) (b)

Figure 3.19: Invariant mass from the two electrons identified by the 'tag and probe' method: left: both electrons are associated to Level-1 candidates above the 8 GeV threshold; right: the probe failed to be identified to a candidate above the threshold.

3.4.3.2 Results

A 'tag and probe' selection of electrons from $Z \rightarrow e^+e^-$ events provides a large and pure sample of electrons in the p_T range above 20 GeV/c. The plateau efficiency of L1_SingleEG8 is precisely measured on probe electrons passing the 'HLT' selection and transverse energy threshold at 17 GeV:

$$\epsilon_{EB} = 99.45^{+0.08}_{-0.09}\,\% \;;\; \epsilon_{EE} = 98.41^{+0.21}_{-0.23}\,\%. \tag{3.2}$$

These high efficiency values, together with measurements for transverse energy ranges around the 17 GeV threshold, suggest that the plateau efficiency is reached before 17 GeV for both barrel and endcaps. These results confirm the consistency of the trigger menu used in 2010.

The inefficiency cases for this population of probe electrons were studied: they all correspond to trigger towers masked for trigger considerations ($\sim 0.2\,\%$ in the barrel, $\sim 1\,\%$ in the endcaps) or to dead towers for trigger[14].

This selection does not provide however enough electrons with $10\,\text{GeV}/c < p_T < 20\,\text{GeV}/c$ to measure the turn-on of the L1_SingleEG8 efficiency. In preparation for the 2011 data taking, the efficiency of higher trigger thresholds was studied: L1_SingleEG12 and L1_SingleEG15 [40]. Because of their higher thresholds, the turn-on characteristics of these triggers could

[14]These towers were already mentioned in paragraph 3.2.3: masked towers for trigger considerations are indicated by diagonal hatches in Fig. 3.10; dead towers for trigger are the white towers remaining on the same figure, and correspond to link errors in the trigger path.